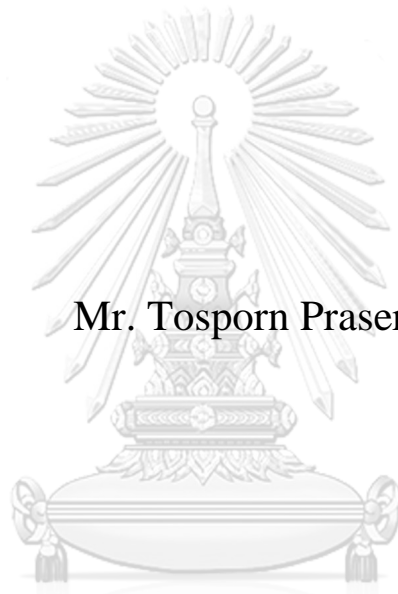


**A STUDY ON INTERMEDIATE DEBONDING FOR STEEL
BEAMS STRENGTHENED WITH FIBER REINFORCED
POLYMER PLATES**



Mr. Tosporn Prasertsri

จุฬาลงกรณ์มหาวิทยาลัย
CHULALONGKORN UNIVERSITY

A Dissertation Submitted in Partial Fulfillment of the Requirements
for the Degree of Doctor of Philosophy in Civil Engineering
Department of Civil Engineering
Faculty of Engineering
Chulalongkorn University
Academic Year 2019
Copyright of Chulalongkorn University

การศึกษาการหลุดล่อนที่ช่วงภายในสำหรับคานเหล็กที่เสริมกำลังด้วยแผ่นพอลิเมอร์เสริมเส้นใย



วิทยานิพนธ์นี้เป็นส่วนหนึ่งของการศึกษาตามหลักสูตรปริญญา
วิศวกรรมศาสตรดุษฎีบัณฑิต
สาขาวิชาวิศวกรรมโยธา ภาควิชาวิศวกรรมโยธา
คณะวิศวกรรมศาสตร์ จุฬาลงกรณ์มหาวิทยาลัย
ปีการศึกษา 2562
ลิขสิทธิ์ของจุฬาลงกรณ์มหาวิทยาลัย

Thesis Title A STUDY ON INTERMEDIATE DEBONDING FOR
STEEL BEAMS STRENGTHENED WITH FIBER
REINFORCED POLYMER PLATES
By Mr. Tosporn Prasertsri
Field of Study Civil Engineering
Thesis Advisor Associate Professor AKHRAWAT LENWARI, Ph.D.

Accepted by the Faculty of Engineering, Chulalongkorn University in Partial
Fulfillment of the Requirement for the Doctor of Philosophy

..... Dean of the Faculty of Engineering
(Professor SUPOT TEACHAVORASINSKUN, D.Eng.)

DISSERTATION COMMITTEE

..... Chairman
(Professor Thaksin Thepchatri, Ph.D.)
..... Thesis Advisor
(Associate Professor AKHRAWAT LENWARI, Ph.D.)
..... Examiner
(Professor TEERAPONG SENCHANTICHAI, Ph.D.)
..... Examiner
(Associate Professor JAROON RUNGAMORN RAT,
Ph.D.)
..... Examiner
(Assistant Professor PITCHA JONGVIVATSAKUL,
Ph.D.)
..... External Examiner
(Associate Professor Sayan Sirimontree, Ph.D.)

จุฬาลงกรณ์มหาวิทยาลัย
CHULALONGKORN UNIVERSITY

ทศพร ประเสริฐศรี : การศึกษาการหลุดล่อนที่ช่วงภายในสำหรับคานเหล็กที่เสริมกำลังด้วยแผ่นพอลิเมอร์เสริมเส้นใย. (A STUDY ON INTERMEDIATE DEBONDING FOR STEEL BEAMS STRENGTHENED WITH FIBER REINFORCED POLYMER PLATES) อ.ที่ปรึกษาหลัก : รศ. ดร.อัศววัชร เล่นวารี

เนื่องจากมีงานวิจัยในอดีตเป็นจำนวนน้อยที่ศึกษาการเกิดการหลุดล่อนของแผ่นพอลิเมอร์เสริมเส้นใย (FRP) ที่ช่วงภายในคานเหล็ก จากการทดสอบคานเหล็กเสริม FRP ที่ผ่านมาใช้วิธีสร้างรอยบากในคานเหล็กเพื่อก่อให้เกิดการหลุดล่อนของ FRP ที่ช่วงภายใน รวมถึงในงานวิจัยใช้ระบบยึดคั้งที่ปลายแผ่น FRP งานวิจัยนี้ใช้ความบกพร่องเริ่มต้นของชั้นวัสดุประสานเพื่อเหนี่ยวนำการหลุดล่อนของแผ่น FRP ที่ช่วงภายใน การทดสอบแรงเฉือนเดี่ยว ดำเนินขึ้นเพื่อศึกษาพฤติกรรมการยึดเหนี่ยวระหว่างเหล็กและ FRP รวมถึงจัดให้มีการทดสอบรับแรงดัดเพื่อศึกษาพฤติกรรมการดัดของคานเหล็กที่เสริมกำลังด้วยแผ่น FRP จากการทดสอบพบว่า รอยต่อระหว่างเหล็กและ FRP ที่มีความบกพร่องเริ่มต้นของชั้นวัสดุประสานมีแนวโน้มช่วยลดการเกิดความเสียหายแบบพื้นที่แยกชั้นใน FRP สำหรับคานเหล็กที่เสริมกำลังด้วยแผ่น FRP และมีความบกพร่องเริ่มต้นของชั้นวัสดุประสาน พบว่ากำลังและดัชนีความเหนียวของคานมีค่าเพิ่มขึ้น



สาขาวิชา วิศวกรรมโยธา

ปี 2562

การศึกษา

ลายมือชื่อนิสิต

.....

ลายมือชื่อ อ.ที่ปรึกษาหลัก

.....

5771410321 : MAJOR CIVIL ENGINEERING

KEYWORD fiber-reinforced polymer, flexural strengthening, initial bond defect,
D: steel beam, debonding

Tosporn Prasertsri : A STUDY ON INTERMEDIATE DEBONDING FOR STEEL BEAMS STRENGTHENED WITH FIBER REINFORCED POLYMER PLATES. Advisor: Assoc. Prof. AKHRAWAT LENWARI, Ph.D.

There are limited previous works focusing on the occurrence of intermediate debonding in steel beams strengthened with fiber reinforced polymer (FRP) plates. Tested beams in the past experiments invoked an intermediate debonding by creating notch in steel beams. An anchorage system at FRP termination points was installed on some tested beams in literature. This research uses an initial bond defect to induce an intermediate debonding at the FRP-steel interface. The bond behavior of FRP-steel interface was investigated through the FRP-steel joints under the single lap shear testing. A four-point bending test was conducted to examine the flexural properties of FRP-strengthened steel beams. The existence of initial bond defect tends to reduce an area of FRP delamination. FRP-strengthened steel beams with initial bond defect failed by FRP intermediate debonding instead of fiber rupture. The presence of initial bond defect improved both strength and ductility index of beams.



Field of Study: Civil Engineering

Student's Signature

Academic 2019

Advisor's Signature

Year:

.....

ACKNOWLEDGEMENTS

I cannot begin to express my gratitude to my father, Group Captain Dr. Pisit PRASERTSRI, my mother, Sujitra PRASERTSRI, and my grandfather, Flight Lieutenant Wiroj JIRAMANEEMAI, whose love and guidance are with me in whatever I pursue. They are always my best role models. Most importantly, I would also like to extend my thank to my supportive girlfriend, Kanyanat PROMRUNGREANG, and my kindness brother, Colonel Supanut PROMRUNGREANG, M.D., who provided me with encouragement and patience throughout the duration of this work.

This research work would not have been possible without the financial support of the 100th Anniversary Chulalongkorn University Fund for Doctoral Scholarship and the 90th Anniversary of Chulalongkorn University Fund (Ratchadaphiseksomphot Endowment Fund). I am especially indebted to my dissertation advisor, Associate Professor Dr. Akhrawat LENWARI. He made an invaluable contribution to the improvement of my research expertise. I am also grateful to my chair committee, Professor Emeritus Dr. Thaksin THEPCHATRI, for many insightful suggestions. Particularly helpful to me during this time were my committees, Professor Dr. Teerapong SENJUNTICHAJ, Associate Professor Dr. Jaroon RUNGAMORN RAT, Assistant Professor Dr. Pitcha JONGVIVATSAKUL, Associate Professor Dr. Sayan SIRIMONTREE, who have provided ideas and constructive criticism. I would like to recognize the assistance that I received from Sika Thailand, Ltd., and Retrofit Structure Specialist, Ltd., for supporting and installing FRP materials and adhesive system. I also had great pleasure of working with all staff members and students in the Department of Civil Engineering.

Tosporn Prasertsri

TABLE OF CONTENTS

	Page
ABSTRACT (THAI)	iii
ABSTRACT (ENGLISH).....	iv
ACKNOWLEDGEMENTS	v
TABLE OF CONTENTS.....	vi
TABLE OF TABLES	ix
TABLE OF FIGURES	x
CHAPTER 1 INTRODUCTION.....	1
1.1 Background.....	1
1.2 Significance of Research	3
1.3 Objectives	3
1.4 Scope	3
1.5 Outline of Dissertation	4
CHAPTER 2 LITERATURE REVIEW.....	5
2.1 Overview	5
2.2 Bond Behavior of FRP-Steel Interfaces	5
2.3 Plate End Debonding in FRP-Strengthened Steel Beams	14
2.4 Intermediate Debonding in FRP-Strengthened Steel Beams.....	20
2.5 Fracture-Based Analysis of Intermediate Crack-Induced Debonding.....	26
CHAPTER 3 EXPERIMENTAL PROGRAM.....	30
3.1 Specimens.....	30
3.1.1 Material Properties	31
3.1.2 Surface Preparation	33
3.1.3 Initial Bond Defects Creation.....	34
3.1.4 Joint Specimens	36
3.1.5 Beam Specimens	37

3.2 Test Setup and Instrumentation	38
3.2.1 Test Configuration.....	38
3.2.2 Strain Gage Locations and Designation	40
CHAPTER 4 BOND BEHAVIOR OF FRP-STEEL INTERFACE.....	45
4.1 Failure of Joint Specimens	45
4.2 Strain Development in FRP plates	48
4.3 Interfacial Fracture Toughness	51
CHAPTER 5 FLEXURAL BEHAVIOR OF FRP-STRENGTHENED STEEL BEAMS.....	55
5.1 Failure of Beam Specimens.....	55
5.2 Definition of Yielding Point.....	58
5.3 Test Variables on Flexural Properties of FRP-Strengthened Steel Beams.....	58
5.3.1 Effect of FRP Modulus.....	60
5.3.2 Effect of Initial Bond Defect.....	63
5.3.3 Effect of FRP Bond Length.....	64
5.3.4 Effect of Predamage	65
5.3.5 Effect of Periodic Unloading.....	68
5.4 Strain Distribution at Midspan Section	70
5.5 Strain Distribution Along FRP Plates.....	73
5.6 Beam Tested under Periodic Unloading.....	74
CHAPTER 6 CONCLUSIONS	78
6.1 Conclusions	78
6.1.1 Bond Behavior of FRP-Steel Joints.....	78
6.1.2 Flexural Behavior of FRP-Strengthened Steel Beams	78
6.2 Recommendations for Future Works.....	79
REFERENCES	80
APPENDIX A EXPERIMENTS CHECKING.....	87
A.1 Symmetry of the Applied Load	87
A.2 Loading Rate	92

APPENDIX B PRE-PEAK BEHAVIOR OF TESTED BEAMS.....	98
B.1 Definition of Yielding Point.....	98
B.2 Strain Distribution at Midspan Section (Before Yielding).....	102
B.3 Strain Distributions at Midspan Section (Between Yield and Maximum Loads)	
107	
B.4 Strain Distributions of Steel in Vicinity of Midspan Section (Before Yielding)	
111	
B.5 Strain Distributions at Steel Beams in Vicinity of Midspan Section (Between	
Yield and Maximum Loads).....	115
B.6 Strain Distributions Along FRP Plates (Before Yielding)	119
B.7 Strain Distributions Along FRP Plates (Between Yield and Maximum Loads)	
122	
APPENDIX C POST-PEAK BEHAVIOR OF MONOTONIC TESTED BEAMS..	127
C.1 Load-Deflection Curves	127
C.2 Strain Distribution at Midspan Section	130
C.3 Strain Distributions of Steel in Vicinity of Midspan Section.....	134
C.4 Strain Distribution Along FRP Plates.....	137
VITA.....	141

TABLE OF TABLES

	Page
Table 3.1 Material properties of steel and CFRP.....	32
Table 3.2 Specimen designation in single lap shear test.....	36
Table 3.3 Details of beam specimens.	37
Table 4.1 Fracture toughness of joint specimens.....	52
Table 5.1 Flexural properties of beams.....	59
Table 5.2 Steel strains of unstrengthened beams at yielding point.....	70
Table 5.3 Steel strains of FRP-strengthened beams at yielding point.	71
Table 5.4 Steel strains of unstrengthened beams at maximum load.....	72
Table 5.5 Steel strains of FRP-strengthened beams at maximum load.....	73

TABLE OF FIGURES

	Page
Figure 1.1 Properties of different fibers and typical reinforcing steel. [1]	1
Figure 1.2 Plate end debonding failure of strengthened steel beam with anchoring bolts. [2]	2
Figure 1.3 FRP-steel hybrid joint specimen for double lap shear test . [3].....	2
Figure 2.1 Steel specimens with doubly FRP reinforcement. [6]	6
Figure 2.2 Double strap joint test. [8]	6
Figure 2.3 Single lap joint test. [12]	7
Figure 2.4 NES single shear test. [13]	8
Figure 2.5 Bond-slip relationship. [13].....	9
Figure 2.6 Hybrid joint test. [3]	9
Figure 2.7 Surface preparations of the steel splice plate. [3].....	10
Figure 2.8 Schematic view of specimens. [15]	11
Figure 2.9 FRP unbonded length in FRP-steel specimen. [18].....	12
Figure 2.10 Geometry of FRP-steel specimens. [24].....	13
Figure 2.11 Four-point bending test of superlight beam. [8].....	14
Figure 2.12 Four-point bending test of steel beams. [29]	15
Figure 2.13 Strengthening configurations around slit. [29].....	16
Figure 2.14 FRP strips strengthened steel beam. [34]	17
Figure 2.15 Damages at the below load location. [34]	18
Figure 2.16 FRP-strengthened steel beam with a stiffener. [38]	19
Figure 2.17 Debonding failures in FRP-strengthened steel beam.	20
Figure 2.18 Anchoring plates at FRP plate ends. [40].....	21
Figure 2.19 Notched beam specimen tested by Kim and Brunell. [45].....	22
Figure 2.20 Notched beam specimen tested by Zhou et al. [46].....	23
Figure 2.21 FRP-strengthened notched steel beam configuration. [48]	24
Figure 2.22 Anchorage system of the beam tested by Karam et al. [49].....	24

Figure 2.23 Anchorage configurations of the beam tested by El-Taly. [50]	25
Figure 2.24 Applied load in RC section. [54].....	28
Figure 2.25 Beam specimens in Gunes’s research. [47].....	28
Figure 3.1 Beam specimen welded with steel cover plate.	30
Figure 3.2 Welding between steel beam and cover plate.....	31
Figure 3.3 Tensile test set-up.	32
Figure 3.4 Metal surface preparation.	34
Figure 3.5 Defect creation.....	35
Figure 3.6 Adhesive proof using insulated paper.	35
Figure 3.7 Examined defect types.....	36
Figure 3.8 Overview of single lap shear test.....	38
Figure 3.9 Details of supporting frame for single lap shear test (all dimension in mm).	39
Figure 3.10 Four-point flexural test set-up.	39
Figure 3.11 Data logging system.	40
Figure 3.12 Instrumentation on joint specimens (all dimensions in mm).....	41
Figure 3.13 Instrumentation on unstrengthened steel beams (all dimensions in mm).42	
Figure 3.14 Instrumentation on FRP-strengthened steel beams (all dimensions in mm).	43
Figure 3.15 Details of instrumentation on CFRP plate and steel beam (all dimensions in mm).....	44
Figure 4.1 Visible failure of joints without initial bond defect (joint JMU400-0).	46
Figure 4.2 Visible failure of joints with different defect types.....	46
Figure 4.3 Failure surface of joints with interfacial defect.	47
Figure 4.4 Failure surface of joints without interfacial defect.....	48
Figure 4.5 FRP strain distributions of joints with interfacial defect.....	49
Figure 4.6 FRP strain distributions of joints without interfacial defect.....	50
Figure 4.7 Bond-slip curve of joints with interfacial defect.	53
Figure 4.8 Bond-slip curve of joints without interfacial defect.	54
Figure 5.1 Unstrengthened beams after terminating the tests.....	55

Figure 5.2 Beam specimens during testing.....	56
Figure 5.3 FRP-strengthened steel beams at the critical state of failure.....	57
Figure 5.4 Typical failure modes of FRP-strengthened beams.....	57
Figure 5.5 FRP intermediate debonding in beam BMM150-100.....	58
Figure 5.6 Effect of FRP modulus on load-deflection curve.....	61
Figure 5.7 Effect of FRP modulus on load-deflection curve under periodic unloading condition.....	62
Figure 5.8 Effect of initial bond defect on load-deflection curve.....	64
Figure 5.9 Effect of FRP bond length on load-deflection curve.....	65
Figure 5.10 Effect of predamage on load-deflection curve.....	67
Figure 5.11 Effect of periodic unloading on load-deflection curve.....	69
Figure 5.12 Definition of energies in beams tested under periodic unloading.....	74
Figure 5.13 Development of energies in beam CBP.....	75
Figure 5.14 Development of energies in beam BSP120-100.....	75
Figure 5.15 Development of energies in beam BMP120-100.....	76
Figure 5.16 Ratio between unloading stiffness and initial stiffness.....	76
Figure 5.17 Difference between recoverable energies before and after FRP strengthening.....	77

CHAPTER 1

INTRODUCTION

1.1 Background

Fiber-reinforced polymer (FRP) is the kind of composite materials formed by embedding continuous fibers in certain types of polymeric matrix. Common types of fibers used for structural rehabilitation are carbon, aramid, and glass fibers. These materials have higher elastic modulus and ultimate strength than reinforcing steel bars or mild steel as shown in Figure 1.1. FRPs have gained wide acceptance in structural strengthening during the past 20 years because of their high strength-to-weight ratio and corrosion resistance with respected to steel.

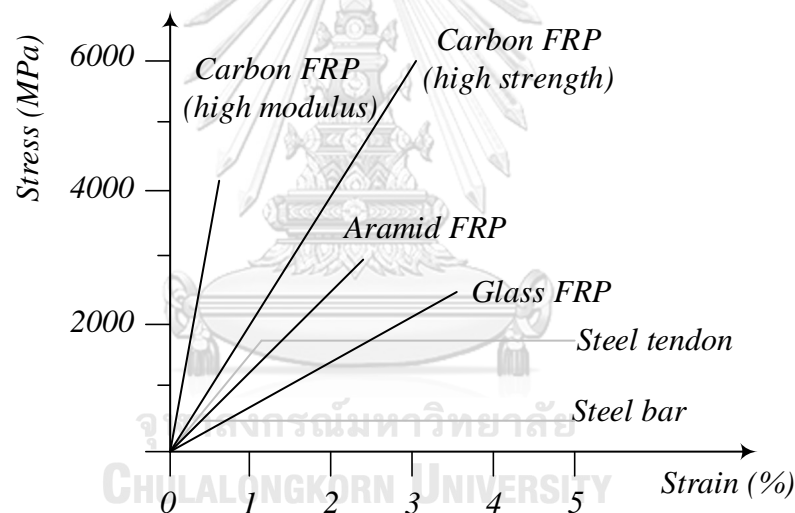


Figure 1.1 Properties of different fibers and typical reinforcing steel. [1]

For flexural strengthening of steel beams, FRP is externally bonded to bottom flange by adhesive layer made from various types of polymer-based materials. Many individuals seem to agree that this layer is the weak link leading FRP debonding mechanism to induce the premature failure without utilizing the full strength of FRP plates [2-5]. Few research works suggested FRP strengthening technique using mechanical anchored bolts along the beam to prevent the unfavorable brittle mechanism due to FRP debonding. Some specimens still failed by plate end

debonding (to be described in CHAPTER 2) because of shear fracture in anchoring bolts as shown in Figure 1.2.



Figure 1.2 Plate end debonding failure of strengthened steel beam with anchoring bolts. [2]

It is worth noting that the combined system including adhesive bonding and mechanical anchored bolts is called the "hybrid joint" (see Figure 1.3). Mechanical fastening is used as a safeguard against bond imperfections within the adhesive layer which may lead to catastrophic failure. However, there are few studies conducted on such joint tests by using hybrid FRP. This approach needs more investigation before the real application [3] and the optimum configuration of anchoring bolts have not been explored in this period.

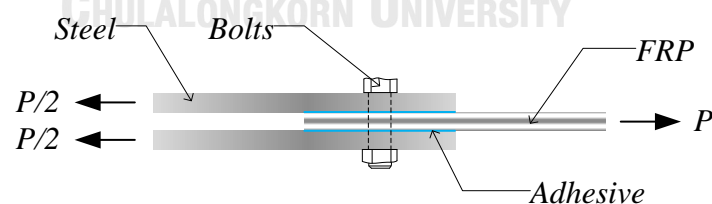


Figure 1.3 FRP-steel hybrid joint specimen for double lap shear test . [3]

Prior research attempted to predict local and global behavior of FRP-strengthened steel beams by using finite element (FE) analysis due to the expensive and time-consuming of experiment [4]. This is based on a complicated mathematical model that is composed of mixed-mode cohesive law and claimed that the failure

mode of strengthened beam is intermediate debonding (to be described in CHAPTER 2) if the longer FRP plate is used [5].

This research question is particularly interesting in the occurrence of intermediate debonding in FRP-strengthened steel beams. Toward an understanding of bond behavior of FRP-steel interfaces would require lap shear testing of FRP-steel joints. Flexural testing has been used to investigate the flexural behavior of FRP-strengthened steel beams with a consideration of intermediate debonding effect.

1.2 Significance of Research

This research is conducted because the previous studies and practical specifications had few explorations of intermediate debonding initiation in the FRP-strengthened steel beams with initial bond defects. In addition, the effects of an initial bond defect on the flexural behavior of the FRP-strengthened steel beams should be investigated.

1.3 Objectives

Main objectives of this research are listed below:

1. To study the bond behavior in the FRP-steel bonded joints with initial bond defects.
2. To study the flexural behavior and intermediate debonding of FRP plates in the FRP-strengthened steel beams with initial bond defects.

1.4 Scope

The scope of research is given below:

1. Other failure modes in FRP-strengthened steel beams such as compression flange buckling and web crippling are beyond the scope of this study.
2. Parameters affected to any environmental effects, durability, and cyclic behaviors are excluded from this study.

1.5 Outline of Dissertation

There are six chapters in this dissertation. CHAPTER 1 states the background information on using FRP in the strengthening of structural components especially beams to understand whether this research fits into a wider field of FRP strengthening of steel structures. Previous research gap, research purposes and hypotheses, and expected outcomes of this study are also presented.

CHAPTER 2 collects the findings of other researchers who have already investigated experimentally and/or numerically the bond behavior of FRP-steel bonded joints, plate end debonding and intermediate debonding of FRP-strengthened steel beams, and fracture-based analysis of FRP-strengthened reinforced concrete (RC) beams.

CHAPTER 3 points out the experimental program and test protocol developed in this study such as single lap shear tests and full-scale FRP-strengthened steel beams tests.

CHAPTER 4 presents the experimental results and discussion of single lap shear testing. FRP strain development and fracture toughness are investigated to study the bond behavior of FRP-steel joint specimens.

CHAPTER 5 reveals the experimental results and discussion of four-point flexural testing. Load-deflection curves are exhibited and examined to focus on the flexural behavior of the tested beams. Energy dissipation during testing is concerned to study the behavior of periodic unloading tested beams.

CHAPTER 6 summarizes the findings of this study. The major concluded points are twofold: bond behavior of joints and flexural behavior of FRP-strengthened steel beams. Recommendation for future works is also discussed in this chapter.

CHAPTER 2

LITERATURE REVIEW

2.1 Overview

Realistic interfacial behavior of FRP-steel bonded joints and the reliable mathematical model play an important role in the prediction of debonding initiation and the failure modes of FRP-strengthened steel girders. This chapter collects a number of previous research works that focused on the corresponding points for the development and achieve the objectives of the current work. Section 2.2 covers the experimental works that investigated behavior of FRP-steel joints. Section 2.3 gathered the recent studies that have generated the appropriated analytical or mathematic model for prediction of FRP plate end debonding in strengthened steel beams. A review of literature on intermediate debonding and their limitations are presented in section 2.4. Finally, section 2.5 collected previous works on fracture-based analysis of intermediate crack-induced (IC) debonding in FRP-strengthened RC beams. This plays an important role for the development of an analysis for FRP-strengthened steel beams.

2.2 Bond Behavior of FRP-Steel Interfaces

A key factor controlling the behavior of metallic structures strengthened with FRP is interfacial behavior between FRP and steel that have many different experimental set-ups for investigating the bond-slip relationship. The tensile test of steel specimens with doubly FRP reinforcement (see Figure 2.1) were conducted by Miller et al. [6]. FRP plates at the termination points were beveled to a 45° that is a typical procedure for composite joints and has proven to effectively limit peel stresses [7]. Tension is directly applied to the steel plates without any gap. The specimens were failed by steel yielding. It seems that such testing method was more suitable for studying strengthening rather than the investigation of bond behavior.

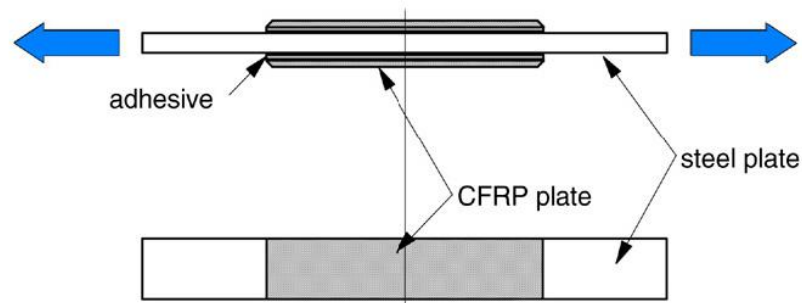


Figure 2.1 Steel specimens with doubly FRP reinforcement. [6]

Schnerch et al. [8] determined a suitable resin for the wet layup of unidirectional FRP sheets bonded to steel plate through double strap shear test. Tension was directly applied to the steel plate with a gap. The specimen configuration is shown in Figure 2.2. The average shear strength of each specimen was not much different, but three failure modes occur such as plate rupture, fiber rupture, and fiber tow pullout. This testing method was also conducted by Fawzia et al. [9] to investigate the effects of bond length and FRP modulus on ultimate bond strength. Unequal bond lengths were used to invoke FRP debonding in the regions with shorter bond lengths. Test results revealed that the failure mode for specimens with normal modulus FRP (240 GPa) was bond failure whereas fiber break failure was observed for specimens with high modulus FRP (640 GPa).

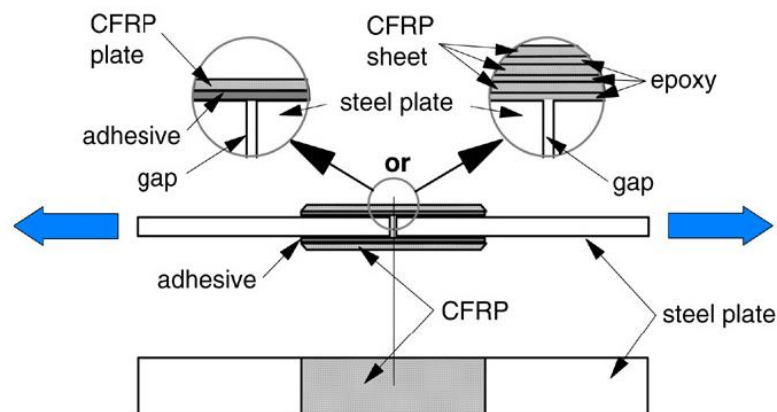


Figure 2.2 Double strap joint test. [8]

Colombi and Poggi [10] verified the effectiveness of the use of FRP pultruded plates to strengthen steel elements by comparing their experimental work and the strength-based model proposed by Albat and Romilly [11]. The analytical could estimate stress distribution along the FRP with good accuracy before the initiation of FRP debonding.

The single lap shear test shown in Figure 2.3 is the alternative testing method for the investigation of FRP-steel joint behavior because only one path for debonding is possible unlike the double strap joint that there are four possible locations exist for the propagation of debonding. Xia and Teng [12] conducted such testing method to study the interfacial behavior of a pultruded FRP plate bonded to a steel plate. This research concluded that the adhesive thickness had a significant effect on the failure mode. Thin adhesive layer (usually less than two millimeters) may reveal the ductile failure process within the adhesive layer; furthermore, FRP delaminating that is a more brittle mode may occur if thick adhesive layer is used. The key parameters of the relationship between shear stress and slip were the maximum bond shear stress τ_{max} , the corresponding separation δ_I , the separation at ultimate state δ_f , and the interfacial fracture energy G_f (defined from the area under bond-slip relationship). However, this testing method must be sure that the alignment is maintained to minimize load eccentricity.

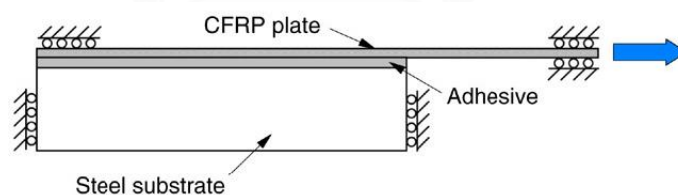


Figure 2.3 Single lap joint test. [12]

Fernando [13] conducted a series of near end supported (NES) single shear tests on FRP-steel joints shown in Figure 2.4.

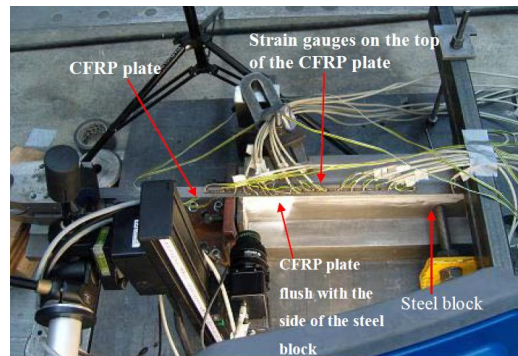
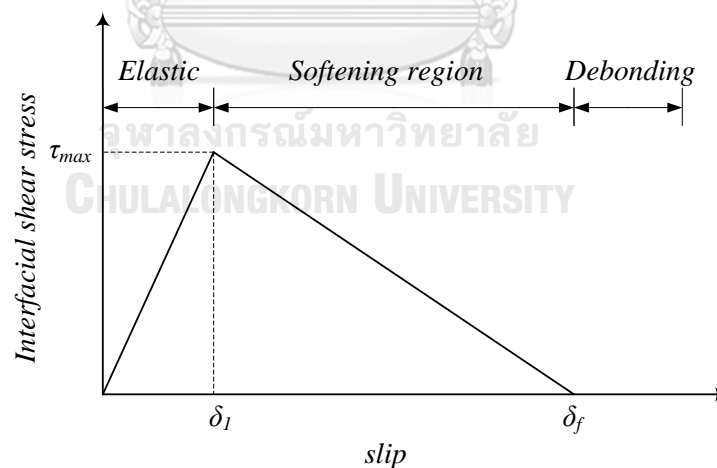
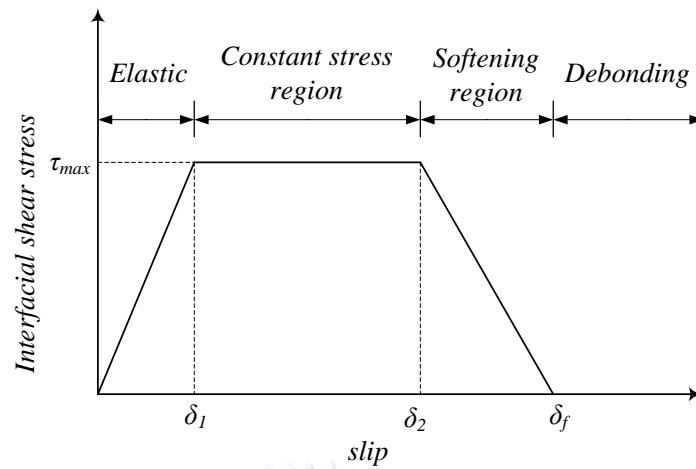


Figure 2.4 NES single shear test. [13]

This work used various types of adhesives and concluded that the adhesive could be categorized as two types (i.e., linear adhesive and nonlinear adhesive) by adhesive tensile test. Linear adhesive denoted the regular adhesive that seems to linearly behavior when subjected to tensile loading. There are other kinds of adhesive that behave nonlinearly in tension and has a high strain capacity (designated as nonlinear adhesive). Moreover, lap shear tests revealed that utilizing the trapezoidal bond-slip model for FRP-steel joints with nonlinear adhesive was more appropriate than two-branch bond-slip model. Two types of bond-slip relationship for FRP-steel bonded joints are shown in Figure 2.5.



(a) linear adhesive



(b) nonlinear adhesive

Figure 2.5 Bond-slip relationship. [13]

The major disadvantages of FRP bonded structural components are the consumption of surface preparation time and the existence of unfavorable brittle mechanism caused by FRP debonding. FRP-steel hybrid joint, which was defined in section 1.1, was tested by Hai and Mutsuyoshi [3]. Typical testing specimen is depicted in Figure 2.6. The aim of the study was to examine the effect of tested variables on load-displacement relationship of tested specimens. The tested variables consisted of adhesive thickness, surface preparations of the steel splice plate, sheared edge distance of bolts, and applied bolt torque.

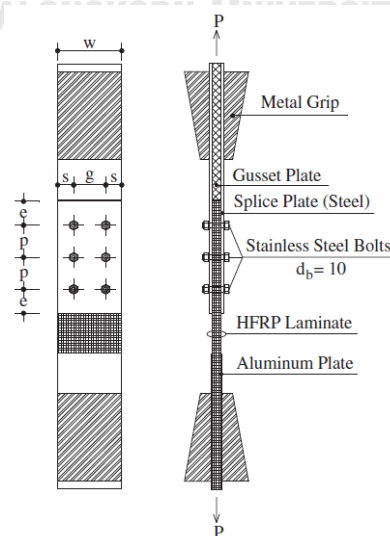


Figure 2.6 Hybrid joint test. [3]

Surface preparations of the steel splice plate consisted of V-notched surface and flat surface as seen in Figure 2.7. Three types of joint specimens (bonded, bolted, and hybrid) were prepared. Test results showed that the hybrid joint without adhesive thickness control (approximately 0.1 mm) was much stiffer than bolted joint because of interaction between adhesive bonding and mechanical anchorage. Roughness of V-notched surface could not only provide additional clamping force between splice plates and the specimen but also controlled the adhesive thickness without any holders. Bolt diameter times three ($3d$) was the recommended minimum sheared edge distance to ensure the bearing failure. 20 N-m bolt torque was also recommended based on the experimental results. However, this research utilized pultruded hybrid FRP laminate that was not widely used and the proposed minimum sheared edge distance may not cover for all kind of fibers.

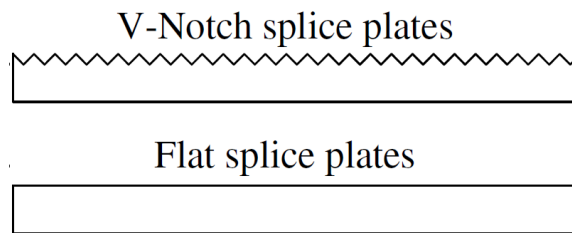


Figure 2.7 Surface preparations of the steel splice plate. [3]

Yu et al. [14] presented the experimental testing of a series of single-lap bonded joints conducted by Fernando [13]. The test investigated the effects of FRP bond length, the rigidity of the FRP plate, adhesive thickness, and mechanical properties of adhesive on the bond strength of such specimens. Both linear adhesive and nonlinear adhesive were provided for the specimen. The test results revealed that the use of linear adhesive led to a much lower interfacial fracture energy than nonlinear adhesive (with high strain capacity) even though tensile strength and elastic modulus of nonlinear adhesives were less than linear adhesive. The bond strength of such specimens depended on the interfacial fracture energy as well as the FRP plate rigidity; furthermore, utilizing FRP bond length beyond the effective value did not lead to a further increase in the bond strength. This study conducted only three specimens with various adhesive thicknesses and concluded that the bond strength

increased with the adhesive thickness since the specimen contained thickest adhesive shown low bond strength.

Sweedan et al. [15] expected that the utilization of mechanical anchoring bolts without adhesive layer may prevent FRP debonding in FRP-strengthened steel beams. This work investigated the behavior of FRP-steel bolted joints by experimental and numerical studies. Two types of specimens as shown in Figure 2.8. A nonlinear load-slip model for FRP-steel interfacial behavior was proposed and shown good agreement with the test results. This study also suggested the optimum sheared edge distance is between $6d$ and $7d$. The rolled edge distance was insignificantly affected to the interfacial behavior of tested specimens. However, the optimum sheared edge distances proposed by Hai and Mutsuyoshi [3] was also shown conflicted with this study.

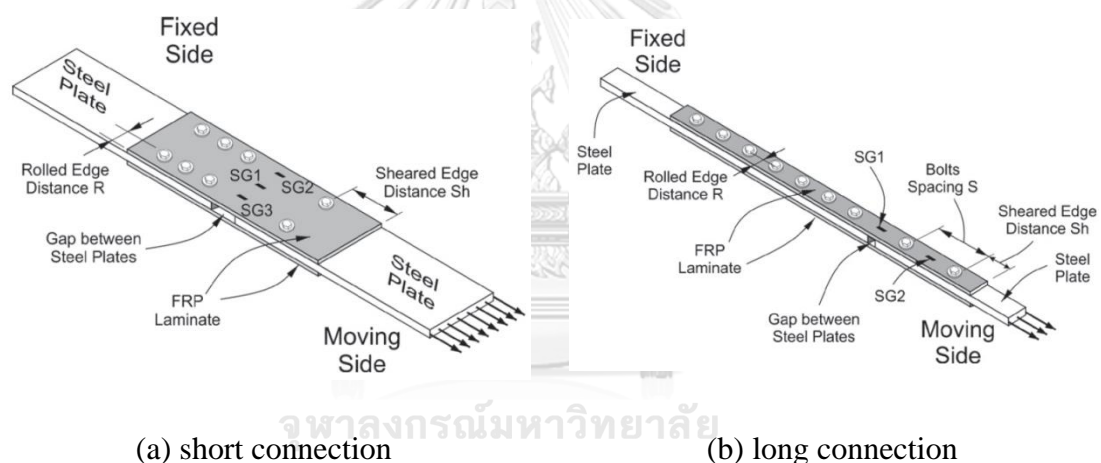


Figure 2.8 Schematic view of specimens. [15]

Analytical solution for the full-range behavior of FRP-steel bonded joints with a nonlinear adhesive was presented by Fernando et al. [16] to explain the different stages of debonding failure. The formulation of the governing equations is based on the classical stresses analyses in FRP-concrete interfaces done by Yuan et al. [17]. The solution was directly relevant to FRP debonding in FRP-steel joints. This work served as the necessary first step towards the development of modeling of plate debonding in FRP-strengthened steel beams. An approach may not put into practice because of its complication.

Experimental results of FRP-steel bonded tests and the existing bond strength model for FRP-steel interface from the technical literature were gathered by Ceroni et al. [18]. The research aims to assess the influence of geometrical and mechanical properties of the adhesive on the debonding load. A bond strength of tested specimens was calculated from the existing strength model [12, 13, 19, 20]. This study did not discuss the appropriated bond strength model for calculating the effective bond length. NES single shear test adopted by Ceroni et al. [18] calculated the effective bond length based on the formulation given by the Italian code [21]. Note that an effective bond length is the FRP bond length that permit an increase of FRP strain. A fully bond strength developed with the increasing of FRP strain. Moreover, effects of FRP unbonded length on interface fracture energy was not clear since this study set the 50 mm of FRP unbonded length (see Figure 2.9) as controlled parameter.

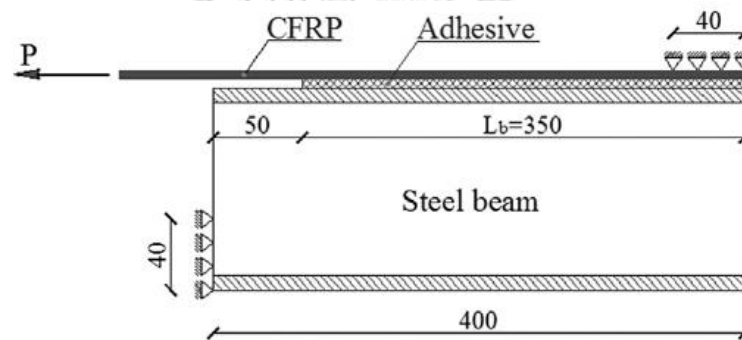


Figure 2.9 FRP unbonded length in FRP-steel specimen. [18]

Wang et al. [22] applied the digital image correlation technique to measure the strain and deflection of tested specimens. This work investigated the effects of FRP bond length and adhesive thickness on the ultimate strength through the single lap shear test method. The research concluded that such measurement technique could provide continuous deformation data and suitable for studying the interfacial behavior of FRP-steel bonded joints. Experimental results revealed that a bond length longer than the effective bond length remains unchanged ultimate strength. From an adhesive thickness between 0.5 to 2 mm, the ultimate strength of tested specimens is enhanced as the adhesive thickness increased. The ultimate strength is decreased in case of the increase of the adhesive which is thicker than 2 mm. [23].

A 20-mm FRP unbonded zone as depicted in Figure 2.10 was used in the joint specimens conducted by He and Xian [24]. The specimens were tested using a single lap shear method. A load-displacement relationship of the tested specimens was fitted with a prediction determined from a finite element analysis. A bond-slip model in an exponential form for FRP-steel joints was proposed. However, an effect of a FRP unbonded length on bond-behavior and fracture toughness of FRP-steel joints was not revealed.

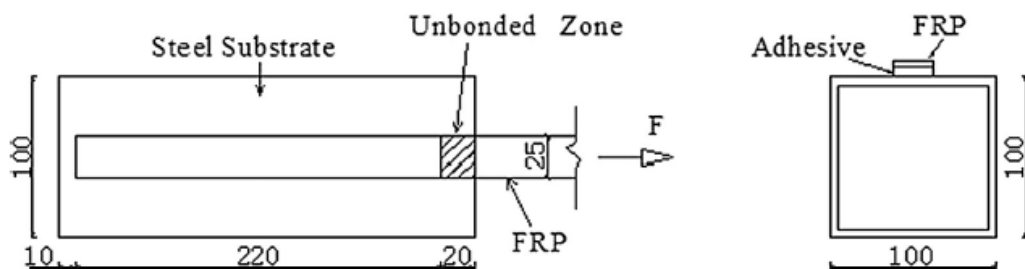


Figure 2.10 Geometry of FRP-steel specimens. [24]

The bond-slip relationship of FRP-steel interface proposed in Fernando's work [13] was improved by Wang et al. [25]. The 37 tests of FRP-steel specimens were collected to calibrate the model parameters. The predicted ultimate load, strain distribution, and load-slip curve had reasonably accurate with the previous test data. A statistical evaluation of the model uncertainty of FRP-steel interface using the 414 tests of FRP-steel specimens was investigated by Yu et al. [26]. The most influential parameter that affect an accuracy of predicted bond behavior is a tensile strength of adhesive.

Previous research showed that steel yielding failure was often avoided in double strap joint testing by using a sufficient steel plate thickness [27]. The FRP debonding was initiated at the FRP plate end and then propagates to a loaded end of joint specimens. This fracture process is consistent with FRP plate end debonding (to be described in section 2.3) but not for intermediate debonding (to be described in section 2.4). Moreover, there are fewer studies on the effects of intermediate debonding on bond behavior and interfacial fracture energy in single lap joint specimens. These should be addressed for the development of an analysis of FRP-strengthened steel beams to predict the locations of FRP debonding and recommend the design guideline for FRP debonding prevention.

2.3 Plate End Debonding in FRP-Strengthened Steel Beams

This section gathers the research that focused on FRP debonding problem in the FRP-strengthened steel beams. Many studies were conducted to represent closed-form solution and finite element analysis that effort to take account into any interfacial behavior of adhesive layer for the realistic prediction for solving such problem. Deng et al. [28] developed a closed -form solution to calculate the interfacial stresses in steel beams reinforced with FRP plates and employed FE analysis to validate the analytical solution. This study concluded that FRP plate with tapered ends can significantly reduce the stress concentration compared with the untapered plate due to the linear elastic material model.

Schnerch et al. [8] determined the effect of FRP bond length on failure mode by using the FRP-strengthened superlight beams (W100×4.8 with metric designation) with an additional steel plate welded along the length of the compression flange. The beams were simply supported and subjected to four-point loading. This work defined the development length as the distance between FRP plate end and point of load application (see Figure 2.11). Development lengths were used between 51 and 203 millimeters. A various brand names of adhesive were also used to determine the adhesive with the most suitable properties for bonding to steel. Test results revealed that the effective FRP bond length for each adhesive was not equal. FRP rupture tends to occur for sufficient bond length, whereas the failure mode changes to FRP debonding for short bond length. Nevertheless, this research did not discuss on the interfacial behavior and fracture properties of specimens.

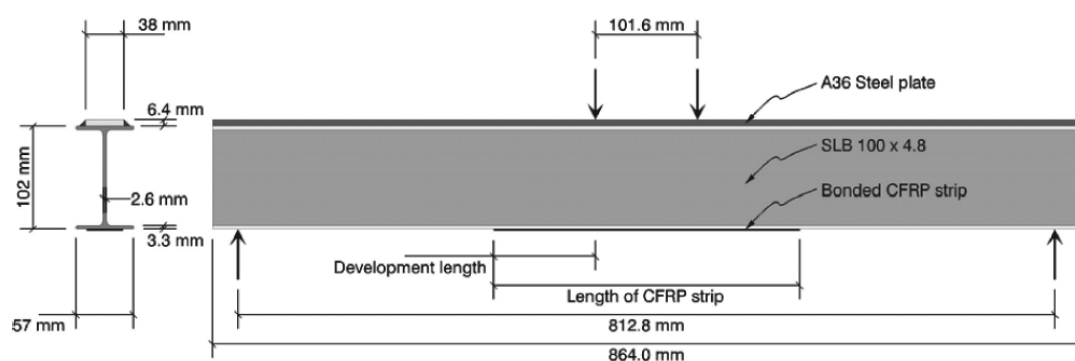


Figure 2.11 Four-point bending test of superlight beam. [8]

The issue of FRP effective bond length was also investigated by Nozaka et al. [29]. Four-point bending tests of FRP-strengthened steel beams were set as shown in Figure 2.12. Beam size was selected to prevent flange local buckling and yielding failure.

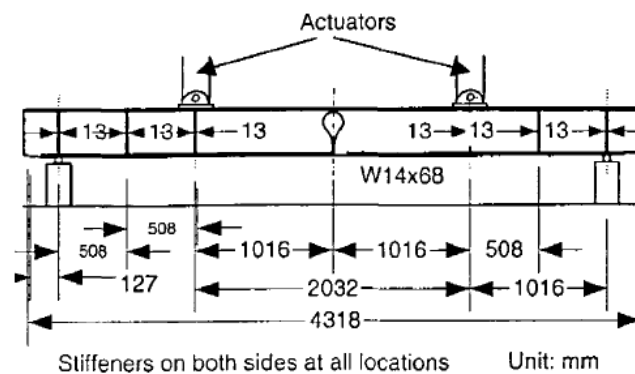


Figure 2.12 Four-point bending test of steel beams. [29]

A large hole and a slit were made at the midspan to represent a severe damage of beam. The strengthening configurations conducted in this work could be categorized into five types (see Figure 2.13). The test results shown FRP debonding occur in all specimens and there is no specimen exhibited a pure FRP rupture. Effective bond length depended on the properties of FRP and adhesive (203 millimeters for the specimen conducted in this study); furthermore, strengthening by closing the slit and creating the unbounded region (configuration 5) resulted in higher moment capacity and FRP tensile strain. Although the location of debonding was not reported in this study, the most effective strengthening configuration was addressed for the further research.

Lenwari et al. [5] stated that load-deflection curve of steel beams strengthened with FRP could be generated by employing section analysis and the principle of virtual work. Distribution of adhesive shear stress and tensile stress in FRP were derived by applying shear lag analysis. This approach was verified by their experimental results and revealed that the failure load and strengthened beams behavior could be conservatively predicted. Debonding strength is approximated in terms of stress intensity factor by taking account into the Betti's law-based reciprocal work contour integral method for two-dimensional finite element (FE) analysis [30].

There are two failure modes (plate end debonding in beams with short bonded FRP and plate rupture in beams with long bonded FRP) observed in the experiments.

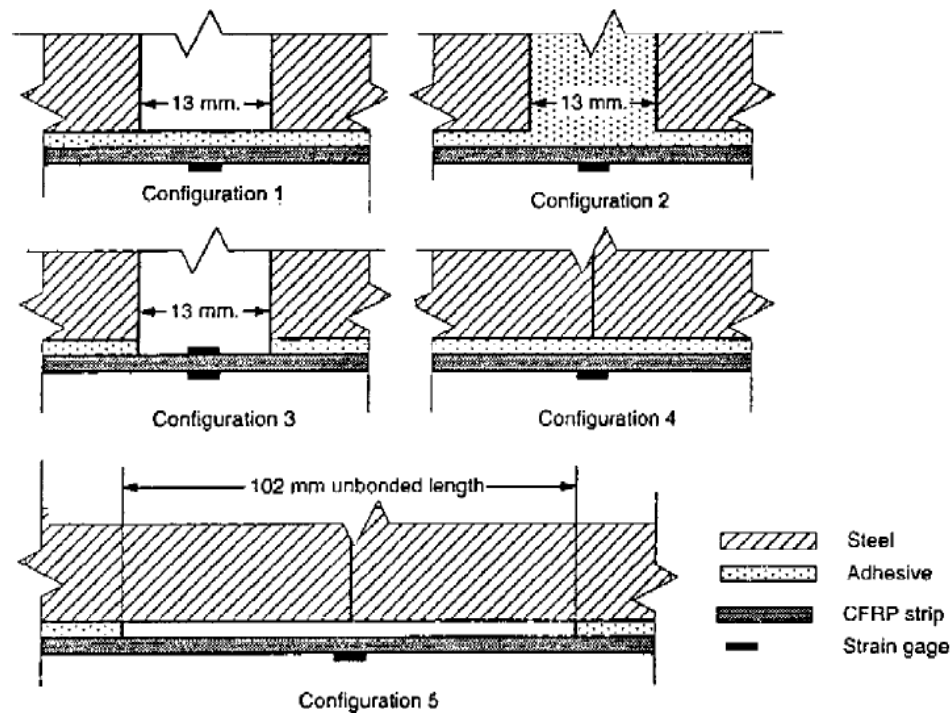


Figure 2.13 Strengthening configurations around slit. [29]

The elastic analysis with cohesive zone model was developed by De Lorenzis et al. [31] to derive the closed-form solutions of interfacial shear stress distribution in strengthened steel beams. This approach considered on the entire stages such as elastic, elastic-softening, and elastic-softening-debonding stage although the peel stress distribution was not reported. The further research [32] was conducted to achieve both of interfacial normal and shear stresses distributions within elastic stage of bond-separation model by applying coupled mixed-mode cohesive zone model. Even though simplified analytical solutions were arrived, it was only applicable to linearly elastic steel beams subjected to three-point bending load. An improved analytical solution with consideration of the Poisson's effect which is commonly neglected in the past studies was proposed by Jiang and Qiao [33] to analyze interface stresses of adhesively bonded joints or FRP-strengthened beams. The solution well predicted the interfacial stresses distribution except for the regions near the singular point.

Narmashiri et al. [34] conducted the four-point bending test of FRP strips strengthened steel beams to investigate the effectiveness of using FRP strips for flexural strengthening and examine the influences of FRP thickness and FRP elastic modulus on flexural strength and failure modes. Test setup and FRP strip configuration is shown in Figure 2.15. FRP strips bonded length was one controlled parameter in this study.

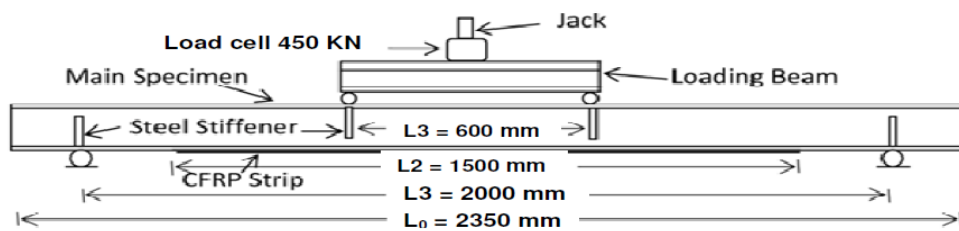
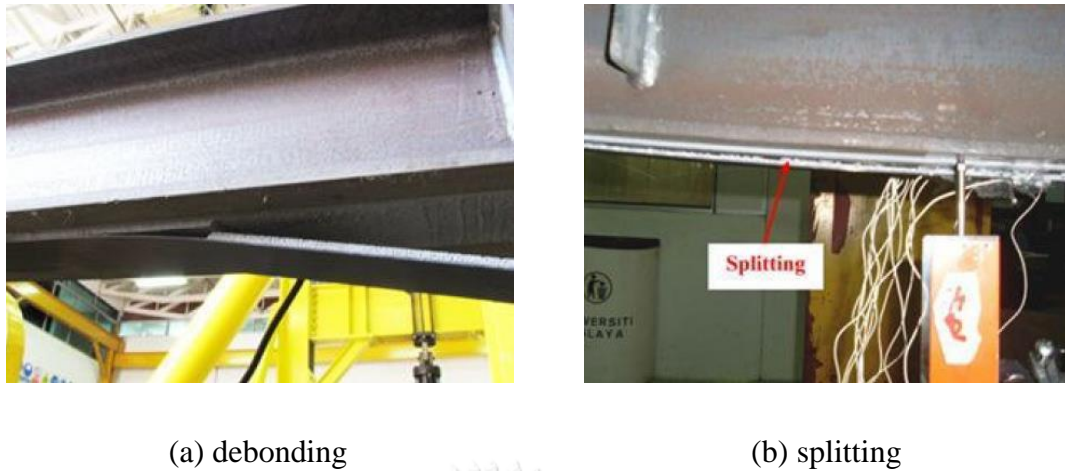


Figure 2.14 FRP strips strengthened steel beam. [34]

The results showed that the flexural capacity could be improved by increasing the FRP thickness and elastic modulus. Moreover, FRP strain at the termination point as well as the location of the applied load would reduce especially for higher load. Most specimens started the debonding process at the below load location except for the specimens strengthened by the thinnest thickness of FRP plate (1.2 millimeter) with the lowest elastic modulus (160 GPa) that started with FRP splitting at the below load location. Damages at the below load location were captured (see Figure 2.15) and all specimens failed by FRP plate end debonding. Furthermore, this study employed the nonlinear three-dimensional finite element models to predict the flexural strength of test specimens. FRP debonding was assumed to occur when the nodal plastic strain of FRP element exceed the FRP ultimate strain. It is not even obvious whether the using of constitutive relationship for modeling and the comparison of interfacial stress and strain between experimental tests and numerical simulation.



(a) debonding

(b) splitting

Figure 2.15 Damages at the below load location. [34]

Teng et al. [4] represented three-dimensional FE model to predict various failure modes of FRP-strengthened steel beams with linear adhesive. The model took account into a mixed-mode cohesive law for depicting interfacial behavior under a combination of normal and shear stresses by assuming that the interface behaves linearly elastic until damage initiation through quadratic strength criterion. Bilinear traction-separation based on Fernando's work [13] was used for modeling of adhesive. Complete interfacial failure was defined based on linear fracture energy criterion instead of Benzeggagh and Kenane (BK) criterion that widely applied by another researcher. Numerical results showed that the model was capable of accurate predictions of compression flange buckling failure, plate end debonding captured from Deng and Lee experimental tests [35].

An analytical model for the prediction of plate end debonding in FRP-strengthened steel beams was proposed by Bocciarelli et al. [36]. An approximated FRP tensile force at debonding depended on an interfacial fracture energy and maximum shear stress of adhesive. An applied load at FRP plate end debonding failure could be calculated by using the concept of mechanics of materials. The predicted failure loads are in good agreement with the previous experimental results [35, 37]. A predicted debonding loads in case of distributed loading application are calculated numerically and compared with the proposed analytical model. A completed load-deflection curve and strain distribution in FRP-strengthened steel

beams were not predicted since the research focused on the prediction of debonding load.

The effects of FRP bond length and stiffener on debonding load and failure mode of FRP-strengthened steel beams were investigated by Zeng et al. [38]. An eight steel beams were prepared and tested using a four-point flexural test as shown in Figure 2.16. In case of an absence of stiffener, the test results showed that debonding failure was observed for the beams with FRP plate that had not more than 950 mm. The beam with 1,200-mm FRP bond length failed by flange local buckling. FRP plate end debonding was found in the beams with stiffener and had not more than 950-mm FRP bond length. For the beam with stiffener and had 1,200-mm FRP bond length, the research could not conclude the failure mode because the applied load approached the maximum load capacity of the testing instrument. The presence of stiffener can avoid flange local buckling failure and improve a failure load between 8-10% compared to the corresponding beams without stiffener. FRP plate end debonding could not be prevented by using stiffener. Moreover, the research stated that a three-dimensional finite element model with a mixed-mode cohesive zone modelling could predict the load-deflection curve of the tested beams.



Figure 2.16 FRP-strengthened steel beam with a stiffener. [38]

In the preceding works, the plate end debonding was widely studied experimentally and numerically. FRP bond length as well as the material properties of FRP and adhesive was selected as variable modifications to investigate the flexural capacity and effectiveness. In the case of numerical simulation, either maximum strain criterion or cohesive law was used to simulate debonding growth in FRP-strengthened steel beams. Although FRP debonding is categorized as brittle failure

mode, some researchers [39] believed that the intermediate debonding (to be described in section 2.4) is less brittle. Intermediate debonding involves a more gradual debonding process compared to the plate end debonding. The current research will investigate an effects of various parameters on flexural properties of FRP-strengthened steel beams that FRP intermediate debonding induced.

2.4 Intermediate Debonding in FRP-Strengthened Steel Beams

FRP debonding commonly started from the location at which the interfacial shear and peeling (normal) stresses are concentrated. There are two possibilities for such failure, plate end debonding and intermediate debonding shown in Figure 2.17. A combination of high interfacial stresses at FRP plate end that depend on either insufficient FRP bond length or the use of inappropriate end anchorage for steel beams may lead to the former failure. Locations of stresses concentration that lead to the latter failure may arise from the presence of initial imperfection in adhesive layer or local yielding of the steel. However, there is not much research on intermediate debonding compared with plate end debonding [39].

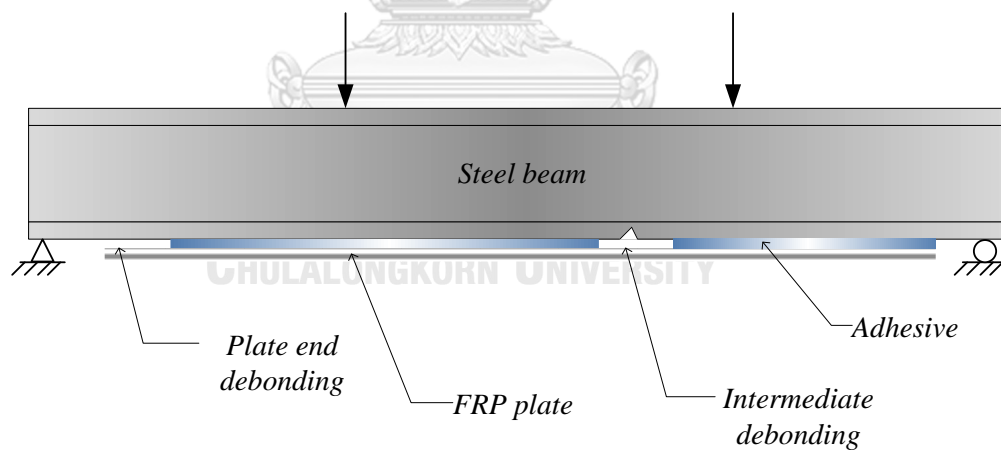


Figure 2.17 Debonding failures in FRP-strengthened steel beam.

Narmashiri et al. [40] studied the effectiveness of end-anchoring for FRP-strengthened beams by using steel plates with anchoring bolts through the four-point bending test method. Two different steel plate sizes were used at the FRP plate ends shown in Figure 2.18. This study reported that using shorter anchoring plate (100 millimeters) provides more flexural capacity and ductile than the longer anchoring

plate (200 millimeters). FRP debonding initiated at the midspan section. During an increase of applied load, the debonding propagated towards through the beam span. Strains along the FRP plate were decreased because of the presence of end anchorage.

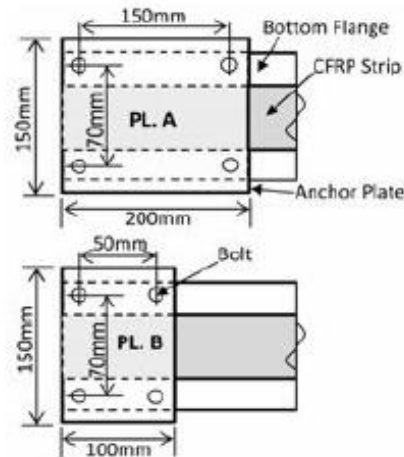


Figure 2.18 Anchoring plates at FRP plate ends. [40]

Sallam et al. [41] conducted the experimental study that reveals FRP intermediate debonding phenomena by testing of strengthened steel beams supporting concrete slab under four-point bending. Pre-intermediate debonding area was generated at the bottom surface of the lower flange by using a piece of insulated paper. The results showed that such debonding does not affect the elastic behavior since there was no growth of the intermediate debonding before steel yielding. Furthermore, beam specimens with pre-debonding area showed lower flexural strength than those with fully bonding due to intermediate debonding propagation. A limitation of this research is that the artificial debonding area is fixed. There is no alternative specimen to discuss the effects of FRP imperfection zone on both flexural and fracture properties.

Seleem et al. [42] adopted the nonlinear three-dimensional FE model that invoked the smeared crack approach for FRP-strengthened steel beam. Predicted load-deflection curves was validated against the previous experimental tests on the effect of bonded FRP plate length [5], FRP plate splicing in the constant moment region [43], and utilizing of FRP splicing near supports [44]. This approach was quite good agreement within the selected test results although a sudden crack driving force due to debonding propagation was not captured and there was no report on compression

flange buckling prediction in this study since stress-strain relationship for steel section used in this mathematical model was identical in both compression and tension.

Kim and Brunell [45] investigated the interaction between damage level in notched steel beams and FRP strengthening via experimental testing and FE simulation. Ratio between notch depth and beam depth identified damage levels and the beams were subjected to three-point loading as shown in Figure 2.19. The test results concluded that initiation of intermediate debonding was first observed near the notch location and propagated towards the termination point. Failure mode of the entire specimens was FRP bond failure followed by crack propagation through the web. Flexural behavior of beam specimens was predicted using three-dimensional FE model in which FRP elements and adhesive elements were modeled with bar element and interface element, respectively. Bilinear bond-slip curve obtained from the experiment was used to model the nonlinearity of FRP-steel interface. The accuracy of the model prediction is limited since the model neglected an occurrence of FRP debonding.

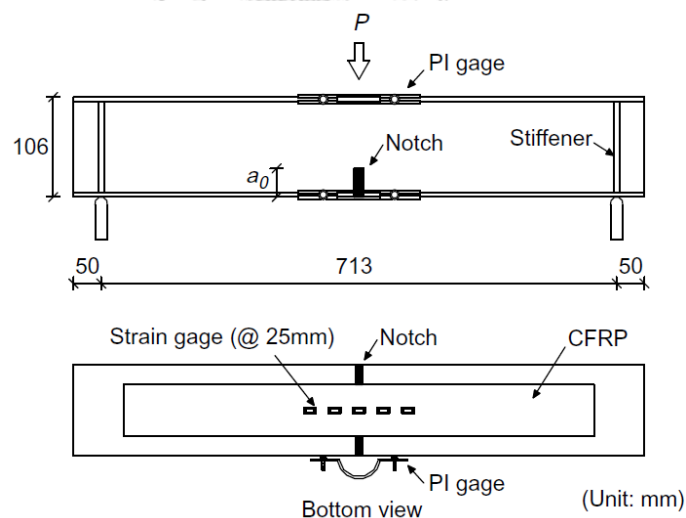


Figure 2.19 Notched beam specimen tested by Kim and Brunell. [45]

Zhou et al. [46] investigated the damage mechanism and behavior of notched steel beams strengthened with hybrid FRP through experimental tests and three-dimensional FE models. Various notch configurations are shown in Figure 2.20 to define the damage level of beams. Both ends of all beam specimens were bolted by mechanical anchorage at both FRP plate ends to ensure that the failure mode was

controlled by plate rupture. This study modified Gunes' energy dissipation equation [47] for FRP-strengthened steel beams to determine stiffness of the retrofitted beams related to plate debonding length. In FE model, adhesive layer was simulated using linearly elastic spring element. Numerical results revealed that the model was capable of predicting the load-deflection response compared to experimental test. The maximum principal strain field and the size of the plastic zone that could be calculated based on von Mises yield criterion under plane stress condition were be reliable with respected to the results obtained by the digital imaging correlations technique. However, this work did not focus on the interfacial stress distribution and bond-slip behavior.

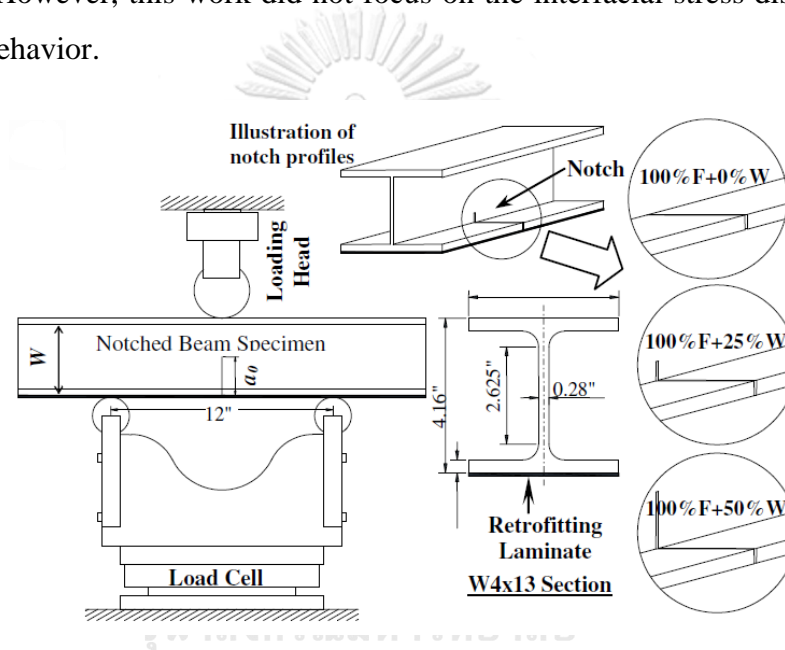


Figure 2.20 Notched beam specimen tested by Zhou et al. [46]

Teng et al. [4] attempted to generate an additional mathematical model and successfully simulated the intermediate debonding; nevertheless, there was no corresponding experimental result for verification. Another integrated closed-form solution was proposed by Deng et al. [48] to obtain both interfacial normal and shear stress distributions in FRP-strengthened notched steel beams as shown in Figure 2.21. Infinitesimal element analysis was derived with the additional expression that the interfacial stresses were maximized at the notch location. These analytical solutions were verified by their experimental tests and showed that both of peeling stress and interfacial shear stress were maximized at the notch. The solutions did not capture the

stress field in a FRP unbonded zone. Nonetheless, this research did not point out on another loading condition except for four-point bending condition.

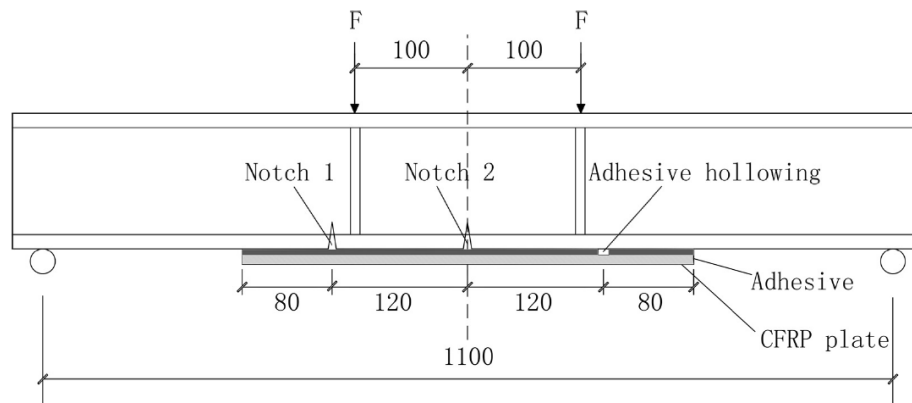


Figure 2.21 FRP-strengthened notched steel beam configuration. [48]

Karam et al. [49] conducted the four-point flexural test using 9 FRP-strengthened steel beams. The beams were notched to reduce in thickness of bottom flange by 45%, 73%, and 100%, respectively. The tested parameters consisted of notch depth, FRP thickness, and the presence of a mechanical anchorage. A galvanized bolt and FRP plate were used to anchor the FRP strengthening system of beams. The test results found that the presence of anchorage could prevent a FRP intermediate debonding in beams. The failure load of the beams was increased by retrofitting the beams using FRP system. The presence of a mechanical anchorage could provide higher failure load. In case of the beams that reduced the bottom flange thickness by 73%, the FRP strengthening and the presence of mechanical anchorage were not affected the failure load.



Figure 2.22 Anchorage system of the beam tested by Karam et al. [49]

El-Taly [50] explored the effect of notch depth and FRP anchorage configuration on strength and ductility of FRP-strengthened steel box beams. A total of 19 beams was prepared and tested under four-point flexural testing. The anchorage configurations were depicted in Figure 2.23. The retrofitting method 1 reflected the beam without an anchorage system. The retrofitting method 2, 3, and 4 revealed the beam with the FRP anchorage system by using various details. A 18-mm FRP height was used for the method 2. A 28-mm FRP height was used for the method 2 and 3. The difference between the method 2 and 3 is FRP thickness. The thickness of FRP used for the method 2 and 3 are 0.262 and 0.393 mm, respectively. The retrofitting method 5 used the FRP strips for anchoring the main FRP flexural strengthening system. The improvement of failure load and ductility index of the tested beams using the retrofitting method 5 is less compared to the other retrofitting method. The beams using the retrofitting method 5 were failed by FRP intermediate debonding. For the beams partially wrapped with FRP anchors, the failure mode was FRP rupture.

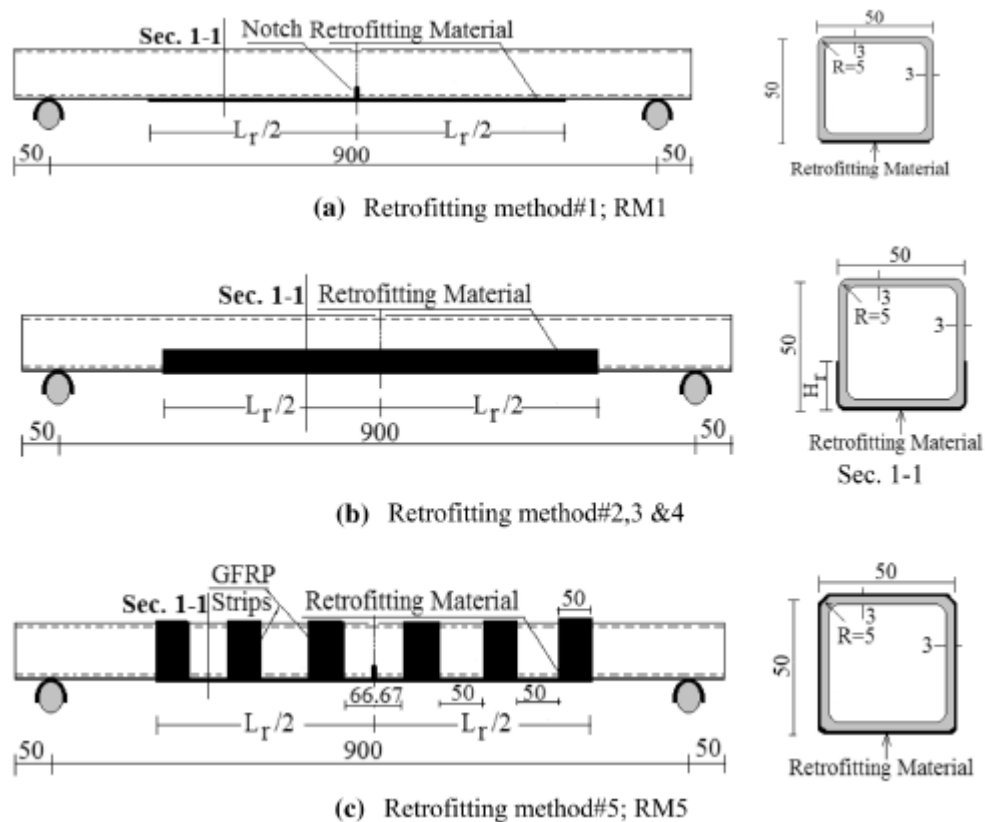


Figure 2.23 Anchorage configurations of the beam tested by El-Taly. [50]

According to the literature review, more research is needed to suggest the design recommendation of the end anchorage system for preventing FRP debonding at the termination point of FRP plates. An advantage of the intermediate debonding over the plate end debonding is recommended to focus in depth. The occurrence of intermediate debonding in FRP-strengthened steel beams without initial notch should be investigated by testing.

2.5 Fracture-Based Analysis of Intermediate Crack-Induced Debonding

Since the intermediate debonding in FRP-strengthened steel beams was not studied extensively compared with the intermediate crack-induced (IC) debonding in FRP-strengthened RC beams, this section collects the relevant works that examined the fracture processes in RC beams and proposed a fracture-based approach to capture such debonding. To develop the fracture-based analysis of FRP intermediate debonding in strengthened steel beams, it is necessary to utilize the literature that studied analytically and experimentally on the fracture properties in strengthened RC beams because there are many theorems, test procedures, and simulation concepts for FRP-strengthened steel beams that started with the corresponding approaches for strengthened RC beams.

Since FRP debonding failure in RC beams could not be predicted by conventional theory, Niu and Wu [51] performed a nonlinear fracture-based finite element analysis to study the effects of bond strength, initial flexural crack spacing, interfacial fracture energy, and the corresponding stiffness on the initiation and propagation of FRP debonding and the structural capacities. Discrete crack approach, Drucker-Prager plasticity, and elasto-plastic stress-strain relation was selected to simulate the concrete material. Elastic-perfectly plastic model was treated for reinforcing steel bars and linear elasticity constitutive law was assumed for FRP sheets without considering rupture failure. The numerical results suggested that the interfacial fracture energy was the key parameter to affect the ultimate load capacity of structures because the higher interfacial fracture energy yields a large FRP bond length and requires more external work to create the interfacial debonding, while the flexural crack spacing was less affected. The bond strength and the stiffness of FRP-concrete interface only affected the yield load and had no significant influence on the

ultimate load capacity. However, there was no report of comparing between the numerical model and the test results in this research.

Empirical formulas for predicting interfacial fracture energy, and the FRP effective bond length was developed by Wu and Niu [52]. Bond stress-slip curve proposed by Nakaba et al. [53] was used to generate the formulas and this work proved that such parameters depended on the compressive strength of concrete. The proposed solutions were compared to the previous literature that conducted the NES single shear test on FRP bonded concrete blocks. It is important to note that such formulas could be applied to certain values of the concrete strength (24 to 58 MPa).

A fracture-based analytical model for determining the FRP debonding load in concrete beams was proposed by Achintha and Burgoyne [54]. This model assumed that the concrete and FRP behaved linear elastic for calculating the internal strain energies which were threefold: The strain energy due to flexure, the strain energy due to axial force induced by considering separately the state of stresses in the original RC beam and the FRP plate (see Figure 2.24), and the strain energy in the FRP plate. Neutral axis depth of beams was computed from the conventional section analysis with Branson's approach [55]. FRP force distribution in bonded zone was determined based on Täljsten's expression [56]. Crack driving force was calculated from the total energy loss due to the FRP debonding process to investigate the sufficient condition for crack propagation through the fracture toughness. This work considered that fracture process in concrete grew locally in a pure mode I (peeling). The results showed that the FRP plate end debonding would occur since the FRP terminal distance was more than the certain value that induced the crack driving force higher than the fracture toughness. For the IC debonding, the model could be revealing the crack driving force by varying the predefined crack length and its location. FRP plate end debonding normally occur at lower applied load, whereas IC debonding often takes place at high applied load.

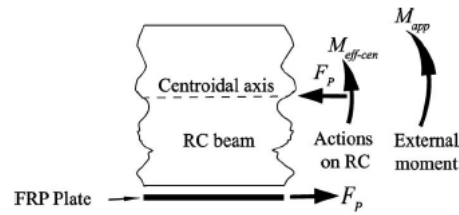


Figure 2.24 Applied load in RC section. [54]

Experimental work aimed at investigating FRP debonding failure modes and the effectiveness of FRP-strengthened concrete beams was conducted by Gunes et al. [47]. The test configuration is shown in Figure 2.25. All beams were strengthened in flexure using the same FRP plates by following the ACI 440 Guideline [57], which specified the FRP limited strain to prevent debonding failure. Shear reinforcing steels size was enlarged only in specimen S2PF7M to investigate the influence of increased shear load capacity on the flexural load capacity. FRP anchorage by half and full shear span was performed in specimen S3PS1M, S3PS2M, S4PS1M, and S4PS2M to study the effects of the spatial extent of shear strengthening along the beam span. FRP shear strengthening configuration was twofold: side bonded plates (specimen S3PS1M and S3PS2M) and L-shaped plates (specimen S4PS1M and S4PS2M).

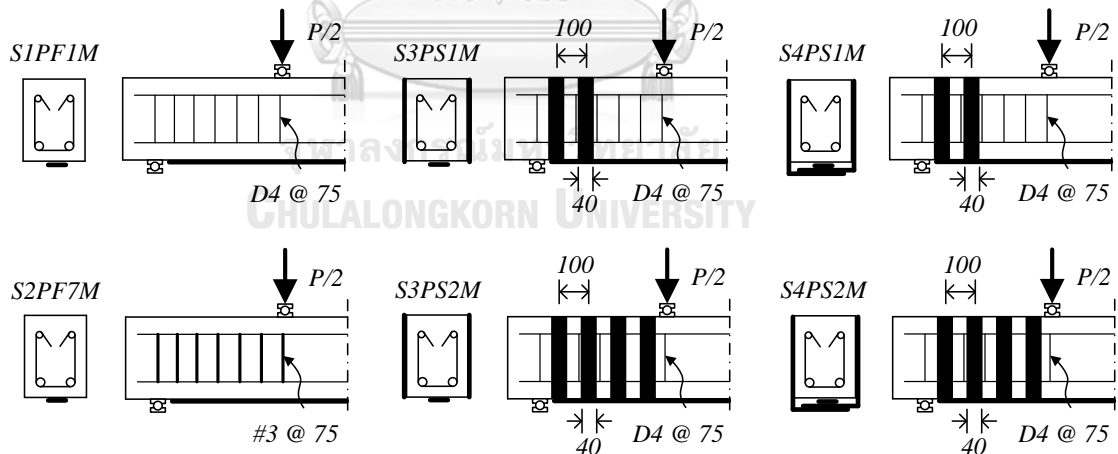


Figure 2.25 Beam specimens in Gunes's research. [47]

The experimental results demonstrated that the specimen S1PF1M that designed only from the ACI 440 approach [57] was found the concrete cover delamination and followed by shear failure. Such failure was unfavorable and more brittle than should be expected. Other specimens except for S1PF1M were failed by FRP debonding

failure. Plate end debonding was occur in specimen S2PF7M, S3PS1M, and S3PS2M while IC debonding due to stress concentration along the constant moment region was initiated in specimen S4PS1M and S4PS2M. The performance of the beam specimen S4PS2M was remarkable both in load capacity and ductility. Furthermore, the fracture-based analytical approach was also proposed to predict the load behavior of FRP-strengthened concrete beam. The model could reasonably predict the load-deflection relationship of strengthened beam, especially for the strengthened beams in flexure and shear with FRP anchorage (specimen S4PS2M). However, this model could not capture the location of FRP debonding and generated the load-deflection curve by considering the FRP anchorage system because the energy dissipation due to the end anchorage system is the assumed value in the absence of mode II (sliding) interfacial fracture energy testing.

Wantanasiri and Lenwari [58] proposed the fracture-based model adapted from Wu and Niu [52] and Achintha and Burgoyne [54] models to predict IC debonding failure load in FRP-strengthened concrete beams. Previous experimental studies on RC beams strengthened with FRP were used to verify the accuracy of the presented model and the predicted load capacity by considering the FRP limited strain to prevent debonding [57] was calculated to compare with the model. The results showed that the proposed model could produce good agreement with the preceding test data, while the ACI approach could not successfully predict the failure mode in the certain cases. Moreover, this research examined the effects of FRP modulus, FRP reinforcement ratio, steel reinforcement ratio, and the compressive strength of concrete on the debonding load. From the parametric study, the steel reinforcement ratio was the most influential parameter on debonding load. The entire parameters showed the same trends that was directly varied with debonding load, except for the FRP reinforcement ratio that could decrease the load capacity and another failure mode may occur when it increased beyond a certain value.

The preceding research may give an inspiration to develop of fracture-based model for an analysis of intermediate debonding in steel beams strengthened with FRP because the knowledge of such findings is very limited at this time.

CHAPTER 3

EXPERIMENTAL PROGRAM

In an attempt to investigate the bond behavior and flexural behavior of the FRP-strengthened steel beams, it was decided to conduct three parts of experiments. Material properties evaluation was firstly performed to compare between tested properties and the corresponding values taken from manufacturer's data. The second experiment was a single lap shear test in which joint specimens were prepared to examine the bond behavior. Bond-slip curves were calculated from the test results. Interfacial fracture energies were determined to use for the prediction of intermediate debonding in steel beams strengthened with FRP plates. The third testing fabricated the FRP-strengthened steel beams with various design parameters such as FRP modulus, initial bond defect, FRP bond length, and loading conditions. Effects of such parameters on flexural responses were explored.

3.1 Specimens

Two hot-rolled wide-flange sections were selected to conduct an experiment in this research. SS400 steel grade was used. The section W150×14.0kg/m was prepared with a length of 2,000 mm and used for the beam specimens. To avoid failure mode due to compressive yielding, steel plates were welded to the top flange of each beams as shown in Figure 3.1. Steel plate was 300 mm in width and 12 mm in thickness.

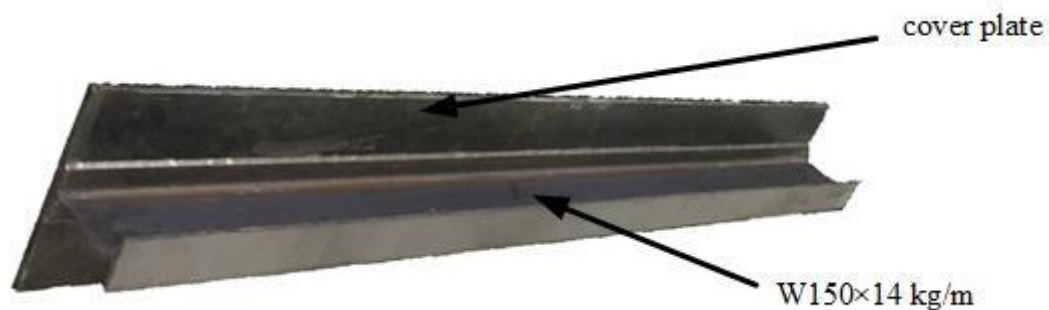


Figure 3.1 Beam specimen welded with steel cover plate.

Surface of steel beams and steel cover plates were initially cleaned by brushing and grinding before welding. Welding procedure was shielded metal arc welding (SMAW) as shown in Figure 3.2. E6013 with 3.2 mm diameter were used as filler metal. Direct current electrode negative (DCEN) was set as polarity welding. Range of welding current was between 95-125 A. Welding travel speed was about 80-100 mm/min.



Figure 3.2 Welding between steel beam and cover plate.

The section W150×31.5kg/m was cut to 500 mm and used for the joint specimens. Two types of CFRP plates (i.e. Sika® CarboDur® S512 and Sika® CarboDur® M514) were used to investigate an effect of FRP modulus on flexural response of strengthened beams. FRP plate is 50 mm in width. Thickness of FRP plates is 1.2 mm and 1.4 mm for Sika® CarboDur® S512 and Sika® CarboDur® M514, respectively. The bonding between steel specimens and FRP plates was performed using thixotropic-based adhesive tradenamed as SikaDur®-30.

3.1.1 Material Properties

There were two materials (i.e. steel and CFRP plate) tested in material properties evaluation. The tested materials were prepared from portions of steel beams, steel plates, Sika® CarboDur® S512, and Sika® CarboDur® M514. All materials were prepared in coupon. Steel coupons cut from the flat regions of flange of wide-flange beams as in ASTM A370 [59]. Tensile test, as shown in Figure 3.3, consisted of measuring yielding stress, yielding strain,

and elastic modulus were conducted for steel coupons. Rupture stress and elastic modulus of CFRP coupons were obtained from the identical test. All coupon specimens were tested under displacement control at a rate of 1mm/min until coupon failure occurs.

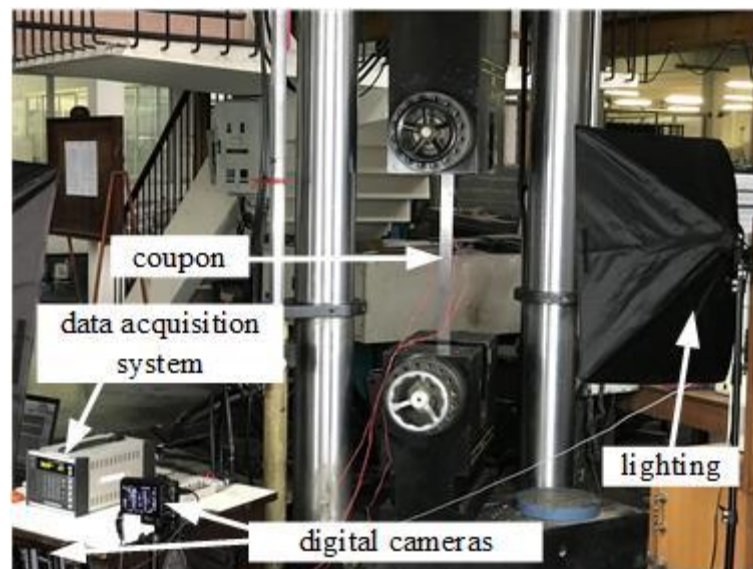


Figure 3.3 Tensile test set-up.

Material properties of coupons are reported in Table 3.1. Note that E is elastic modulus, σ_y is yield stress of steel, and σ_{fu} is tensile stress of CFRP plate. A related hypothesis maintains that elastic modulus of steel is equal to 210,000 MPa, suggesting that manufacturer's data did not report the value of steel modulus [60].

Table 3.1 Material properties of steel and CFRP.

Material	E (MPa)		σ_y (MPa)		σ_u or σ_{fu} (MPa)	
	Manufacturer data	Coupon tests	Manufacturer data	Coupon tests	Manufacturer data	Coupon tests
Steel beam	-	178,091	361	318	479	458
Steel plate		182,590	356	284	457	397
Sika® CarboDur® S512	160,000	180,777	-		2,800	3,303
Sika® CarboDur® M514	200,000	238,575			2,900	2,522

Material properties of SikaDur®-30 is estimated based on the manufacturer data [61] since many works [22, 23, 62-66] had proved that the variation of their properties were relatively low. Elastic modulus and tensile stress of SikaDur®-30 is 11,200 MPa and 31 MPa, respectively. There is only tested elastic modulus and tensile stress of Sika® CarboDur® S512 coupons that meet the expected values from specification. Tested elastic modulus of steel is less than the expected modulus (i.e. 210,000 MPa) about 13-16%. Yield stress of steel obtained from tensile test is lower than manufacturer's data about 12-20%. Tested tensile stress of steel is also less than the expected value about 5-13%. Elastic modulus of Sika® CarboDur® M514 coupons meet the manufacturer's data but tensile stress obtained from testing is lower than the expected value about 13%. These results highlight that material properties evaluation is one of the necessary steps to indicate true strength of materials before performing larger scale experiments or another computation.

3.1.2 Surface Preparation

Adhesive strength of FRP-steel interface can be improved by producing surface preparation before FRP strengthening. Sandblasting was chosen because this method is easy installation and relatively cheap [67]. The other benefit for surface preparation by sandblasting is to avoid interfacial failure between steel and adhesive [68]. SA3 grade sandblasting was provided for the bottom flange surface of all steel specimens tested in this research. This abrasive blasting grade cleans the surface to visually clean steel condition and classified according to ISO 8501-1 [69]. A comparison between Figure 3.4(a) and Figure 3.4(b) shows that the surface color of the bottom flange of specimens changed from metal color to near white color. Roughness level is improved by visual inspection.

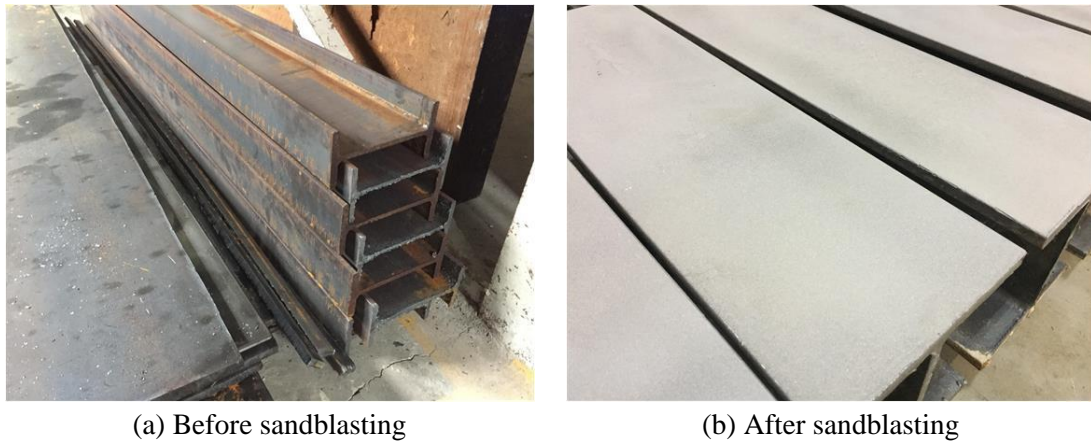


Figure 3.4 Metal surface preparation.

Previous studies performed FRP installation within 24 hrs after sandblasting [22, 23] or gritblasting [13, 64]. The main goal is to minimize potential contamination on a steel surface resulted in some rust or unresolved interface defect. This work concerns on this issue and decides to adhesively bond CFRP plate to steel specimens within 3 hrs after sandblasting. Adhesive hardening time was 1 month to ensure the bond between steel and FRP.

3.1.3 Initial Bond Defects Creation

A polyester film-based insulation paper as shown in Figure 3.5(a) was used to generate an initial bond defect at the interface between steel and adhesive. The insulation paper was 0.25 mm in thickness.



(a) Insulation paper



(b) Paper position before FRP strengthening

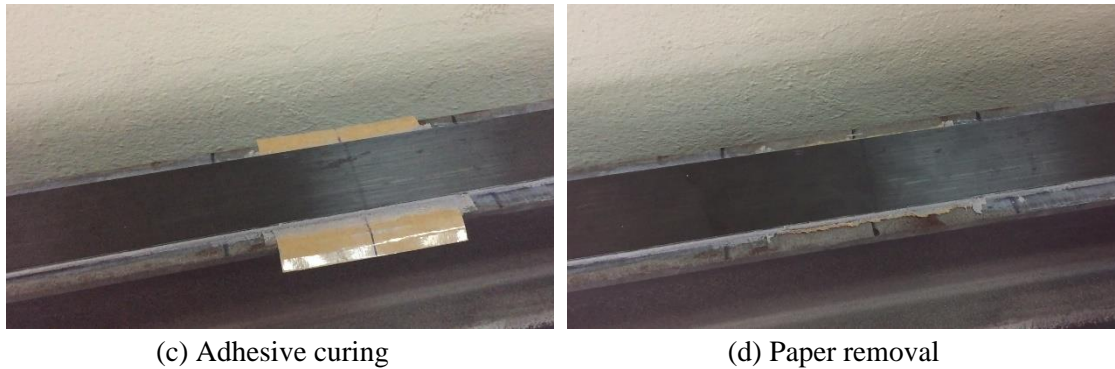


Figure 3.5 Defect creation.

Before installation of CFRP plates, the insulation paper was positioned on the steel specimens as presented in Figure 3.5(b). It can be seen from Figure 3.5(c) that insulation paper was attached to steel specimens throughout the adhesive curing time. Figure 3.5(d) illustrates that insulation paper was removed from the steel substrate before testing. According to visual inspection as shown in Figure 3.6, this insulation paper can be proved that hardened adhesive would not leak onto the steel surface.

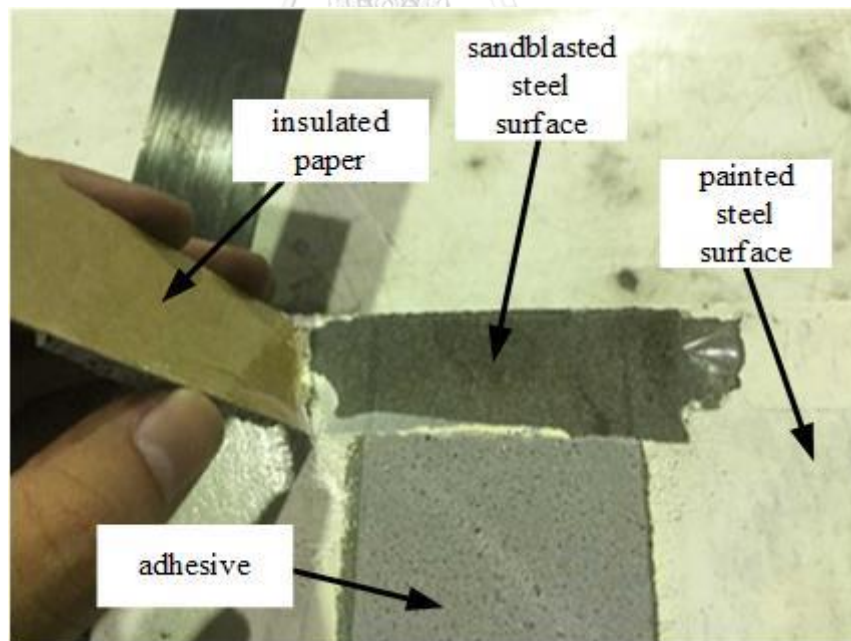


Figure 3.6 Adhesive proof using insulated paper.

3.1.4 Joint Specimens

Eight joint specimens were conducted on single lap shear test to study the bond behavior of the FRP-steel interface. Details of joint specimens prepared for single lap shear test are described in Table 3.2. The FRP bond length (l_{frp}) is defined in Figure 3.7.

Table 3.2 Specimen designation in single lap shear test.

Joint	FRP type	Defect type	l_{frp} (mm)	t_a (mm)	a_0 (mm)
JSI75-25	Sika® CarboDur® S512	Interfacial defect	75	3.5	25
JSI150-25			150		
JSI250-25			250		
JSI400-25			400		
JSU400-25	Sika® CarboDur® M514	Unbonded zone	400	-	-
JMU400-0			4.3	25	
JMU400-25			3.6	50	
JMU400-50					

The investigated parameters in single lap shear test consisted of FRP modulus, defect type, and initial bond defect length. Adhesive thickness and initial bond defect length are denoted by the symbol t_a and a_0 , respectively. Figure 3.7 illustrates that the defects induced in this study can be categorized into two types (i.e. unbonded zone and interfacial defect). This may be an issue on fracture resistance due to adhesive fracture between intended defect (unbonded zone) and unresolved defect (interfacial defect).

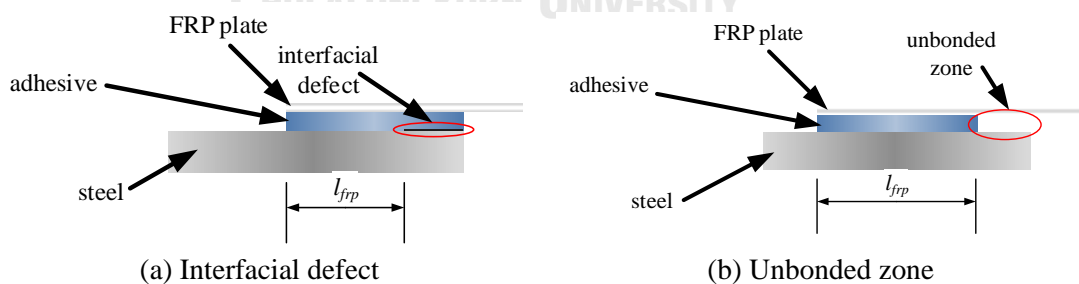


Figure 3.7 Examined defect types.

3.1.5 Beam Specimens

There were thirteen specimens of FRP-strengthened steel beams prepared for flexural test as presented in Table 3.3. The span length of all beam specimens was 1,800 mm.

Table 3.3 Details of beam specimens.

Beam	FRP type	Loading type	$l_{frp}(mm)$	Preloading	$2a_0(mm)$		
CBM	-	Monotonic	-	-	-		
CBMY				Yes			
BMM120-0	Sika® CarboDur® M514		120	-	50		
BMM120-50				Yes	100		
BMM120-100			150			-	-
BMM120Y-100				120	Yes		
BMM150-100	Sika® CarboDur® S512		120			-	-
BSM120-0				Yes	100		
BSM120-100							
BSM120Y-100	-		-				
CBP				-	-	-	-
BMP120-100	Sika® CarboDur® M514		Periodic unloadings	120	-	100	
BSP120-100							Sika® CarboDur® S512

Flexural test conducted in this research concerns the following parameters: FRP modulus, loading type, FRP bond length (l_{frp}), preloading, and initial bond defect length ($2a_0$). Preloading was applied in beam CBMY, BMM120Y-100, and BSM120Y-100 to simulate the damaged condition where service residual stress had occurred in the beams. Beam CBMY was prepared by utilizing beam CBM after testing. Beam BMM120Y-100 and BSM120Y-100 were set by using pilot beam pBMM120-100 and pBMM120-200. The symbol “p” indicates the pilot testing that conducted to check and improve the experimental system. Results of two pilot beams are not discussed in this work. Level of preloading was defined by the ratio between strain value at top surface of bottom flange and coupon yield strain of steel. It was found that the mentioned ratio of beam CBMY, BMM120Y-100, and BSM120Y-100 are equal to 8.18, 8.55, and 6.37, respectively.

3.2 Test Setup and Instrumentation

3.2.1 Test Configuration

FRP-steel joint specimens were tested under tensile loading in Universal Testing Machine of 1,000 kN capacity manufactured by Instron as shown in Figure 3.8. Each specimen was placed in supporting frame to prevent bending moment during the test.

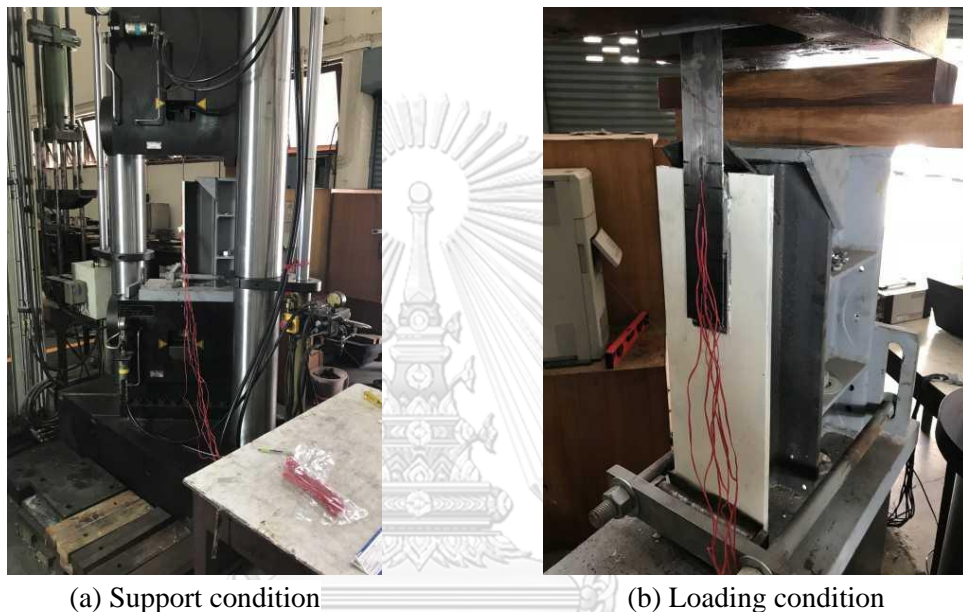


Figure 3.8 Overview of single lap shear test.

The test was performed under displacement control until failure. Crosshead speed was controlled at 5 mm/min. Strain and tensile force values were recorded with a data logging system during the test. A sampling rate of 5 Hz was used for the investigation of bond behavior of joint specimens. Geometry and size of supporting frame are illustrated in Figure 3.9.

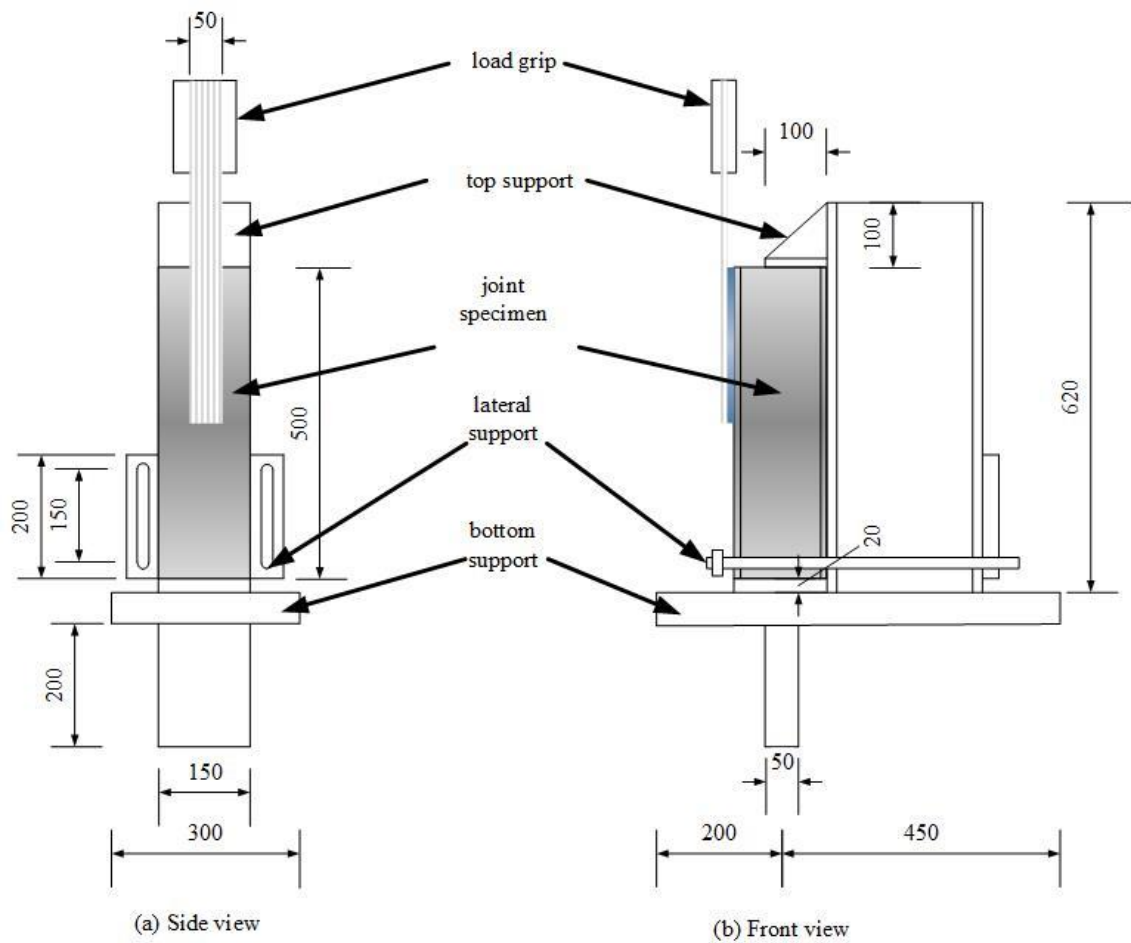


Figure 3.9 Details of supporting frame for single lap shear test (all dimension in mm).

A four-point flexural test was conducted as shown in Figure 3.10. A spreader steel beam positioned on the steel beam specimen induces two concentrated loads. The spacing between two applied loads was 150 mm.



(a) Support condition



(b) Loading condition

Figure 3.10 Four-point flexural test set-up.

The tested beams were placed on the steel rollers, which allow the beams to behave in a simply supported manner. For the monotonic loading type, beams were manually applied load with a displacement rate of 1mm/min using a 300 kN capacity hydraulic jack. The applied load was also with a displacement rate of 1mm/min. During an unloading period for periodic unloading type, midspan deflection was released to zero within 1 min to minimize the testing time and structural health recovery.

The midspan deflection after fully unloaded cannot be zero in subsequent cycles because of the permanent damage in beams. The test was continued and increasing displacement rate of 1mm/min was applied even as long as beam was not failed. According to unloading curve of nanoindentation polymers, it was observed that a fast unloading rate results in less recovery during unloading [70].

3.2.2 Strain Gage Locations and Designation

This research collected strain data by using data acquisition system as shown in Figure 3.11. A dual sampling rate was chosen to record two type of data. A 5 Hz sampling rate was used for the investigation of static behavior of joints and beams. A sampling rate of 100 Hz was selected to capture an abrupt event triggered by FRP intermediate debonding and FRP rupture. Joints were collected strain and applied load data. Beams were recorded strain, deflection, and applied load data.

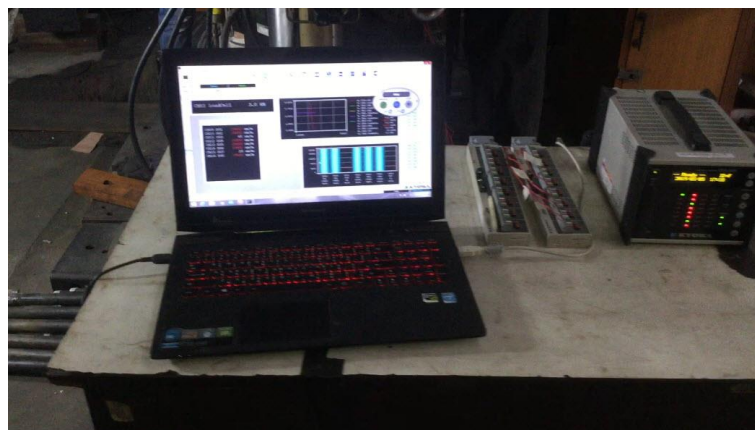


Figure 3.11 Data logging system.

Electrical resistance strain gages were installed to measure the strain distribution in joints and beams. Strain gages is denoted by “SG”. For joint specimens, single lap shear test was stopped when FRP plate was found to be rupture or debonding. Details of strain gage installation for joint specimens are illustrated in Figure 3.12. Strain gage spacing in the first 150mm from loaded end is equal to 25mm. For the distance from loaded end further than 150mm, strain gage spacing is equal to 50 mm.

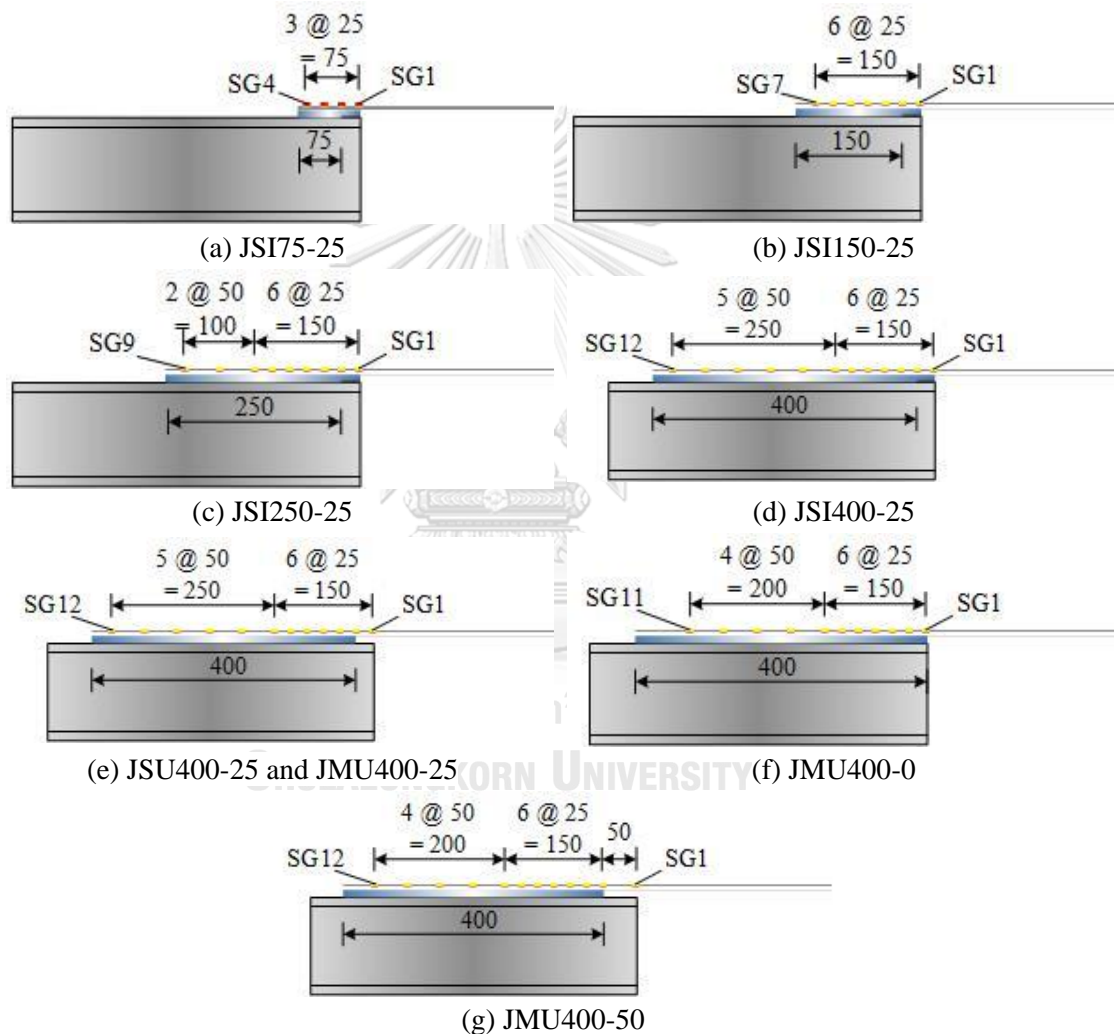


Figure 3.12 Instrumentation on joint specimens (all dimensions in mm).

Displacement transducers were installed to measure the deflection of beam specimens. Displacement transducers is denoted by “DT”. According to the instrumentation on beam without FRP strengthening as shown in Figure 3.13, SG1 was installed at the bottom surface of the bottom flange. SG2

located at the upper surface of the bottom flange. SG3 and SG4 was installed at mid-height of the W150×75 section and the bottom surface of the top flange, respectively. The compressive strain at top surface of the steel cover plate was measured by SG5. Three displacement transducers measured the deflections at midspan and locations near the CFRP plate terminations (refer to specimens strengthened with FRP plate).

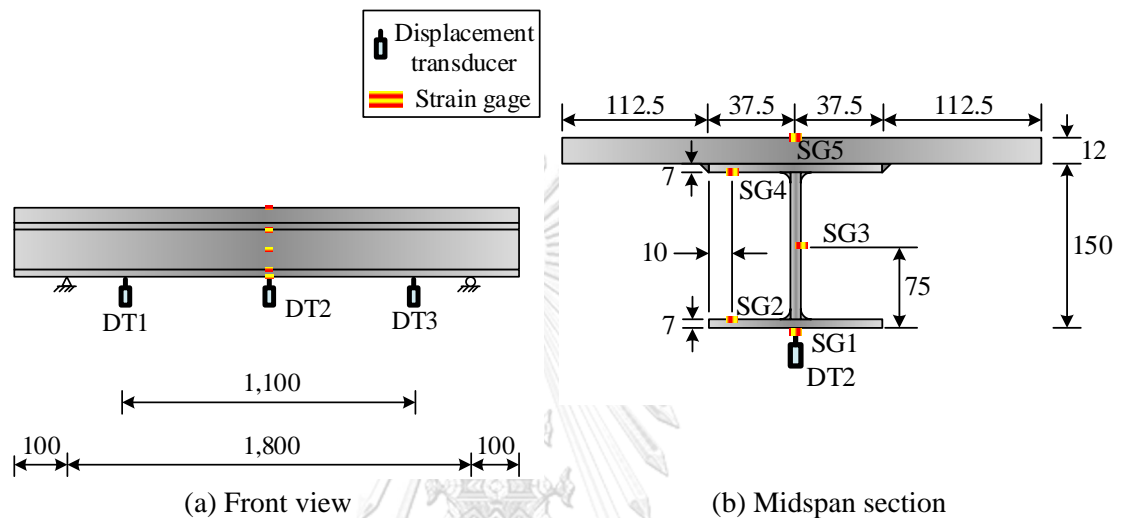


Figure 3.13 Instrumentation on unstrengthened steel beams (all dimensions in mm).

FRP strains were measured with nineteen strain gages as shown in Figure 3.14 for beam specimens strengthened with FRP. There are thirteen strain gages which were attached on the CFRP plate. Six strain gages were installed on the steel beam and cover plate to measure axial strain in steel. Note that $2a = 50$ for beam BMM120-50 and $2a = 100$ for the other FRP-strengthened beams. FRP bond length (L_f) is equal to 1,500 mm for beam BMM150-100 and $L_f = 1,200\text{mm}$ for the other FRP-strengthened beams.

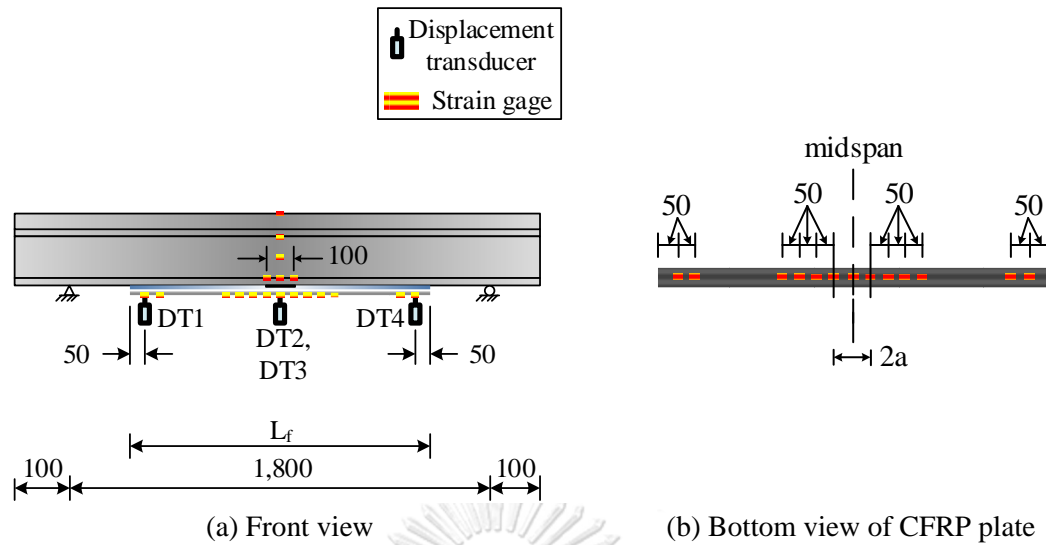
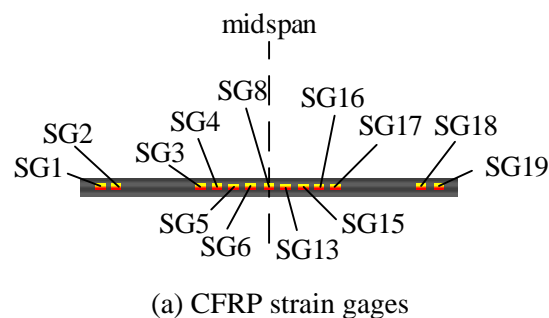


Figure 3.14 Instrumentation on FRP-strengthened steel beams (all dimensions in mm).

Strain gage locations for FRP-strengthened steel beams are depicted in Figure 3.15(a). SG1, SG2, SG18, and SG19 were used to detect the debonding near the plate ends, while SG3-SG6, SG13, SG15-SG17 were used to detect the intermediate debonding. SG8 was used for the FRP tensile strain at midspan. The bottom flange yielding within the initial bond defect zone was observed from three strain gages SG7, SG9, and SG14 at the steel bottom flange. Additional strain gages were also installed to measure the strain distribution across the midspan section, as shown in Figure 3.15(c). However, typical strain signals for the detection of steel yielding, fiber rupture, and intermediate debonding will be presented in the paper.



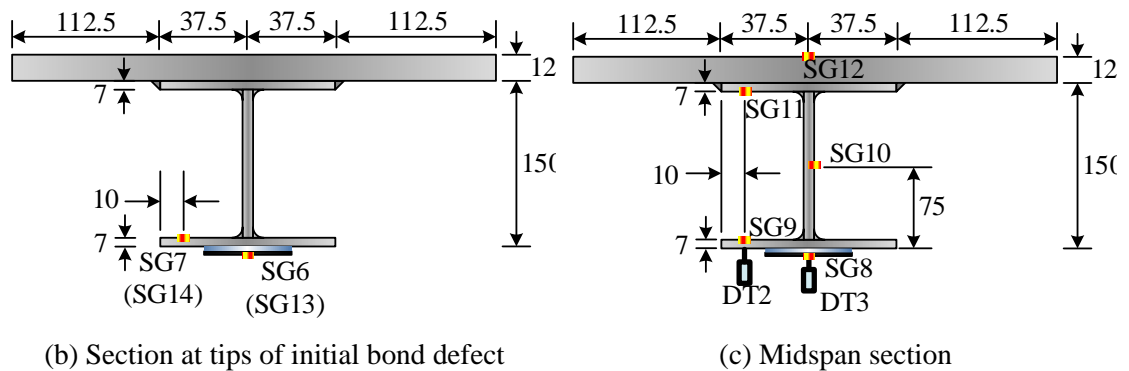


Figure 3.15 Details of instrumentation on CFRP plate and steel beam
(all dimensions in mm).

For beam CBM, the test was terminated when the compressive strain at the steel cover plate reached 75% of yield strain of the steel plate. Last value of midspan deflection in beam CBM would use for an application of maximum midspan deflection. For beam strengthened with FRP, the test was stopped when FRP plate was found to be rupture or debonding as same as joint specimens.

CHAPTER 4

BOND BEHAVIOR OF FRP-STEEL INTERFACE

Interfacial behavior between steel and FRP can be explained by experimental results obtained from FRP-steel joint specimens under single lap shear test. This section examines the failure mode of FRP-steel joint specimens with three different bonding conditions: fully bonded steel-FRP interface, unbonded zone, and interfacial defect. Images of FRP-steel joint specimens at failure were also produced at frame rates of 1,000 frames per second using digital camera. Development of strain along the FRP bond length as well as interfacial fracture energy calculated from bond-slip relationship were also investigated. FRP strain distribution can be represented an influenced region of FRP plate that affected by external applied load. Effective bond length can be found by considering distribution and level of development of FRP strain. Moreover, it is necessary to calculate interfacial fracture energy of FRP-steel interface, particularly when used for the prediction flexural responses of FRP-strengthened steel beams with an initial bond defect.

4.1 Failure of Joint Specimens

The time when failure occurred in fully bonded FRP-steel joint specimens was captured as shown in Figure 4.1. FRP plate started debonding from the free end and propagated to the loaded end. Some parts of the FRP plate still attached to an adhesive in the region of free end. This may be caused by the dramatically different of peeling stress between top and bottom interface of adhesive in the vicinity of free end. Such different of peeling stress can be expressed in the mathematical model developed by Jiang and Qiao [33].



Figure 4.1 Visible failure of joints without initial bond defect (joint JMU400-0).

Typical state at the time when the failure occurred in steel-joint specimens with initial bond defect are presented in Figure 4.2. Unlike FRP-steel joint specimens with an initial bond defect, the captured images showed that FRP plate debonding was not started at the free end. Intermediate curvature of FRP plate was instead found in the specimens with either interfacial defect or unbonded zone. This can be explained by observing that FRP intermediate debonding may be induced by the presence of initial bond defect.



(a) Interfacial defect (joint JSI400-25)

(b) Unbonded zone (joint JSU400-25)

Figure 4.2 Visible failure of joints with different defect types.

It can be seen by visual inspection of FRP-steel joint specimens after the testing that FRP plates were detached from the adhesive. Surfaces of FRP plates and adhesives of joint specimens with interfacial defect after the testing are shown in Figure 4.3. Joint JSI75-25 seems to have the most area of FRP delamination compared to its whole FRP bonded area. FRP delamination area can be observed from the area of FRP plate that still attaches to adhesive surface. Joint JSI75-25 showed that the FRP delamination area may take approximately 50% of its whole bonded

area. Interestingly, the FRP delamination area with respected to the whole bonded area decreased as the FRP bond length increase. Longer FRP bond lengths may reduce the length of region that has undergone the dramatically different of peeling stress in the vicinity of free end.

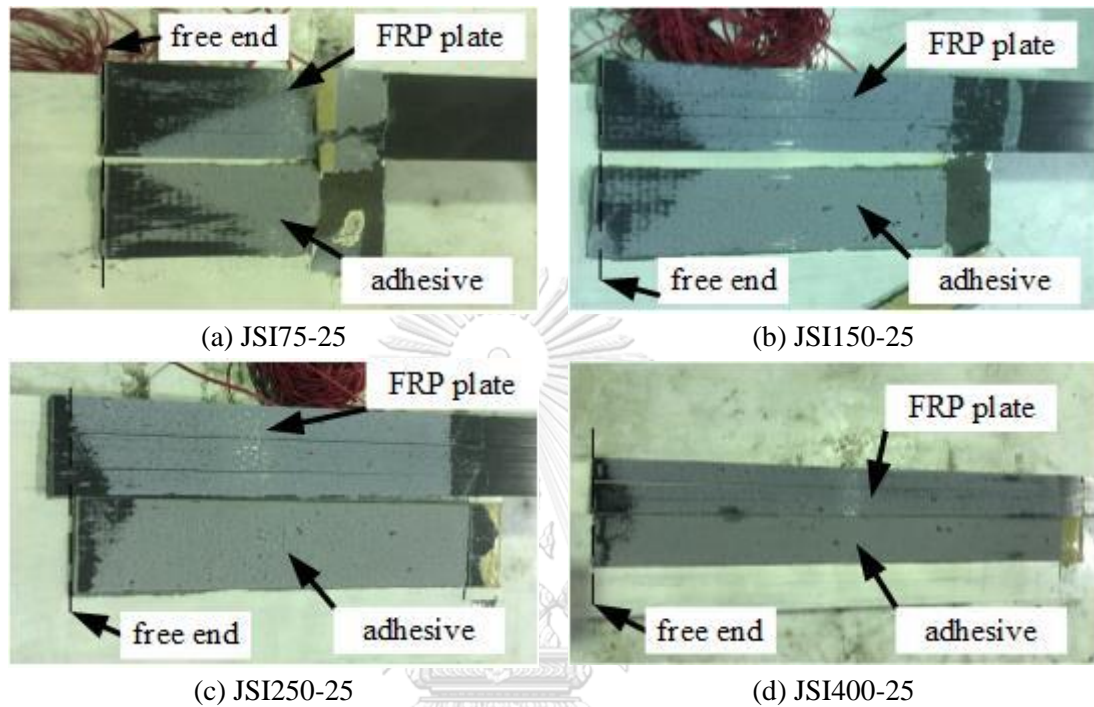


Figure 4.3 Failure surface of joints with interfacial defect.

Surfaces of FRP plates and adhesives of joint specimens without interfacial defect after the testing are also depicted in Figure 4.4. The FRP delamination area could not be equalized even through the identical FRP bond length was provided. In case of an increased unbonded zone length, increasing FRP delamination area trend became not obvious after an unbonded zone length is equal to 50 mm. The FRP delamination area of joint JMU400-50 was less compared to JMU400-25 as seen in Figure 4.4(d). Moreover, the FRP delamination area with respected to the whole bonded area increases as the FRP modulus increases.

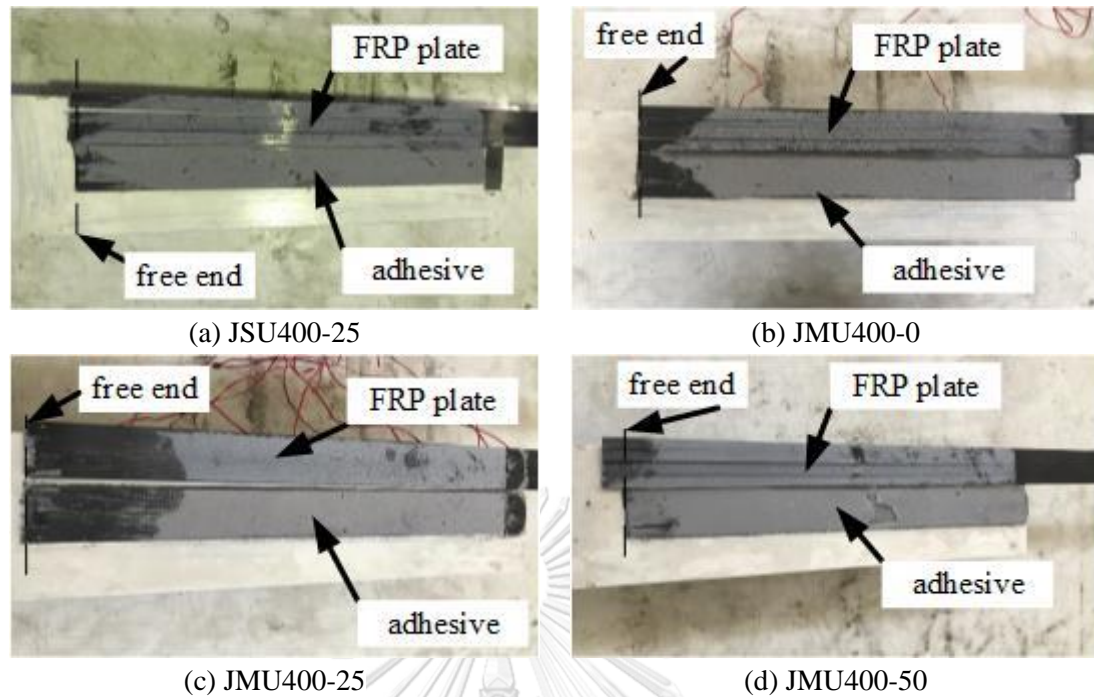
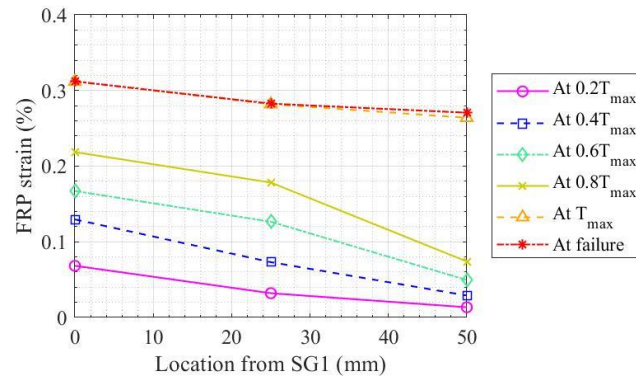


Figure 4.4 Failure surface of joints without interfacial defect.

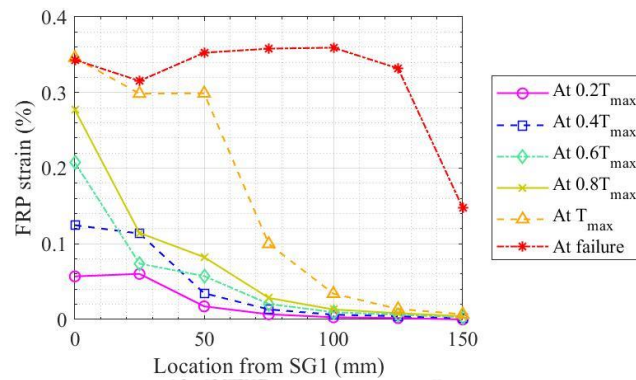
According to the comparison between joint JSI400-25 and JSU400-25, the FRP delamination area of joint JSI400-25 seems to be less than the corresponding area of joint JSU400-25. This may be implied that there are some correlations between the FRP delamination area and defect types. The presence of interfacial defect within FRP-steel interface likely reduces the length of region that has undergone the dramatically different of peeling stress compared to the presence of unbonded zone.

4.2 Strain Development in FRP plates

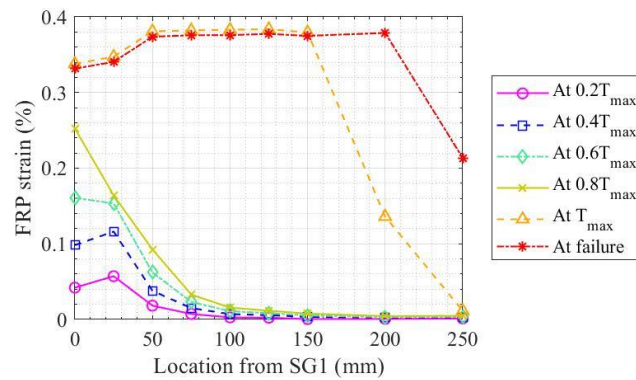
The first raw data set obtained after the single lap shear testing are applied tension and axial strain at various locations along the FRP plate. Figure 4.5 and Figure 4.6 plot the FRP axial strain distribution started from the location near the loaded end. SG1 is the strain gage nearest to the loaded end. Each plots were produced by increasing the applied tension increment until the maximum applied tension was reached in the specimens. Applied tension increment for plotting is equal to 20% of maximum applied tension (T_{max}). After the maximum applied tension was reached, the specimens could resist a few deformation before failure. The development of FRP strain at failure was also plotted.



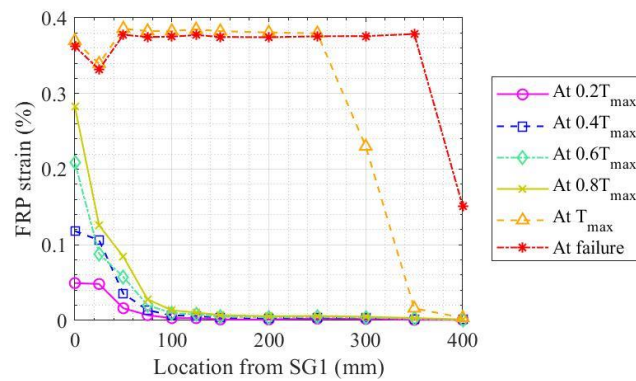
(a) JSI75-25



(b) JSI150-25

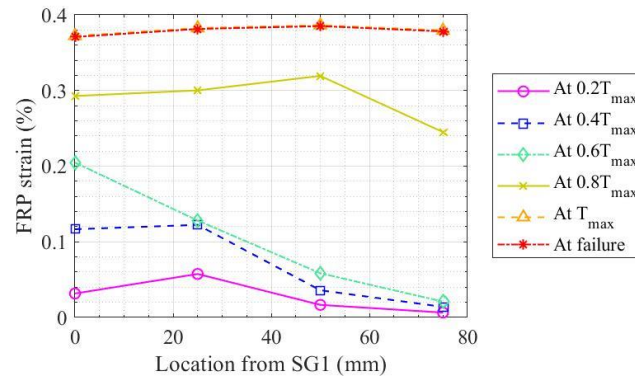


(c) JSI250-25

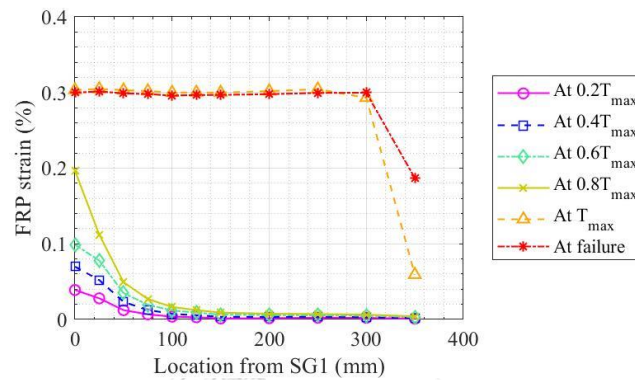


(d) JSI400-25

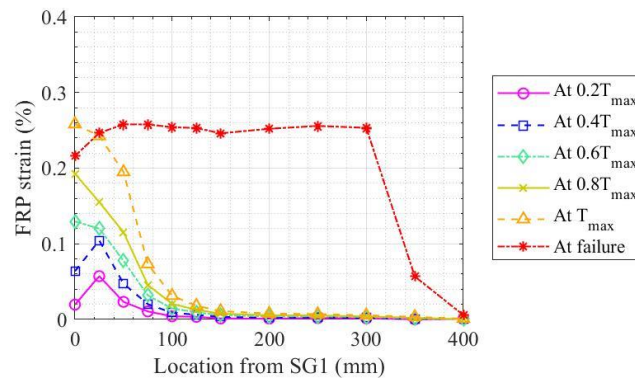
Figure 4.5 FRP strain distributions of joints with interfacial defect.



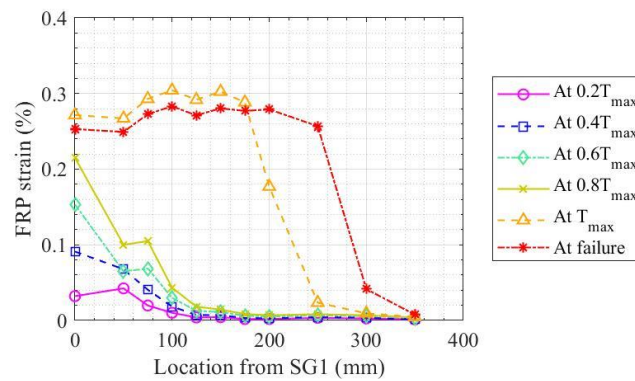
(a) JSU400-25



(b) JMU400-0



(c) JMU400-25



(d) JMU400-50

Figure 4.6 FRP strain distributions of joints without interfacial defect.

Location from SG1 equal to 25 mm is tip of initial bond defect for all joint specimens, except for joint JMU400-50. SG2 was affixed at tip of initial bond defect for all joint specimens with initial bond defect. SG5 to SG12 of joint JSU400-25 are not reported since strain gages were broken due to specimen transporting.

For most of joint specimens with initial bond defect, development of FRP strain at SG2 is not proportion to the increased applied tension. At 40% maximum applied tension, FRP strain value at SG2 of joint JSI150-25 and joint JSI400-25 have jumped about two times the corresponding values at 20% maximum applied tension. Small drop of such value were found at 60% maximum applied tension. These uncertainty values of SG2 may be caused by discontinuity of FRP strain among fully bonded FRP-steel interface region and bond defect region. Most of joint specimens with initial bond defect showed that FRP strain at SG2 were higher than strain at SG1 before 40% maximum applied tension was reached. A possible explanation for this is that axial stress concentration was occurred among fully bonded FRP-steel interface region and bond defect region. Moreover, these results indicate that FRP strain was insignificantly changed after SG5 onward. An effective bond length equal to 100 mm can be assumed.

FRP strain distribution at maximum applied tension and the corresponding trend at failure of joint JMU400-0 are not differed among the length of 300 mm measured from SG1. This may be driven by the uniform microscopic detachment of FRP plate from adhesive surface occurred in that region. Unlike FRP-steel joint with initial bond defect, the experimental observation found that the uniform microscopic detachment of FRP plate may be performed at failure. This may suggest that the presence of initial bond defect can potentially delay brittle failure due to FRP debonding.

4.3 Interfacial Fracture Toughness

FRP strain distribution data were converted to bond-slip relationship for the investigation of fracture toughness of FRP-steel joint specimens. Average fracture toughness values and their standard deviations are listed in Table 4.1. The fracture toughness increases as the FRP bond length increases. FRP strain data obtained from joint JSI75-25 could not calculate the average fracture toughness. It seems possible

that these results are due to the provided FRP bond length that less than 100 mm. The 100 mm FRP bond length was assumed to be the effective bond length for joint specimens conducted in this study, as presented in the previous section.

Table 4.1 Fracture toughness of joint specimens.

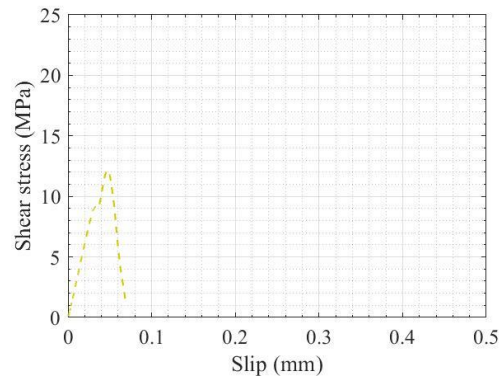
Joint	G_f (kJ/m^2)	
	Mean	S.D.
JSI75-25	*	
JSI150-25	1.38	0.47
JSI250-25	1.79	0.37
JSI400-25	1.96	0.37
JSU400-25	**	
JMU400-0	1.71	0.24
JMU400-25	1.42	0.64
JMU400-50	1.25	0.72

* Average value and standard deviation of specimen cannot calculate since the shear stress-slip curve for the region between SG1 and SG3 are neglected.

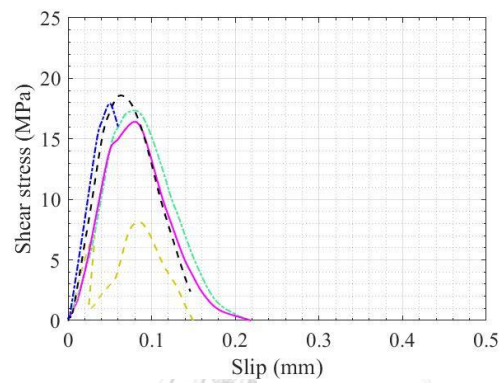
** Fracture toughness is not reported because the FRP strain data is not sufficient for a calculation of a fracture toughness.

According to the fracture toughness of joint specimens without interfacial defect, the fracture toughness decreases as the length of unbonded zone increases. Note that the average fracture toughness and their standard deviation of all considered shear stress-slip curves are equal to 1.60 and 0.54, respectively. The shear stress and slip relationships are plotted in Figure 4.7 and Figure 4.8.

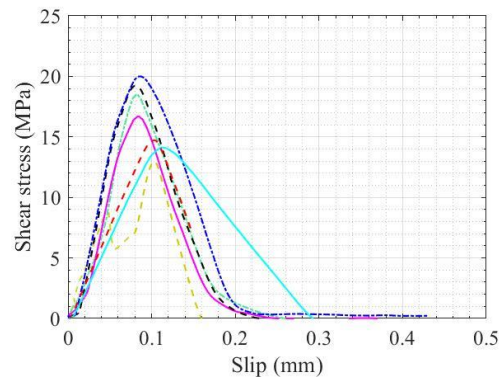
The shear stress-slip curves for the region between SG1 and SG2 were not plotted, as there is substantial variance of FRP strains in this region. The variance is most likely due to the existence of initial bond defect and axial stress concentration at tip of bond defect. Shear stress-slip curves fluctuated when considering the region between SG2 and SG3. Note that the average fracture toughness values and their standard deviations in Table 4.1 were calculated by excluding the shear stress-slip curve for the region between SG1 and SG3.



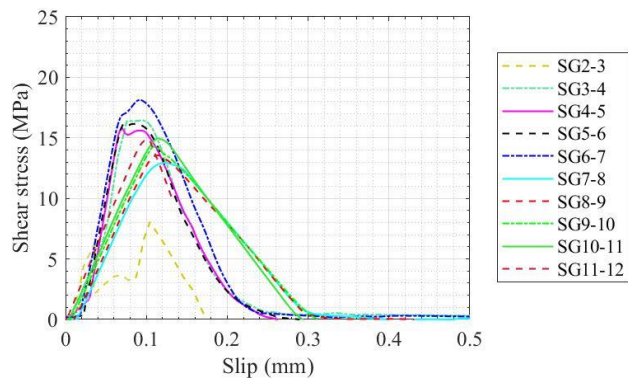
(a) JSI75-25



(b) JSI150-25

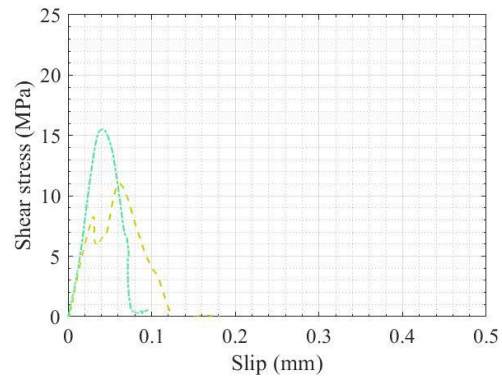


(c) JSI250-25

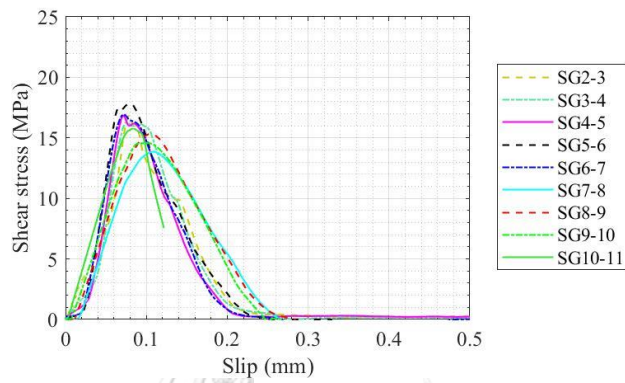


(d) JSI400-25

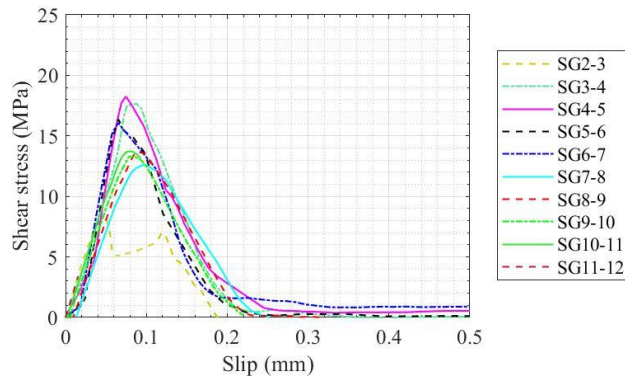
Figure 4.7 Bond-slip curve of joints with interfacial defect.



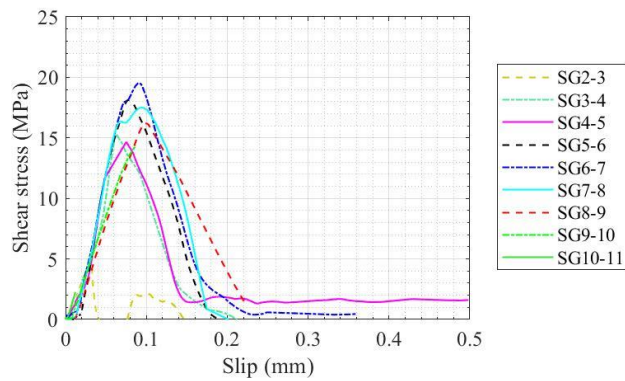
(a) JSU400-25



(b) JMU400-0



(c) JMU400-25



(d) JMU400-50

Figure 4.8 Bond-slip curve of joints without interfacial defect.

CHAPTER 5

FLEXURAL BEHAVIOR OF FRP-STRENGTHENED STEEL BEAMS

In the four-point flexural testing, the collected raw data consisted of strain gage signals, deflections, and applied load. Steel strains were paired with the corresponding applied load and used for the definition of yielding point as described in section 5.2. The midspan deflections were paired with the corresponding applied load to investigate flexural behavior in terms of load-deflection curves as explained in section 5.3. A cross-sectional strain distribution during the increasing of applied load was focused in section 5.4. Strain development along the FRP plate was examined in section 5.5. The FRP-strengthened steel beams under periodic unloading were diagnosed with additional considerations. Existing energies in beams were defined and discussed in section 5.6. The beam deflections near both sides of the FRP termination points were used to check the symmetry of an applied load as presented in Appendix A.1.

5.1 Failure of Beam Specimens

Visible damage of beams without FRP strengthening after testing is captured as shown in Figure 5.1. Permanent deflection could be easily observed. The photos captured when the compressive strain at top surface of the cover plate, measured by strain gage number 5 (SG5), is the approximately 855 microstrain. This strain level is equal to 55% yield strain of cover plate tested by coupons.

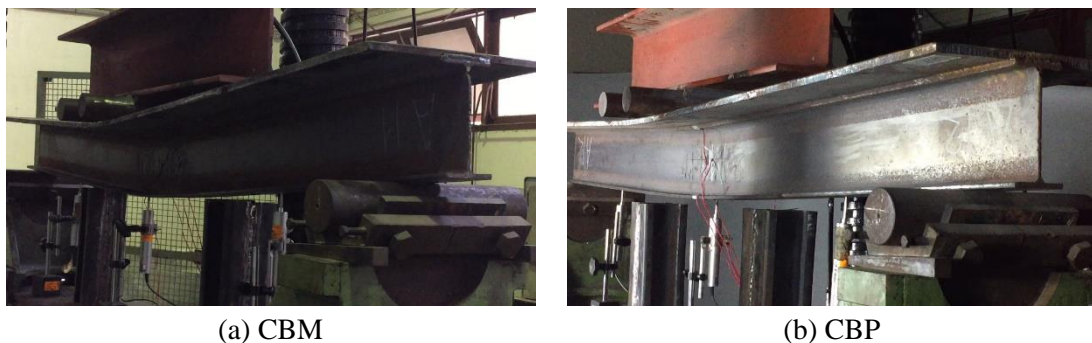


Figure 5.1 Unstrengthened beams after terminating the tests.

When an applied load reached the maximum value, strain at cover plate in most FRP-strengthened steel beams tested in this research is between 31-54% yield strain of cover plate tested by coupons. Beam BSP120-100 is the only one that the mentioned strain did not meet the range of 31-54% yield strain of cover plate tested by coupons (see section 5.4). At the maximum load, the compressive strain at top surface of cover plate of beam BSP120-100 is equal to 63% yield strain of cover plate tested by coupons. The beam BSP120-100 has higher debonding resistance than beam BMP120-100 (see further discussion in section 5.6).

Figure 5.2 shows that four displacement transducers were installed to measure the deflection at midspan and the points near the FRP termination points. Two transducers were affixed at the midspan. One of them was placed on the lower surface of bottom flange and the other one was located on the FRP plate surface. The midspan deflection was measured by the transducer placed on the lower surface of bottom flange.

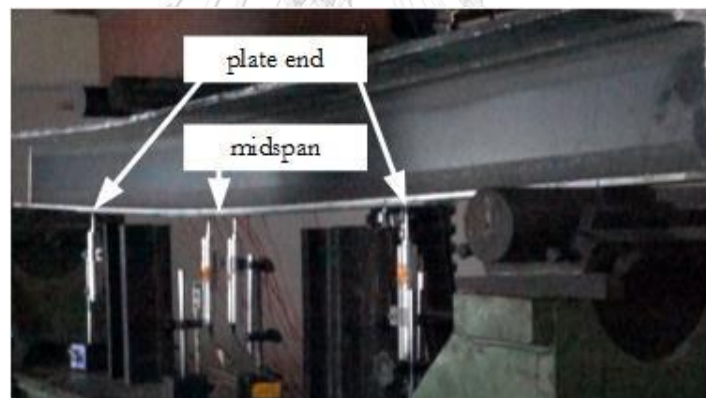


Figure 5.2 Beam specimens during testing.

A video camera-recording in slow-motion at 1,000 frames per second was used to capture the time when failure occurred in the FRP-strengthened steel beams. Beam BMM120-0 captured at failure was used to be the typical failure of fiber rupture as shown in Figure 5.3(a). Some broken carbon fiber pieces detached from the FRP plate are depicted in Figure 5.4(a). It was found experimentally that fiber rupture occurred before the initiation of FRP intermediate debonding. Photo of the beam BMM150-100 at failure was also used to be the typical failure of FRP intermediate debonding as shown in Figure 5.3(b).

In contrast to fiber rupture, in case of FRP intermediate debonding, there is no evidence that some broken carbon fiber pieces detached from the FRP plate. Some parts of FRP plate were also adhered at the lower surface of bottom flange as shown in Figure 5.4(b).

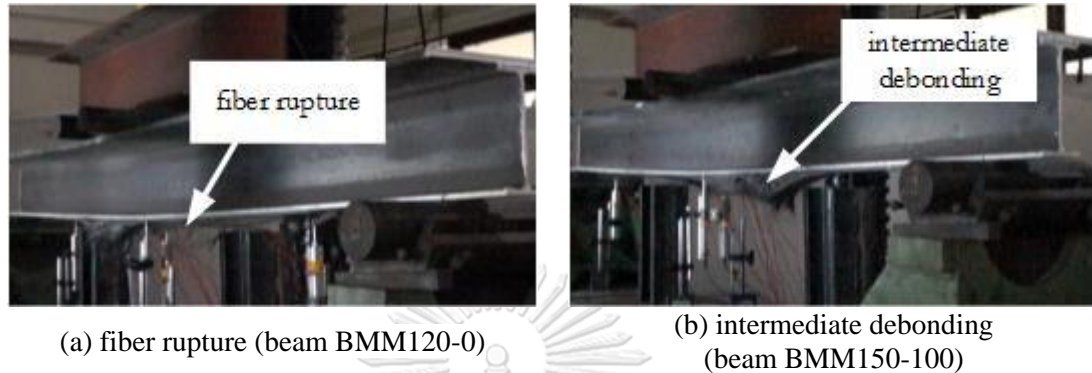


Figure 5.3 FRP-strengthened steel beams at the critical state of failure.

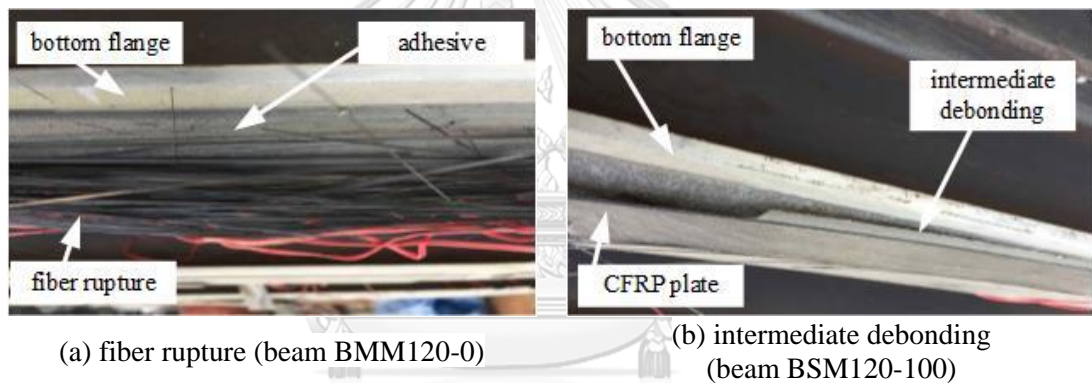


Figure 5.4 Typical failure modes of FRP-strengthened beams.

This seems to be that adhesion failure at steel-adhesive interface occurred in the beams failed by FRP intermediate debonding. According to the experiment observation, it could not be concluded that adhesion failure at the steel-adhesive interface occurred in all tested beams. Figure 5.5 is the photo captured from beam BMM150-100 when it failed. The mode of failure was mixed-mode. The detached adhesive revealed the adhesion failure at steel-adhesive interface. Some part of FRP plate was found to be debonded and this indicated the adhesion failure at FRP-adhesive interface.

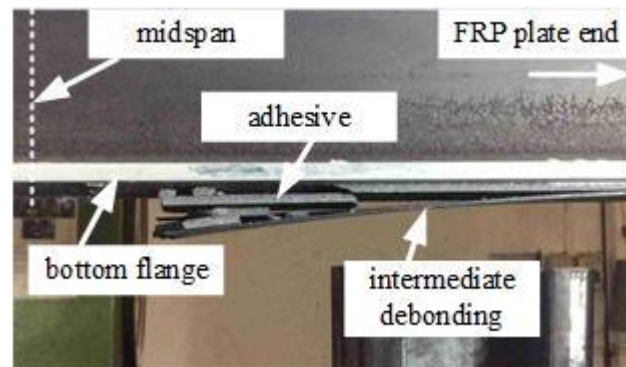


Figure 5.5 FRP intermediate debonding in beam BMM150-100

Single lap shear test proved that cohesion failure occurred under the provided surface preparation, adhesive thickness, and used FRP plates. Failure of FRP-strengthened steel beams using the thick adhesive may be easy to differentiate between adhesion failure and cohesion failure. This may be caused by bending effect and the use of thick adhesive, then the debonding propagation seems not to be controllable. In practice, the use of thick adhesive should be avoided in this time until the further research will find ways of controlling the path of FRP debonding propagation.

5.2 Definition of Yielding Point

Identification of yielding point of tested beams is the first step to split load-deflection curves into two regions, before yielding and after yielding. Definition of yielding point is presented in Appendix B.1. The loss of linearity of steel strain at midspan section is assigned as the yielding point.

5.3 Test Variables on Flexural Properties of FRP-Strengthened Steel Beams

The important characteristics of tested beams under bending test consist of yielding point, maximum load point, stiffness, ductility, and failure mode. This research considers such characteristics as flexural properties of the tested beams. Flexural properties of tested beams are summarized in Table 5.1. The symbol Δ_y and P_y are used to represent the midspan deflection (measured by DT2) and applied load at the yielding point. Stiffness is calculated from the ratio between P_y and Δ_y . When an applied load reached the maximum value, the symbols that used for the

corresponding midspan deflection and applied load are Δ_{max} and P_{max} , respectively. This research defines ductility index of beams using the ratio between Δ_{max} and Δ_y .

Table 5.1 Flexural properties of beams.

Beam	Δ_y (mm)	P_y (kN)	Stiffness (kN/m)	Δ_{max} (mm)	P_{max} (kN)	Δ_{max} / Δ_y	Failure mode*
CBM	4.95	98.3	19,865	17.76	129.5	3.59	BFY
CBMY	6.14	121.9	19,854	34.43	138.9	5.61	BFY
BMM120-0	4.37	94.9	21,691	14.64	163.1	3.35	FR
BMM120-50	3.77	85.6	22,720	18.75	191.0	4.98	ID
BMM120-100	4.16	80.8	19,449	17.39	163.9	4.18	ID
BMM120Y-100	5.24	120.5	22,985	24.51	198.7	4.68	ID
BMM150-100	4.55	98.5	21,655	16.39	182.5	3.60	ID
BSM120-0	4.51	89.5	19,846	23.60	182.1	5.23	FR
BSM120-100	3.97	79.3	19,957	33.52	200.3	8.44	ID
BSM120Y-100	5.88	124.6	21,189	28.92	198.2	4.92	ID
CBP	5.30	91.8	17,331	13.61	113.1	2.57	BFY
BMP120-100	4.65	99.9	21,482	17.88	191.6	3.85	ID
BSP120-100	4.13	86.6	20,958	26.03	182.1	6.30	ID

- * BFY ; Bottom flange yielding
 FR ; Fiber rupture
 ID ; Intermediate debonding

For the three unstrengthened beams, the criterion for test termination is the strain level at 55% yield strain of cover plate tested by coupons (855 microstrain) as described in section 5.1. Strains at both top and bottom surface of bottom flange were found to be yielded, then the failure mode of all unstrengthened beams is defined as bottom flange yielding. In fact, there was no sign of danger due to beam deformation and unstrengthened beams could keep testing. This research decided to terminate the test because of the consideration on inherently increases the safety of the measuring instruments. Note that this research implies the development of yielding state at bottom flange in terms of midspan deflection since displacement-controlled loading is used throughout the testing process.

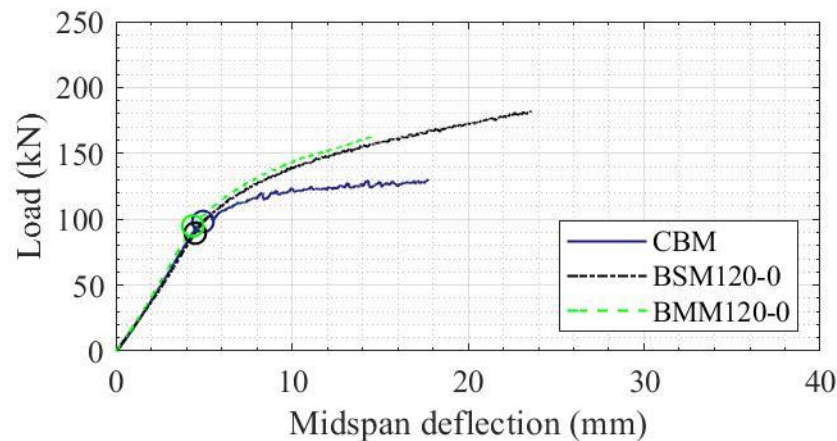
5.3.1 Effect of FRP Modulus

Load-midspan deflection curves of tested beams considering the effect of FRP strengthening and FRP modulus are plotted in Figure 5.6. Considering beam CBM, BMM120-0, and BSM120-0, it was found that FRP strengthening results in faster development of yielding state at bottom flange about 10-13% compared to beam CBM. Beam BSM120-0 was found that the development of yielding state was slower than beam BMM120-0 about 3%, which is different from the beams with initial bond defect. It was observed that the yielding point of beam BSM120-100 takes place before beam BMM120-100 about 5%. Effect of the use of different FRP moduli for strengthening the development of yielding state cannot be directly concluded. There is the possibility that the use of higher FRP modulus can accelerate the yielding state of FRP-strengthened beams without initial bond defect. This may result in opposite direction for FRP-strengthened beams with initial bond defect.

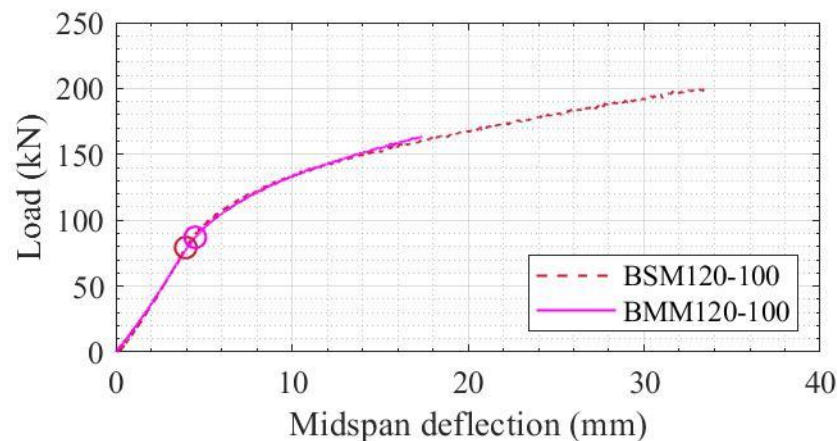
FRP strengthening did not affect the beam stiffness except for the beam BMM120-0 where stiffness was increased about 9% with respect to beam CBM. This may be caused by the difference of elastic modulus between steel beam and Sika® CarboDur® M514. Stiffness of beam BMM120-0 is also higher than beam BSM120-0 about 9%. Stiffness of beam BMM120-100 is reduced about 4% compared to the stiffness of beam BSM120-100. The presence of an initial bond defect may disturb the local stiffness of beam domain and results in slightly lower stiffness.

To take the strain level at 55% yield strain of cover plate tested by coupons as a basis, it was found that beam BMM120-0 and BSM120-0 cannot reach this point (see Table 5.5). Beam BMM120-0 and BSM120-0 can produce higher maximum applied load compared to beam CBM. Maximum load was increased about 26-41% after FRP strengthening. However, the increase in FRP modulus shows lower maximum load capacity about 10-18% compared to the beam strengthened by Sika® CarboDur® S512. A 18% decreasing of maximum load is found in case of FRP-strengthened beam with initial bond defect.

Deformation capability that beams permitted after the yielding point can be discussed in terms of ductility index. The use of FRP plate that has a similar elastic modulus compared to steel beam, as tested by beam BSM120-0, shows better ductility than beam BMM120-0. Ductility index of beam BSM120-0 is more than beam CBM about 46%, while the corresponding value of beam BMM120-0 is less than beam CBM about 7%. In view of the increase in FRP modulus, ductility is reduced about 36% for the beam without initial bond defect and 50% for the beam with initial bond defect. Consequently, these findings recommend the use of FRP plate that has a similar elastic modulus to steel beam.



(a) without initial bond defect



(b) with initial bond defect

Figure 5.6 Effect of FRP modulus on load-deflection curve.

The difference of flexural properties due to FRP strengthening and the increase in FRP modulus of tested beams under periodic unloading is shown in Figure 5.7. FRP strengthening can delay the development of yielding state

about 14-28% compared to beam CBP. Increase in stiffness of beams after FRP installation with respected to unstrengthened beam is about 21-24%. Maximum load of FRP-strengthened beams is produced about 61-69% compared to beam CBP. Ductilities of beams BSP120-100 and BMP120-100 with respected to beam CBP are increased about 150-245%. These results obviously showed that FRP strengthening can improve flexural properties under periodic unloading.

In case of the increase in FRP modulus, development of yielding state of beam BMP120-100 was slowed about 13% compared to beam BSP120-100. Stiffness of beam BMP120-100 was slightly increased about 3% with respected to beam BSP120-100. Maximum load capacity is improved at 5% compared to maximum load of beam BSP120-100 but ductility is decreased about 37%. These results are not exactly consistent with test results of beams under monotonic loading. In case of the beam without an initial bond defect and subjected to monotonic loading, only stiffness of beam BMM120-0 is increased when use higher FRP modulus. When an initial bond defect was created, only the development of yielding state of beam BMM120-100 is delayed. It is interested to note that all flexural properties may be improved for the real beams. The delay in development of yielding state requires to resolve for the faster activation of FRP contribution.

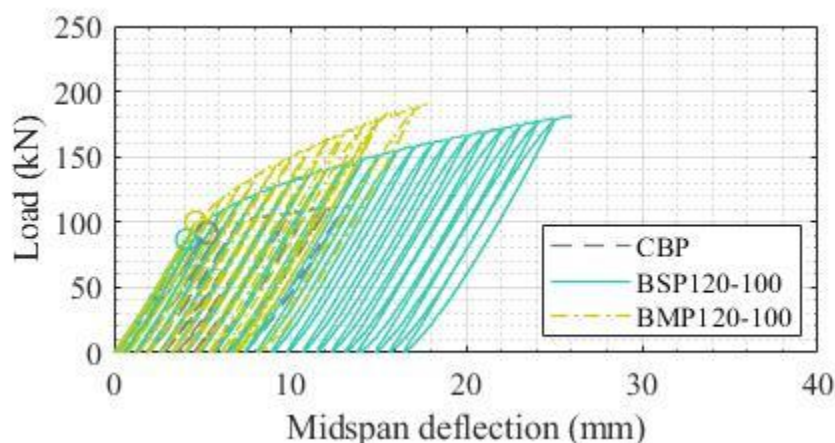


Figure 5.7 Effect of FRP modulus on load-deflection curve under periodic unloading condition.

5.3.2 Effect of Initial Bond Defect

The different effects among the presence and absence of initial bond defect in FRP-strengthened beams were found. Effect of initial bond defect on flexural properties of tested beams was shown by plotting load-deflection curves in Figure 5.8. Development of yielding state of beam BSM120-100 is faster about 12% compared to the beam BSM120-0. This phenomenon is also found in beam BMM120-50 that developed the yielding state faster than beam BMM120-0 about 14%. Lengthening of initial bond defect was provided in beam BMM120-100 and this beam developed the yielding state faster than beam BMM120-0 about 5%. Stiffness of most beams after creating an initial bond defect is not significantly changed except for beam BMM120-100 that reduces about 10% compared to the corresponding value of beam BMM120-0.

Maximum load capacity of FRP-strengthened beams with initial bond defect improves up to 17% compared to the beams without the creation of bond defect. Ductility index of beams increases about 25-61% with respected to the beams without initial bond defect. It was found that ductility index of beam BSM120-100 is the most improved compared to beam BMM120-50 and BMM120-100. These suggest that the presence of initial bond defect can improve strength and ductility index of FRP-strengthened beams. Future consideration should recommend an appropriated bond defect length and examine the effect of various bond defect length on the development of yielding state, strength, and ductility index of FRP-strengthened beams.

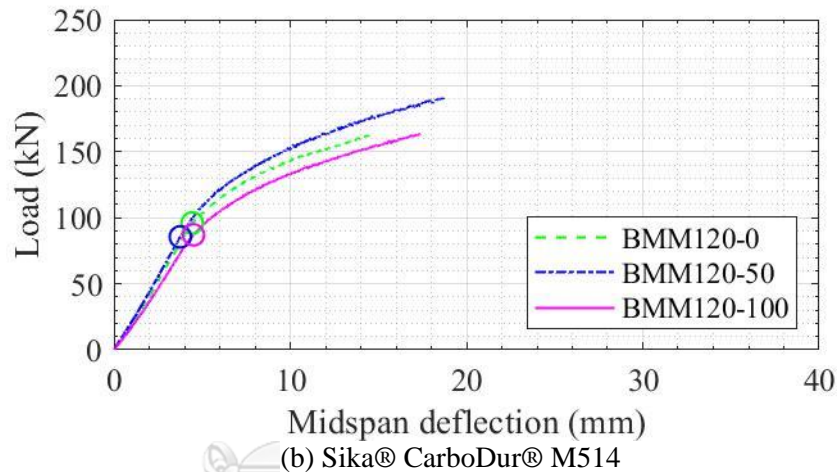
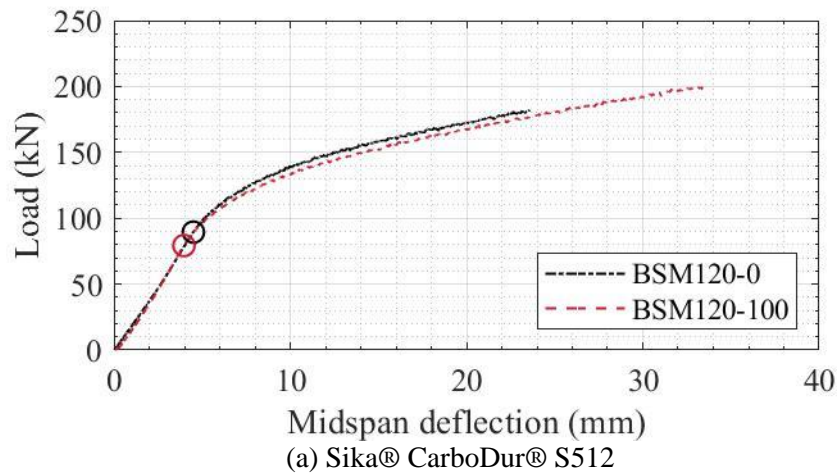


Figure 5.8 Effect of initial bond defect on load-deflection curve.

5.3.3 Effect of FRP Bond Length วิทยาลัย

Comparison of load-deflection curves between beam BMM120-100 and BMM150-100 is shown in Figure 5.9. It was found that the increase of FRP bond length retards the development of yielding state about 9%. Both stiffness and maximum load capacity of beam BMM150-100 improved about 12% compared to beam BMM120-100. The ductility index of beam BMM150-100 is decreased about 14% with respected to beam BMM120-100. The need of more strength with less ductility is still a challenging issue for designer to choose wisely.

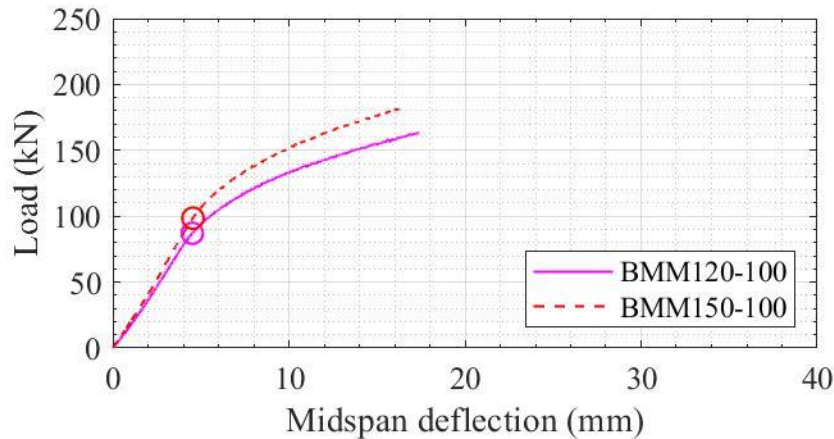


Figure 5.9 Effect of FRP bond length on load-deflection curve.

5.3.4 Effect of Predamage

Effect of predamage on flexural properties of FRP-strengthened beams is indicated in Figure 5.10. Beam CBMY was the retest of beam CBM. At the state of maximum load, the strain at top surface of bottom flange of beam CBM was 9.13 times yield strain of cover plate tested by coupons. Beam BSM120Y-100 was prepared from the pilot beam BMM120-200 (the beam using Sika® CarboDur® M514 and creating 200 mm bond defect). The last value of strain at top surface of bottom flange of the pilot beam BMM120-200 was 6.38 times yield strain of cover plate tested by coupons. Beam BMM120Y-100 was prepared from the pilot beam BMM120-100 (the beam using Sika® CarboDur® M514 and creating 100 mm bond defect). Note that the pilot beam BMM120-100 is not the same beam as beam BMM120-100. The last value of strain at top surface of bottom flange of the pilot beam BMM120-200 was 8.57 times yield strain of cover plate tested by coupons. All test results of the pilot beam BMM120-100 and the pilot beam BMM120-200 are not presented in this research because the purpose of conducting these two beams is only for pilot study.

Beams before and after applying predamage are compared to investigate the effect of predamage level on flexural properties of beams. It is found that predamage can delay the development of yielding state about 24-48% compared to yielding point of beams without predamage. Smallest

predamage (beam BSM120Y-100) retards the development of yielding state about 48% with respect to beam BSM120-100. Largest predamage (beam CBMY) defers the development of yielding state about 24% compared to yielding point of beam CBM. These could be preliminarily concluded that higher predamage level may have delayed the development of yielding state at top surface of bottom flange.

Stiffness of unstrengthened beams before and after applying predamage is not significantly changed. For tested beams with FRP strengthening, beam BSM120Y-100 is found that its stiffness was higher than beam BSM120-100 about 6%. Stiffness of beam BMM120Y-100 is more than beam BMM120-100 about 18%. This may imply that higher level of predamage and the use of higher FRP modulus can produce higher stiffness.

In view of maximum applied load, beam BSM120Y-100 provided insignificantly different maximum load (lower about 1%) compared to beam BSM120-100. Unlike the results found in beam BMM120Y-100, the maximum load was increased about 21% compared to beam BMM120-100. The trend showed that higher level of predamage and the use of higher FRP modulus can provide larger value of maximum load capacity.

Ductility index of beams before and after applying predamage showed the trend in a quite straightforward way with the trend of maximum applied load. Beam BSM120Y-100 is found that its ductility was decreased about 42% compared to the corresponding value of beam BSM120-100. The trend is in a different way for the beam BMM120Y-100. Ductility index of beam BMM120Y-100 was higher than ductility index of beam BMM120-100 about 11%. This may imply that higher level of predamage and the use of higher FRP modulus can provide better ductility. It is recommended that further research should be undertaken to focus the effect of predamage level on flexural properties of FRP-strengthened beams.

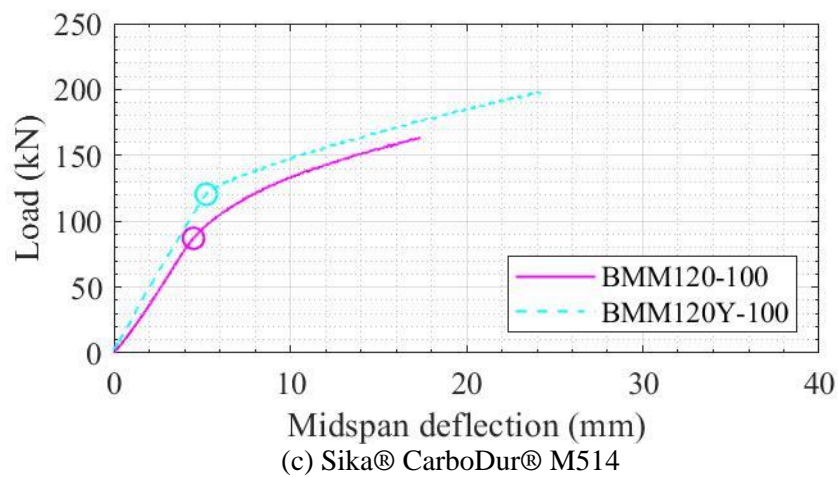
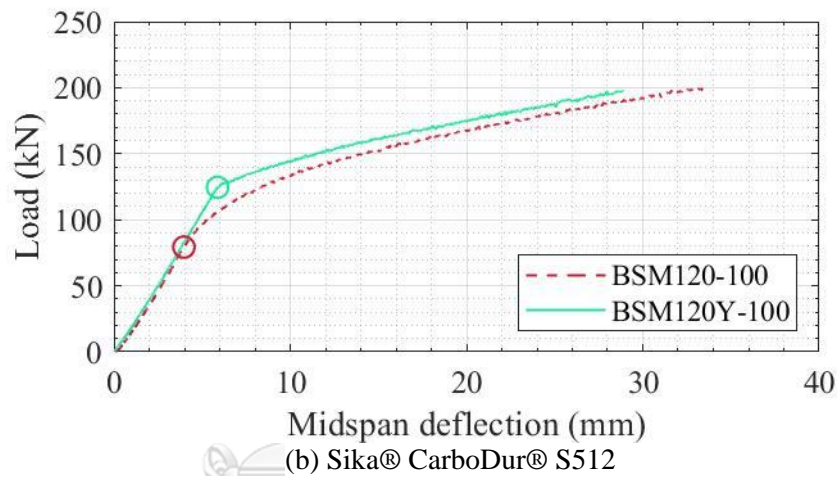
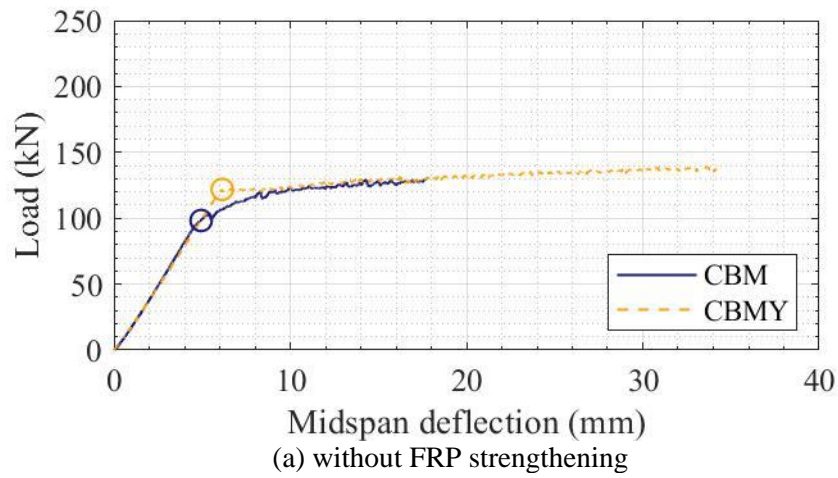


Figure 5.10 Effect of predamage on load-deflection curve.

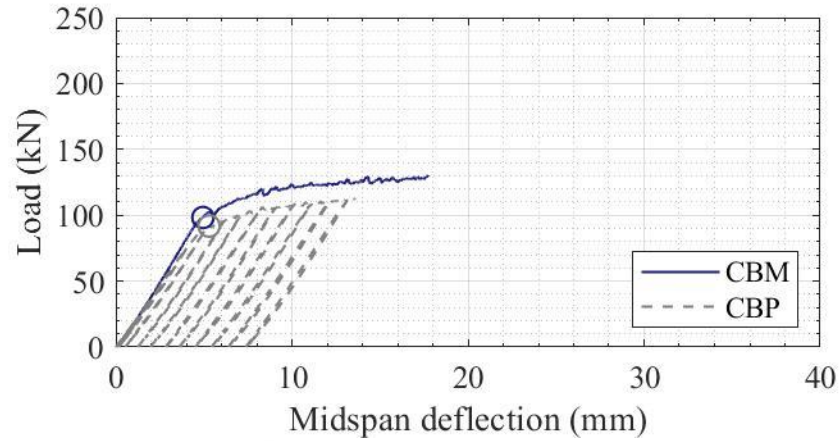
5.3.5 Effect of Periodic Unloading

Load-deflection curves of FRP-strengthened beams tested under monotonic and periodic unloading are compared in Figure 5.11. This worth noting that load-deflection curves of most beam tested under monotonic loading can be regard as the envelop line of the corresponding curves obtained from periodic unloading test. There is only beam BMM120-100 that cannot regard its load-deflection curve as the envelop line of beam BMP120-100. The possibility of this unconventional trend may result from a great different of elastic modulus between steel and Sika® CarboDur® M514. This may lead the load-deflection curve of beam BMM120-100 to the lower flexural capacity than expected trend as plotted by load-deflection curve of beam BMP120Y-100.

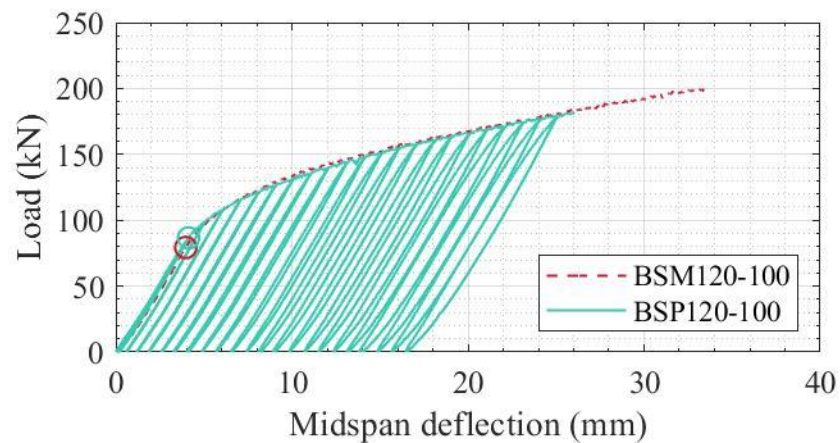
Periodic unloading condition can lead the beams to produce faster development of yielding state about 4-12%. Stiffness is reduced about 13% in case of unstrengthened beam. For beams strengthened with FRP, stiffness is increased about 5-10%. To take the strain level at 55% yield strain of cover plate tested by coupons as a basis, it was found that the applied load of beam CBP is reduced about 13% compared to beam CBM. Beam BSP120-100 produced the maximum load less than beam BSM120-100 about 9%. This decreased of measured load may cause by repeated load application from periodic unloading. Beam BMP120-100 is only one that can produce the maximum load about 17% more than beam BMM120-100. The possibility of this outcome may result from the use of higher FRP modulus that provides suitable condition for the increasing load capacity.

All tested beams under periodic unloading showed the decreasing of ductility about 8-28% with respected to the corresponding tested under monotonic loading. In practical design, these observation probabilities imply the difference between actual responses and predicted responses. For real structural beams, monotonic loading application is not controllable. Actual yielding state, maximum load, and ductility may not consistent with the case that beams subjected to the monotonic loading. Effect of periodic unloading

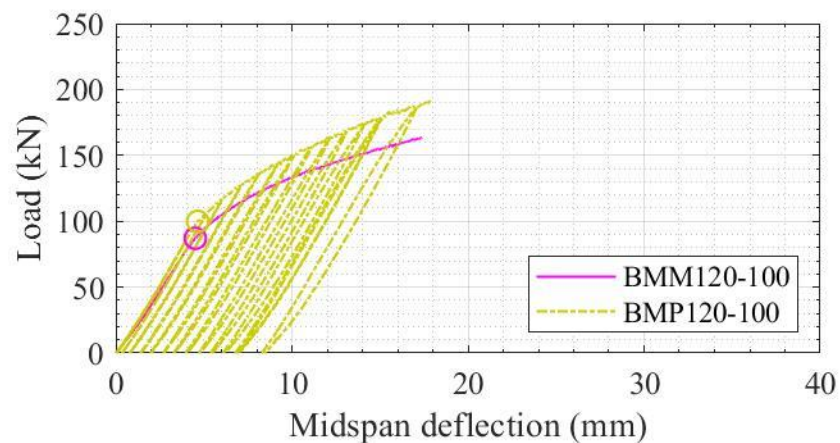
on flexural properties in more detailed should be conducted in further research.



(a) without FRP strengthening



(b) Sika® CarboDur® S512



(c) Sika® CarboDur® M514

Figure 5.11 Effect of periodic unloading on load-deflection curve.

5.4 Strain Distribution at Midspan Section

At the yielding point, steel strains normalized by coupon yield strain at midspan section of unstrengthened beams are presented in Table 5.2. Data shows fluctuated strains at bottom surface of the bottom flange of beam CBP. Strain at top surface of the cover plate of beam CBM and CBMY are quite variant. These results proved that strain compatibility over the cross section may not occurred for all situations. Effects of welding process and material integrity on strain compatibility should be made in future implementation.

Effect of predamage on steel strains at midspan section can be discussed by comparing the strain produced in beam CBM with the corresponding strains developed in beam CBMY. It was observed that tensile strain at bottom flange and midweb in beam CBMY are higher than the corresponding values for beam CBM. The compressive strains at top flange and cover plate of beam CBMY are also more than the values of beam CBM. It may be noted that predamage can bring an earlier yielding state in beams.

Monotonic loading and periodic unloading show different behavior on steel strains at midspan section. This issue was investigated by comparing the steel strains between beam CBM and beam CBP. There is a higher possibility that beam CBP store permanent deformation more than beam CBM. Steel strain at top surface of the bottom flange and midweb of beam CBP are higher than beam CBM.

Table 5.2 Steel strains of unstrengthened beams at yielding point.

Beam	Steel strain normalized by coupon yield strain				
	Bottom surface of the bottom flange	Top surface of the bottom flange	Midweb	Bottom surface of the top flange	Top surface of the cover plate
CBM	0.79	0.76	0.31	-0.12	-0.09
CBMY	1.10	1.04	0.38	-0.16	-0.15
CBP	0.55	0.80	0.43	-0.11	-0.15

For the FRP-strengthened beams subjected to yielding load, steel strains along the cross section at midspan are tabulated in Table 5.3. Strain at top surface of the bottom flange shows a lower value when performing FRP strengthening. This issue was observed by comparing the strain at top surface of the bottom flange between

beam CBM, beam BMM120-0, and beam BSM120-0. Predamage is also showed the decrease of such strain by considering on beam CBMY, beam BMM120Y-100, and beam BSM120Y-100. Periodic unloading condition is also consistent with that observation, which can be considered from beam CBP, beam BMP120-100, and beam BSP120-100.

Table 5.3 Steel strains of FRP-strengthened beams at yielding point.

Beam	Steel strain normalized by coupon yield strain			
	Top surface of the bottom flange	Midweb	Bottom surface of the top flange	Top surface of the cover plate
BMM120-0	0.71	0.27	-0.15	-0.12
BMM120-50	0.64	0.25	-0.11	-0.09
BMM120-100	0.66	0.24	-0.12	-0.07
BMM120Y-100	0.88	0.39	-0.19	-0.11
BMM150-100	0.76	0.29	-0.17	-0.10
BMP120-100	0.73	0.31	-0.15	-0.05
BSM120-0	0.68	0.27	-0.12	-0.06
BSM120-100	0.64	0.25	-0.13	-0.07
BSM120Y-100	0.96	0.42	-0.18	-0.16
BSP120-100	0.73	0.30	-0.13	-0.09

It is found that the presence of initial bond defect can decrease the strain at top surface of the bottom flange. The use of higher FRP modulus decrease the strain at top surface of the bottom flange except for beams tested under periodic unloading condition. Increasing FRP bond length is only possibility that can produce higher strain at top surface of the bottom flange.

When an applied load reached the maximum value, steel strain over the midspan section of unstrengthened beams are tabulated in Table 5.4. Strain at top surface of the cover plate is limited to 0.55 times yield strain of cover plate coupons. This value is selected since most of FRP-strengthened steel beams subjected to their maximum applied load produce the corresponding strain less than such value. Fluctuated strain at bottom surface of the bottom flange of beam CBP is observed as same as the yielding point. Strain at bottom surface of the bottom flange of beam CBMY is also variant.

Table 5.4 Steel strains of unstrengthened beams at maximum load.

Beam	Steel strain normalized by coupon yield strain				
	Bottom surface of the bottom flange	Top surface of the bottom flange	Midweb	Bottom surface of the top flange	Top surface of the cover plate
CBM	9.39	8.18	5.86	0.40	-0.55
CBMY	10.88	11.31	4.59	0.28	-0.55
CBP	5.73	7.37	6.67	0.12	-0.55

When an applied load reached the maximum value, steel strains at midspan section were detected and presented in Table 5.5. These found that most beams produced strain at top surface of the cover plate less than 55% yield strain of cover plate tested by coupons. Only beam BSP120-100 can produce the strain level at 63% yield strain of cover plate tested by coupons. The use of Sika® CarboDur® S512 in beams with initial bond defect tends to produce higher compressive strain at the cover plate compared to the other beams. This may be caused by using FRP plate that has elastic modulus close to steel beam and the presence of initial bond defect. These two issues may allow beams to become more deformable compared to the other beams.

Tensile strain at top surface of the bottom flange is found to be larger when beams created an initial bond defect. This strain would decrease in case of the shortening of FRP bond length and predamage application. Periodic unloading caused lower such strain value for beam strengthened with Sika® CarboDur® M514 but the opposite way is observed in beam strengthened with Sika® CarboDur® S512. The great difference of elastic modulus between steel and FRP may reduce tensile strain at top surface of the bottom flange.

For the beam BMM120-0 and BSM120-0, strain at midweb is lower than strain at top surface of the bottom flange. The possibility of this issue is that bottom flange may be restrained by FRP plate, then its strain might not be freely deformed as midweb. BMM120Y-100 is the beam that can detect this issue. The level of predamage in beam BMM120Y-100 may produce the certain value of initial curvature and this state may suitable for the restraint of bottom flange by FRP plate. The issue found in beam BMM120Y-100 should be verified and studied in detail for the further consideration.

Table 5.5 Steel strains of FRP-strengthened beams at maximum load.

Beam	Steel strain normalized by coupon yield strain			
	Top surface of the bottom flange	Midweb	Bottom surface of the top flange	Top surface of the cover plate
BMM120-0	0.73	1.15	-0.10	-0.53
BMM120-50	8.56	1.30	0.05	-0.47
BMM120-100	11.65	3.80	-0.02	-0.33
BMM120Y-100	1.49	2.16	-0.18	-0.46
BMM150-100	6.83	1.11	-0.10	-0.40
BMP120-100	8.12	1.24	-0.04	-0.31
BSM120-0	3.07	3.55	0.09	-0.49
BSM120-100	10.83	2.36	0.01	-0.54
BSM120Y-100	3.49	1.12	0.12	-0.54
BSP120-100	10.91	1.12	0.04	-0.63

Additional details of strain distribution at midspan section are shown in APPENDIX B. Strain distribution of all beams before an applied load reached the yielding point is plotted in section B.2. After the beam beyond the yielding load, strain distribution is changed and behave as depicted in section B.3. Moreover, steel strain of FRP-strengthened beams in vicinity of midspan section before and after the yielding point is investigated in section B.4 and B.5, respectively.

5.5 Strain Distribution Along FRP Plates

Most beams are found that the development of FRP strain is proportioned to the applied load before the yielding state. Constant moment region cannot produce an identical strain level. This may cause from non-uniform of plastic zone propagation, and any real beams subjected to fluctuated and changeable applied load might also found this issue. Local fiber rupture and FRP intermediate debonding are found when the applied load reached the maximum value. When the applied beyond the maximum value, it was found that some point of FRP plate changed from to fiber rupture to intermediate debonding. Local fiber rupture and intermediate debonding after beams beyond the maximum applied load can be recorded by using a 100 Hz sampling rate and discussed in APPENDIX C.

The development of strain distribution along FRP plates in more details are plotted in APPENDIX B. Before an applied load reached the yielding state, FRP strains are distributed as depicted in section B.6., FRP strains are distributed as plotted in section B.7 after the beam beyond the yielding load.

5.6 Beam Tested under Periodic Unloading

One of the advantage for the load application in periodic unloading pattern is that existing energies in beams and stiffness deterioration during testing can be observed. This loading condition may conduct to examine more realistic of flexural properties of tested beams since the real structural components are not subjected to monotonic loading.

Load-deflection curves of beams tested under periodic unloading are found that there are many cycles of load application as depicted in Figure 5.12(a). Some of load cycle is considered and shaded for the better understanding. This cycle contains loading path and unloading path. When any beam released from the applied load, unloading stiffness can be recorded.

According to the considered cycle, there are two energies existed in beam as shown in Figure 5.12(b). Dissipated energy is known as non-recoverable energy. This energy dissipates from the structural domain and lead to the increase of internal strain energy that can deform the structural domain. Recoverable energy reveals the capability of structural domain that can resist the tremendously increasing in dissipated energy. After the yielding state of structural domains, there is the possibility that dissipated energy can overcome the recoverable energy.

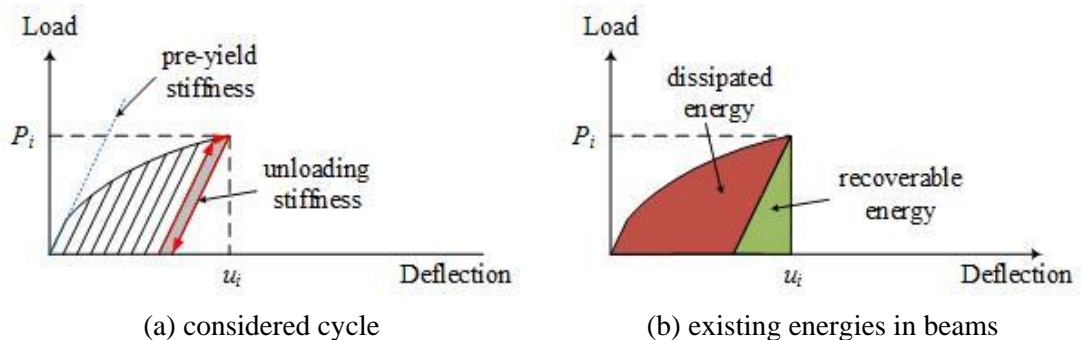


Figure 5.12 Definition of energies in beams tested under periodic unloading.

Existing energies in three beams tested under periodic unloading are calculated and plotted in Figure 5.13 to Figure 5.15. The yielding state of beam CBP, BSP120-100, and BMP120-100 is firstly produced at the first time the beams reached the midspan deflection about 5.30, 4.13, and 4.65, respectively. The value of midspan deflection that dissipated energy can overcome the recoverable energy is started at 8, 9, and 10, respectively. This may imply that dissipated energy can overcome the recoverable energy when the midspan deflection beyond the yielding state up to 51%.

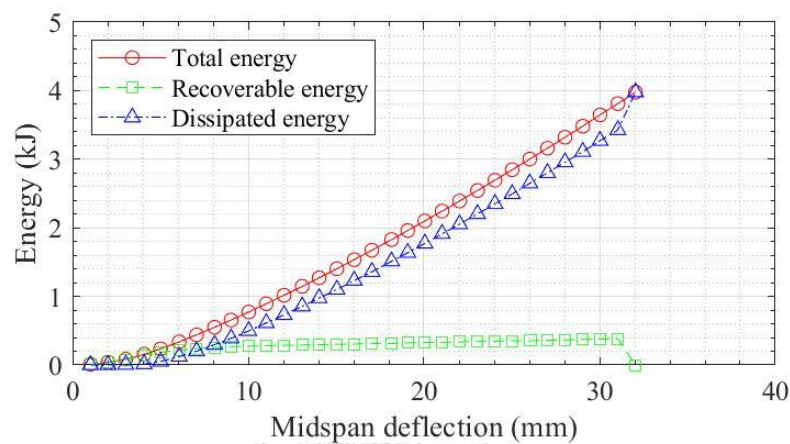


Figure 5.13 Development of energies in beam CBP.

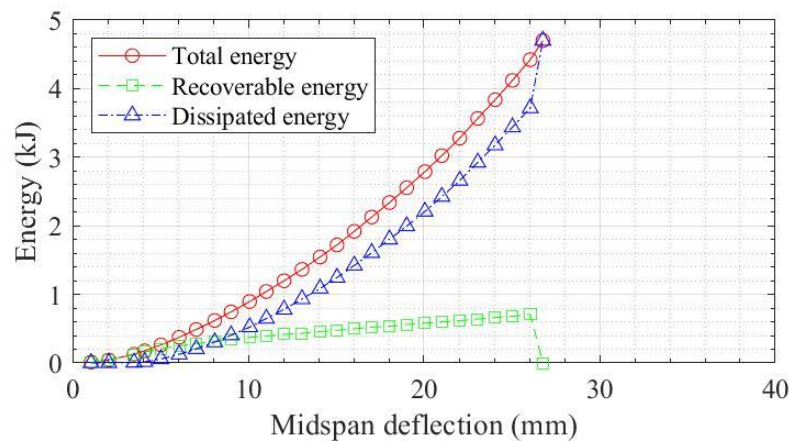


Figure 5.14 Development of energies in beam BSP120-100.

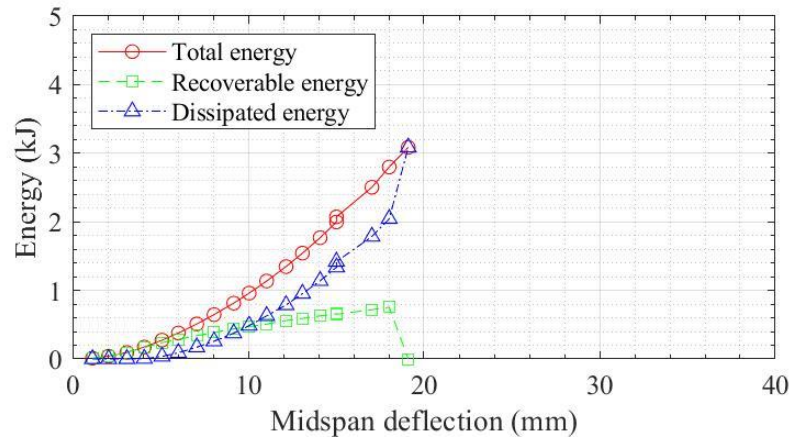


Figure 5.15 Development of energies in beam BMP120-100.

The unloading stiffness with respect to initial stiffness is examined to detect the stiffness deterioration throughout the testing. Figure 5.16 plotted the ratio between unloading stiffness and initial stiffness versus the midspan deflection. It is found that the yielding state is not affected to such ratio. The state that dissipated energy can overcome the recoverable energy is also not affected to the ratio between unloading stiffness and initial stiffness. It is worth noting that the average ratio is about 1.06. This may lead to the prediction of unloading stiffness of beams under non-monotonic loading for the future consideration.

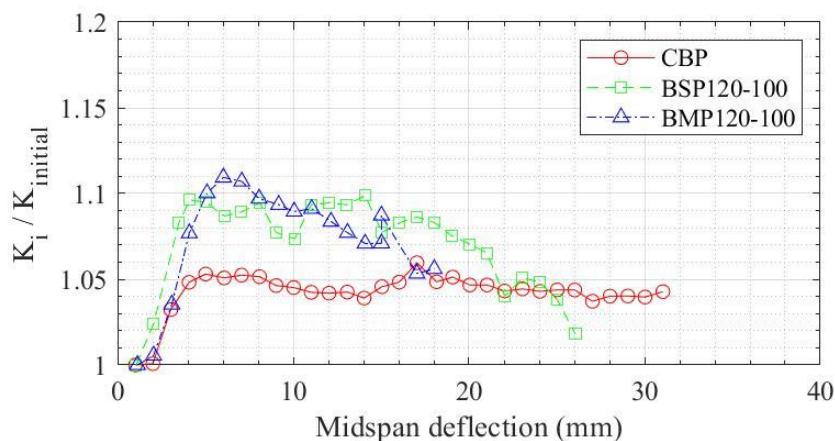


Figure 5.16 Ratio between unloading stiffness and initial stiffness.

The difference of recoverable energy between FRP-strengthened beams and beam CBP is determined and also plotted versus the midspan deflection as shown in Figure 5.17. It is interested to note that this difference of energy may involve interaction with fracture toughness. This research defined this energy as debonding resistance energy. The difference of capability for recovery before and after FRP strengthening treated as the capability for resistance of FRP debonding. However, this approach should be examined and verified in further works.

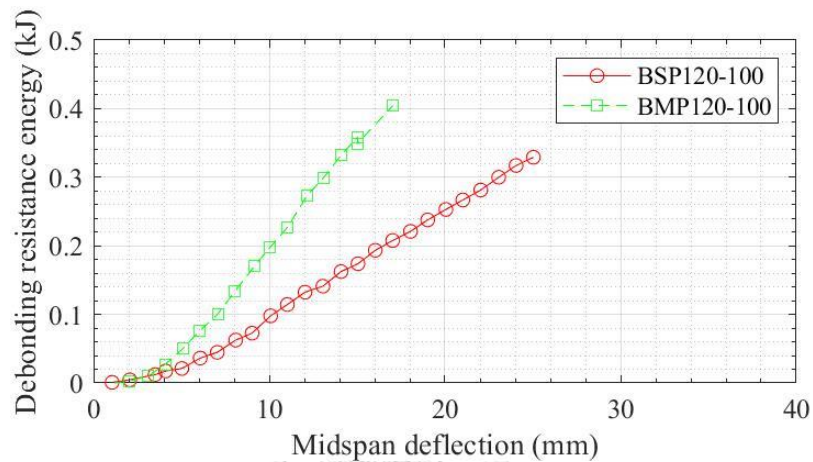


Figure 5.17 Difference between recoverable energies before and after FRP strengthening.

CHAPTER 6

CONCLUSIONS

6.1 Conclusions

There are two main objectives in this research. The FRP-steel joint specimens were tested to examine their bond behavior and fracture toughness. The testing of FRP-strengthened steel beams subjected to four-point flexural loading was conducted to investigate their flexural behavior. A synopsis of this research can be divided into two sections as follows.

6.1.1 Bond Behavior of FRP-Steel Joints

A visual inspection suggested that FRP-steel joints with an initial bond defect failed by FRP intermediate debonding. The FRP delamination area decreases as the FRP bond length increases. The presence of interfacial bond defect in joint specimens tends to reduce an area of FRP delamination compared to the presence of FRP unbonded zone in joint specimens.

The measured strain distributions of FRP-steel joints exhibited that the presence of initial bond defect can delay the brittle failure due to FRP debonding. The bond-slip curves of FRP-steel joints indicated that the fracture toughness decreases as the initial bond defect length increases. The reduction of FRP bond length decreased the fracture toughness.

6.1.2 Flexural Behavior of FRP-Strengthened Steel Beams

A fiber rupture failure was found in the FRP-strengthened steel beams without an initial bond defect. Unlike the FRP-strengthened steel beams with initial bond defect, the intermediate debonding failure occurred instead of fiber rupture.

For the FRP strengthening of steel beams, the use of higher FRP modulus considerably reduces the maximum load capacity and ductility index of beams. It is surprising that the existence of initial bond defect can improve both maximum load and ductility index of the FRP-strengthened steel beams.

The increase of FRP bond length can enhance both stiffness and maximum load of beams. The ductility index of beams decreases as the FRP bond length increases.

The situations consist of predamaged beams and beams subjected to periodic unloading were also investigated. According to FRP-strengthened steel beams with predamage, it seems that the use of high FRP modulus and high level of predamage tends to produce higher maximum load capacity. For the beams tested under periodic unloading, both maximum load and ductility are considerably lower compared to the identical beams subjected to monotonic loading.

6.2 Recommendations for Future Works

According to experimental observation, the path of FRP debonding propagation is uncontrollable. A combination between adhesion failure and cohesion failure is found in many tested beams. Effects of adhesive thickness and different surface preparation on the failure surface of FRP-strengthened steel beams with initial bond defect are suggested for further works.

It is found that the beam with 50 mm of defect length provided better strength and ductility than the beam with 100 mm of defect length. An appropriated length of initial bond defect for the best performance in flexural behavior should be verified.

Before the tested beams reached the yielding load, the measured cover plate strain showed lower value compared to the measured strain at top flange. The unusual strain signal is also found before the tested beams failed. The strain at web is higher than the strain at bottom flange. Nonlinear strain compatibility in actual beams due to welding process should be focused for an improvement of further models.

The tested beams under periodic unloading exhibited a sign of stiffness deterioration while unloading the tested beams. These issues should be investigated by conducting an additional testing. The future numerical model should be expanded for the prediction of FRP-strengthened steel beams subjected to seismic loading.

REFERENCES

- [1] A. Carolin, "Carbon fibre reinforced polymers for strengthening of structural elements," PhD Thesis, Department of Civil and Mining Engineering, Lulea University of Technology, Sweden, 2003.
- [2] A. M. I. Sweedan, M. M. A. Alhadid, and K. M. El-Sawy, "Experimental study of the flexural response of steel beams strengthened with anchored hybrid composites," *Thin-Walled Structures*, vol. 99, pp. 1-11, 2016/02/01/ 2016, doi: <https://doi.org/10.1016/j.tws.2015.10.026>.
- [3] N. D. Hai and H. Mutsuyoshi, "Structural behavior of double-lap joints of steel splice plates bolted/bonded to pultruded hybrid CFRP/GFRP laminates," *Construction and Building Materials*, vol. 30, pp. 347-359, 2012/05/01/ 2012, doi: <https://doi.org/10.1016/j.conbuildmat.2011.12.001>.
- [4] J. G. Teng, D. Fernando, and T. Yu, "Finite element modelling of debonding failures in steel beams flexurally strengthened with CFRP laminates," *Engineering Structures*, vol. 86, pp. 213-224, 2015/03/01/ 2015, doi: <https://doi.org/10.1016/j.engstruct.2015.01.003>.
- [5] A. Lenwari, T. Thepchatri, and P. Albrecht, "Flexural Response of Steel Beams Strengthened with Partial-Length CFRP Plates," *Journal of Composites for Construction*, vol. 9, no. 4, pp. 296-303, 2005/08/01 2005, doi: [https://10.1061/\(ASCE\)1090-0268\(2005\)9:4\(296\)](https://10.1061/(ASCE)1090-0268(2005)9:4(296)).
- [6] C. Miller Trent, J. Chajes Michael, R. Mertz Dennis, and N. Hastings Jason, "Strengthening of a Steel Bridge Girder Using CFRP Plates," *Journal of Bridge Engineering*, vol. 6, no. 6, pp. 514-522, 2001/12/01 2001, doi: [https://10.1061/\(ASCE\)1084-0702\(2001\)6:6\(514\)](https://10.1061/(ASCE)1084-0702(2001)6:6(514)).
- [7] J. R. Vinson and R. L. Sierakowski, *The behavior of structures*. Kluwer, Dordrecht, Netherlands,, 1987.
- [8] D. Schnerch, K. Stanford, E. A. Sumner, and S. Rizkalla, *Strengthening Steel Structures and Bridges with High-Modulus Carbon Fiber-Reinforced Polymers Resin Selection and Scaled Monopole Behavior*. 2004.
- [9] S. Fawzia, X.-L. Zhao, R. Al-Mahaidi, and S. Rizkalla, "Bond characteristics between CFRP and steel plates in double strap joints," *The International Journal of Advanced Steel Construction*, vol. 1, no. 2, pp. 17-27, 2005. [Online]. Available: <https://eprints.qut.edu.au/44538/>.
- [10] P. Colombi and C. Poggi, "Strengthening of tensile steel members and bolted joints using adhesively bonded CFRP plates," *Construction and Building Materials*, vol. 20, no. 1, pp. 22-33, 2006/02/01/ 2006, doi: <https://doi.org/10.1016/j.conbuildmat.2005.06.042>.
- [11] A. M. Albat and D. P. Romilly, "A direct linear-elastic analysis of double symmetric bonded joints and reinforcements," *Composites Science and Technology*, vol. 59, no. 7, pp. 1127-1137, 1999/05/01/ 1999, doi: [https://doi.org/10.1016/S0266-3538\(98\)00149-3](https://doi.org/10.1016/S0266-3538(98)00149-3).
- [12] S. Xia and J. G. Teng, *Behaviour of FRP-to-steel bonded joints*. 2005.
- [13] D. Fernando, "Bond behaviour and debonding failures in CFRP-strengthened steel members," PhD Thesis, Department of Civil and Structural Engineering, The Hong Kong Polytechnic University, Hong Kong, 2010.
- [14] T. Yu, D. Fernando, J. G. Teng, and X. L. Zhao, "Experimental study on CFRP-

- to-steel bonded interfaces," *Composites Part B: Engineering*, vol. 43, no. 5, pp. 2279-2289, 2012/07/01/ 2012, doi: <https://doi.org/10.1016/j.compositesb.2012.01.024>.
- [15] A. M. I. Sweedan, K. M. El-Sawy, and M. M. A. Alhadid, "Interfacial behavior of mechanically anchored FRP laminates for strengthening steel beams," *Journal of Constructional Steel Research*, vol. 80, pp. 332-345, 2013/01/01/ 2013, doi: <https://doi.org/10.1016/j.jcsr.2012.09.022>.
- [16] D. Fernando, T. Yu, and J. G. Teng, "Behavior of CFRP Laminates Bonded to a Steel Substrate Using a Ductile Adhesive," *Journal of Composites for Construction*, vol. 18, no. 2, p. 04013040, 2014/04/01 2014, doi: [https://doi.org/10.1061/\(ASCE\)CC.1943-5614.0000439](https://doi.org/10.1061/(ASCE)CC.1943-5614.0000439).
- [17] H. Yuan, J. G. Teng, R. Seracino, Z. S. Wu, and J. Yao, "Full-range behavior of FRP-to-concrete bonded joints," *Engineering Structures*, vol. 26, no. 5, pp. 553-565, 2004/04/01/ 2004, doi: <https://doi.org/10.1016/j.engstruct.2003.11.006>.
- [18] F. Ceroni, M. Ianniciello, and M. Pecce, "Bond behavior of FRP carbon plates externally bonded over steel and concrete elements: Experimental outcomes and numerical investigations," *Composites Part B: Engineering*, vol. 92, pp. 434-446, 2016/05/01/ 2016, doi: <https://doi.org/10.1016/j.compositesb.2016.02.033>.
- [19] M. Bocciarelli, P. Colombi, G. Fava, and C. Poggi, *Interaction of interface delamination and plasticity in tensile steel members reinforced by CFRP plates*. 2007, pp. 79-92.
- [20] J. L. Hart-Smith, "Adhesive-bonded double-lap joints," Technical Report, National Aeronautics and Space Administration, Langley Research Center, USA, 1973.
- [21] *CNR-DT 200 R1/2012: Guide for the Design and Construction of Externally Bonded FRP Systems for Strengthening Existing Structures*, 8880800744, Advisory Committee on Technical Recommendation for Construction of National Research Council, 2006.
- [22] H.-T. Wang, G. Wu, Y.-T. Dai, and X.-Y. He, "Determination of the bond-slip behavior of CFRP-to-steel bonded interfaces using digital image correlation," *Journal of Reinforced Plastics and Composites*, vol. 35, no. 18, pp. 1353-1367, 2016/09/01 2016, doi: <https://doi.org/10.1177/0731684416651342>.
- [23] H.-T. Wang, G. Wu, Y.-T. Dai, and X.-Y. He, "Experimental Study on Bond Behavior between CFRP Plates and Steel Substrates Using Digital Image Correlation," *Journal of Composites for Construction*, vol. 20, no. 6, p. 04016054, 2016/12/01 2016, doi: [https://doi.org/10.1061/\(ASCE\)CC.1943-5614.0000701](https://doi.org/10.1061/(ASCE)CC.1943-5614.0000701).
- [24] J. He and G. Xian, "Bond-slip behavior of fiber reinforced polymer strips-steel interface," *Construction and Building Materials*, vol. 155, pp. 250-258, 2017, doi: <http://dx.doi.org/10.1016/j.conbuildmat.2017.08.062>.
- [25] H. T. Wang and G. Wu, "Bond-slip models for CFRP plates externally bonded to steel substrates," *Composite Structures*, vol. 184, pp. 1204-1214, 2018, doi: <http://dx.doi.org/10.1016/j.compstruct.2017.10.033>.
- [26] Q. Q. Yu, X. L. Gu, X. L. Zhao, D. M. Zhang, H. W. Huang, and C. Jiang, "Characterization of model uncertainty of adhesively bonded CFRP-to-steel joints," *Composite Structures*, vol. 215, pp. 150-165, 2019, doi: <https://doi.org/10.1016/j.compstruct.2019.02.045>.

- [27] X.-L. Zhao and L. Zhang, "State-of-the-art review on FRP strengthened steel structures," *Engineering Structures*, vol. 29, no. 8, pp. 1808-1823, 2007/08/01/2007, doi: <https://doi.org/10.1016/j.engstruct.2006.10.006>.
- [28] J. Deng, M. M. K. Lee, and S. S. J. Moy, "Stress analysis of steel beams reinforced with a bonded CFRP plate," *Composite Structures*, vol. 65, no. 2, pp. 205-215, 2004/08/01/2004, doi: <https://doi.org/10.1016/j.compstruct.2003.10.017>.
- [29] K. Nozaka, K. Shield Carol, and F. Hajjar Jerome, "Effective Bond Length of Carbon-Fiber-Reinforced Polymer Strips Bonded to Fatigued Steel Bridge I-Girders," *Journal of Bridge Engineering*, vol. 10, no. 2, pp. 195-205, 2005/03/01/2005, doi: [https://doi.org/10.1061/\(ASCE\)1084-0702\(2005\)10:2\(195\)](https://doi.org/10.1061/(ASCE)1084-0702(2005)10:2(195)).
- [30] A. Lenwari, T. Thepchatri, and P. Albrecht, "Debonding Strength of Steel Beams Strengthened with CFRP Plates," *Journal of Composites for Construction*, vol. 10, no. 1, pp. 69-78, 2006/02/01/2006, doi: [https://doi.org/10.1061/\(ASCE\)1090-0268\(2006\)10:1\(69\)](https://doi.org/10.1061/(ASCE)1090-0268(2006)10:1(69)).
- [31] L. De Lorenzis and G. Zavarise, "Cohesive zone modeling of interfacial stresses in plated beams," *International Journal of Solids and Structures*, vol. 46, no. 24, pp. 4181-4191, 2009/12/01/2009, doi: <https://doi.org/10.1016/j.ijsolstr.2009.08.010>.
- [32] L. De Lorenzis, D. Fernando, and J.-G. Teng, "Coupled mixed-mode cohesive zone modeling of interfacial debonding in simply supported plated beams," *International Journal of Solids and Structures*, vol. 50, no. 14, pp. 2477-2494, 2013/07/01/2013, doi: <https://doi.org/10.1016/j.ijsolstr.2013.03.035>.
- [33] W. Jiang and P. Qiao, "An improved four-parameter model with consideration of Poisson's effect on stress analysis of adhesive joints," *Engineering Structures*, vol. 88, pp. 203-215, 2015/04/01/2015, doi: <https://doi.org/10.1016/j.engstruct.2015.01.027>.
- [34] K. Narmashiri, H. Sulong, and Z. Jumaat, "Flexural strengthening of steel I-beams by using CFRP strips," *International journal of physical sciences*, vol. 6, no. 7, pp. 1620-1627, 2011, doi: <https://doi.org/10.5897/IJPS11.140>.
- [35] J. Deng and M. M. K. Lee, "Behaviour under static loading of metallic beams reinforced with a bonded CFRP plate," *Composite Structures*, vol. 78, no. 2, pp. 232-242, 2007/04/01/2007, doi: <https://doi.org/10.1016/j.compstruct.2005.09.004>.
- [36] M. Bocciarelli, P. Colombi, G. Fava, and L. Sonzogni, "Energy-based analytical formulation for the prediction of end debonding in strengthened steel beams," *Composite Structures*, vol. 153, pp. 212-221, 2016, doi: <https://doi.org/10.1016/j.compstruct.2016.05.084>.
- [37] G. Fava, "Strengthening of metallic structures using carbon fiber reinforced polymer materials," PhD Thesis, Department of Structural Engineering, Politecnico di Milano, 2007.
- [38] J. J. Zeng, W. Y. Gao, and F. Liu, "Interfacial behavior and debonding failures of full-scale CFRP-strengthened H-section steel beams," *Composite Structures*, vol. 201, pp. 540-552, 2018, doi: <https://doi.org/10.1016/j.compstruct.2018.06.045>.
- [39] J. G. Teng, T. Yu, and D. Fernando, "Strengthening of steel structures with fiber-reinforced polymer composites," *Journal of Constructional Steel Research*, vol.

- 78, pp. 131-143, 2012/11/01/ 2012, doi: <https://doi.org/10.1016/j.jcsr.2012.06.011>.
- [40] K. Narmashiri, Z. Jumaat, and H. Sulong, "Investigation on end anchoring of CFRP strengthened steel I-beams," *International journal of physical sciences*, vol. 5, no. 9, pp. 1360-1371, 2010.
- [41] H. E. M. Sallam, A. A. M. Badawy, A. M. Saba, and F. A. Mikhail, "Flexural behavior of strengthened steel-concrete composite beams by various plating methods," *Journal of Constructional Steel Research*, vol. 66, no. 8, pp. 1081-1087, 2010/08/01/ 2010, doi: <https://doi.org/10.1016/j.jcsr.2010.03.005>.
- [42] M. H. Seleem, I. A. Sharaky, and H. E. M. Sallam, "Flexural behavior of steel beams strengthened by carbon fiber reinforced polymer plates – Three dimensional finite element simulation," *Materials & Design*, vol. 31, no. 3, pp. 1317-1324, 2010/03/01/ 2010, doi: <https://doi.org/10.1016/j.matdes.2009.09.010>.
- [43] M. Dawood and S. Rizkalla, "Bond and splice behavior of CFRP laminates for strengthening steel beams," *Proceedings of the International Conference on Advanced Composites in Construction*, 2007.
- [44] D. Schnerch and S. Rizkalla, "Flexural Strengthening of Steel Bridges with High Modulus CFRP Strips," *Journal of Bridge Engineering*, vol. 13, no. 2, pp. 192-201, 2008/03/01 2008, doi: [https://doi.org/10.1061/\(ASCE\)1084-0702\(2008\)13:2\(192\)](https://doi.org/10.1061/(ASCE)1084-0702(2008)13:2(192)).
- [45] Y. J. Kim and G. Brunell, "Interaction between CFRP-repair and initial damage of wide-flange steel beams subjected to three-point bending," *Composite Structures*, vol. 93, no. 8, pp. 1986-1996, 2011/07/01/ 2011, doi: <https://doi.org/10.1016/j.compstruct.2011.02.024>.
- [46] H. Zhou, T. L. Attard, Y. Wang, J.-A. Wang, and F. Ren, "Rehabilitation of notch damaged steel beams using a carbon fiber reinforced hybrid polymeric-matrix composite," *Composite Structures*, vol. 106, pp. 690-702, 2013/12/01/ 2013, doi: <https://doi.org/10.1016/j.compstruct.2013.07.001>.
- [47] O. Gunes, O. Buyukozturk, and E. Karaca, "A fracture-based model for FRP debonding in strengthened beams," *Engineering Fracture Mechanics*, vol. 76, no. 12, pp. 1897-1909, 2009/08/01/ 2009, doi: <https://doi.org/10.1016/j.engfracmech.2009.04.011>.
- [48] J. Deng, Y. Jia, and H. Zheng, "Theoretical and experimental study on notched steel beams strengthened with CFRP plate," *Composite Structures*, vol. 136, pp. 450-459, 2016/02/01/ 2016, doi: <https://doi.org/10.1016/j.compstruct.2015.10.024>.
- [49] E. C. Karam, R. A. Hawileh, T. El-Maaddawy, and J. A. Abdallaa, "Experimental investigations of repair of pre-damaged steel-concrete composite beams using CFRP laminates and mechanical anchors," *Thin-Walled Structures*, vol. 112, pp. 107–117, 2017.
- [50] B. El-Taly, "Repairing steel beams with different notch levels using composite materials," *Asian Journal of Civil Engineering*, vol. 19, no. 2, 2018.
- [51] H. Niu and Z. Wu, "Numerical Analysis of Debonding Mechanisms in FRP-Strengthened RC Beams," *Computer-Aided Civil and Infrastructure Engineering*, vol. 20, no. 5, pp. 354-368, 2005/09/01 2005, doi: <https://doi.org/10.1111/j.1467-8667.2005.00402.x>.
- [52] Z. Wu and H. Niu, "Prediction of crack-induced debonding failure in R/C

- structures flexurally strengthened with externally bonded FRP composites," *Doboku Gakkai Ronbunshuu E*, vol. 63, no. 4, pp. 620-639, 2007, doi: <https://10.2208/jsceje.63.620>.
- [53] K. Nakaba, T. Kanakubo, T. Furuta, and H. Yoshizawa, "Bond behavior between fiber-reinforced polymer laminates and concrete," *ACI Structural Journal*, vol. 98, no. 3, 5/1/2001 2001, doi: <https://10.14359/10224>.
- [54] P. M. M. Achintha and C. J. Burgoyne, "Fracture Mechanics of Plate Debonding," *Journal of Composites for Construction*, vol. 12, no. 4, pp. 396-404, 2008/08/01 2008, doi: [https://10.1061/\(ASCE\)1090-0268\(2008\)12:4\(396\)](https://10.1061/(ASCE)1090-0268(2008)12:4(396)).
- [55] D. E. Branson, "Design Procedures for Computing Deflections," *ACI Journal*, vol. 65, no. 9, 9/1/1968, doi: <https://10.14359/7508>.
- [56] B. Täljsten, "Strengthening of beams by plate bonding," *Journal of Materials in Civil Engineering*, vol. 9(4), pp. 206-212, 1997.
- [57] *Guide for the design and construction of externally bonded FRP systems for strengthening concrete structures (ACI 440.2R-17)*, American Concrete Institute (ACI), 2017.
- [58] P. Wantanasiri and A. Lenwari, "Intermediate crack-induced debonding analysis for RC beams strengthened with FRP plates," *Structural Engineering and Mechanics*, vol. 56, pp. 473-490, 2015, doi: <https://10.12989/sem.2015.56.3.473>.
- [59] *Standard Test Methods and Definitions for Mechanical Testing of Steel Products (ASTM A370-17a)*, American Society for Testing and Materials (ASTM), 2017.
- [60] *Design of Steel Structures: Eurocode 3: Design of steel structures, Part 1-1 - General rules and rules for buildings, First Edition*, European Committee for Standardization (CEN), 2005.
- [61] Sika (Thailand) Limited, "Product Data Sheet: Sikadur®-30," 2017, doi: https://tha.sika.com/dms/getdocument.get/c421a0fc-54d0-3dfb-b213-922efcc2f307/Sika%20PDS_E_Sikadur%20-30.pdf.
- [62] J. Deng, J. Li, Y. Wang, and W. Xie, "Numerical study on notched steel beams strengthened by CFRP plates," *Construction and Building Materials*, vol. 163, pp. 622–633, 2018, doi: <https://doi.org/10.1016/j.conbuildmat.2017.12.110>.
- [63] O. H. Elkhabeery, S. S. Safar, and S. A. Mourad, "Flexural strength of steel I-beams reinforced with CFRP sheets at tension flange," *Journal of Constructional Steel Research*, vol. 148, pp. 572–588, 2018, doi: <https://doi.org/10.1016/j.jcsr.2018.05.038>.
- [64] J. He and G. Xian, "Debonding of CFRP-to-steel joints with CFRP delamination," *Composite Structures*, vol. 153, pp. 12–20, 2016, doi: <https://dx.doi.org/10.1016/j.compstruct.2016.05.100>.
- [65] A. H. Korayem, C. Y. Li, Q. H. Zhang, X. L. Zhao, and W. H. Duan, "Effect of carbon nanotube modified epoxy adhesive on CFRP-to-steel interface," *Composites Part B: Engineering*, vol. 79, pp. 95-104, 2015, doi: <http://dx.doi.org/10.1016/j.compositesb.2015.03.063>.
- [66] C. Li, L. Ke, J. He, Z. Chen, and Y. Jiao, "Effects of mechanical properties of adhesive and CFRP on the bond behavior in CFRP-strengthened steel structures," *Composite Structures*, vol. 211, pp. 163–174, 2019, doi: <https://doi.org/10.1016/j.compstruct.2018.12.020>.
- [67] C. Fragassa and M. Ippoliti, "Technology assessment of tire mould cleaning systems and quality finishing," *International Journal for Quality Research*, vol.

- 10, no. 3, pp. 523–546, 2016, doi: <https://doi.org/10.18421/IJQR10.03-06>.
- [68] D. Fernando, J. G. Teng, T. Yu, and X. L. Zhao, "Preparation and characterization of steel surfaces for adhesive bonding," *Journal of Composites for Construction*, vol. 17, no. 6, p. 04013012, 2013, doi: [https://doi.org/10.1061/\(ASCE\)CC.1943-5614.0000387](https://doi.org/10.1061/(ASCE)CC.1943-5614.0000387).
- [69] *Preparation of steel substrates before application of paints and related products — visual assessment of surface cleanliness—Part 1: rust grades and preparation grades of uncoated steel substrates and of steel substrates after overall removal of previous coatings (EN ISO 8501-1)*, European Committee for Standardization (CEN), 2007.
- [70] S. K. Sinha and B. J. Briscoe, *Polymer Tribology*. 2009.





APPENDICES

จุฬาลงกรณ์มหาวิทยาลัย
CHULALONGKORN UNIVERSITY

APPENDIX A

EXPERIMENTS CHECKING

Validation checking of four-point flexural testing is investigated to ensure the precision and accuracy of the experiment. This appendix presents a signal analysis methodology to check the symmetry of load applied on tested beams (see A.1) and midspan displacement rate (see A.2) throughout the experiment. A sampling rate of 100 Hz was used in the datalogging process for detecting both pre-peak and post-peak responses.

A.1 Symmetry of the Applied Load

Figure A.1 to Figure A.3 show load-deflection curves of unstrengthened beams. These indicate the symmetry of applied load since the deflections measured by DT1 is very close to the deflection measured by DT3.

The relationship between load and measured deflection of FRP-strengthened beams are also plotted in Figure A.4 to Figure A.13. The applied load configuration used for the testing of FRP-strengthened beams is appeared to be symmetrical. At each certain load level before the maximum applied load, the deflections measured by DT1 is very close to the deflection measured by DT4. Likewise, the midspan deflection measured by DT2 and DT3 are identical.

The symmetry of applied load lost after the midspan deflection beyond the value of midspan deflection at maximum applied load. The strength degradation is not uniform over the points of deflection measurement. These may be caused by the FRP debonding initiation induced applied load softening and structural instability.

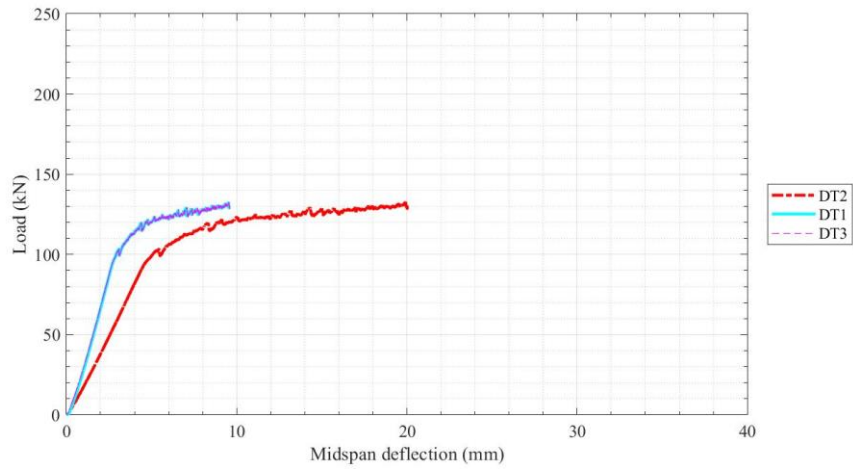


Figure A.1 Load-deflection curve of beam CBM.

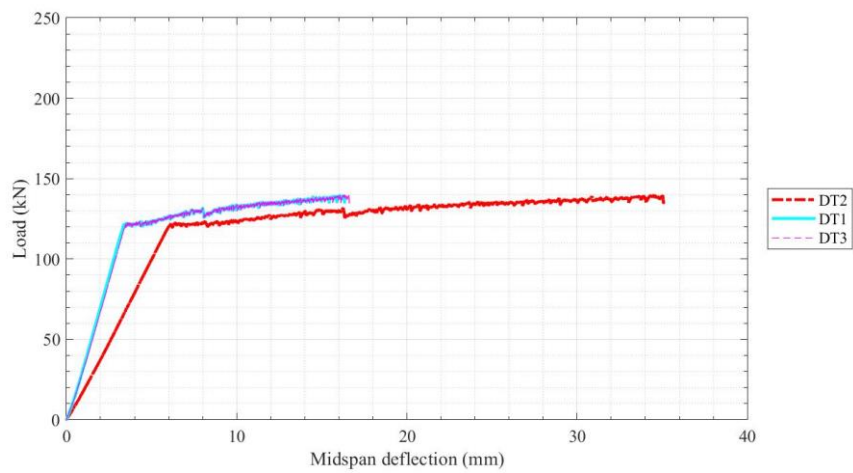


Figure A.2 Load-deflection curve of beam CBMY.

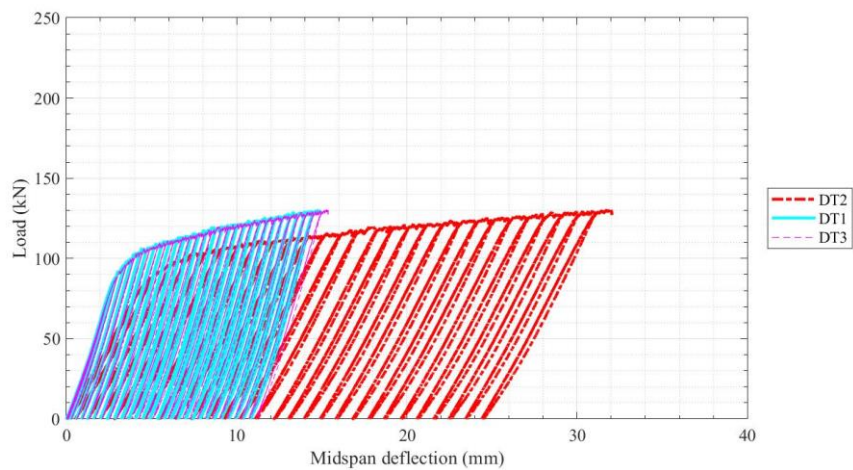


Figure A.3 Load-deflection curve of beam CBP.

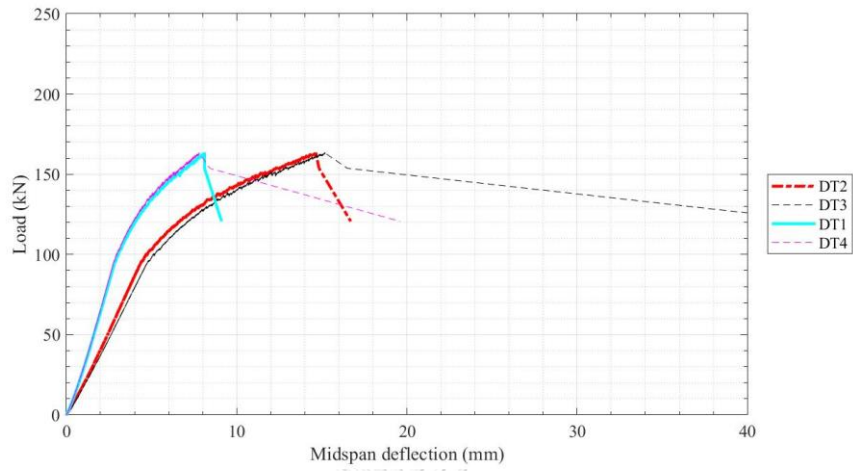


Figure A.4 Load-deflection curve of beam BMM120-0.

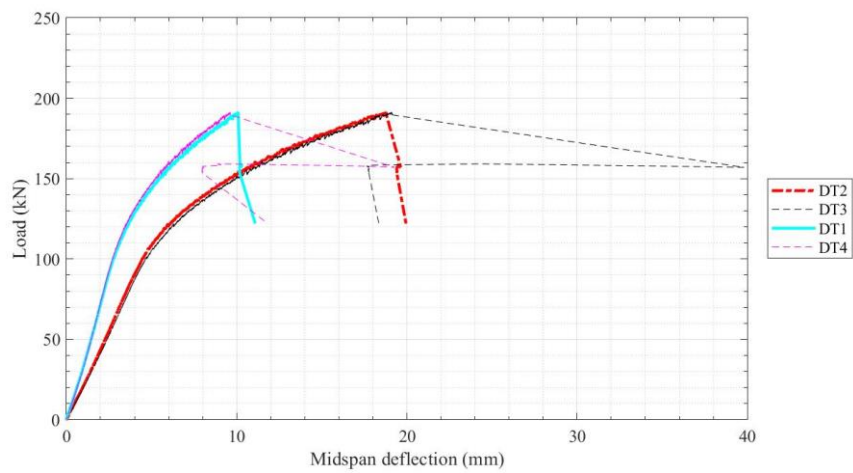


Figure A.5 Load-deflection curve of beam BMM120-50.

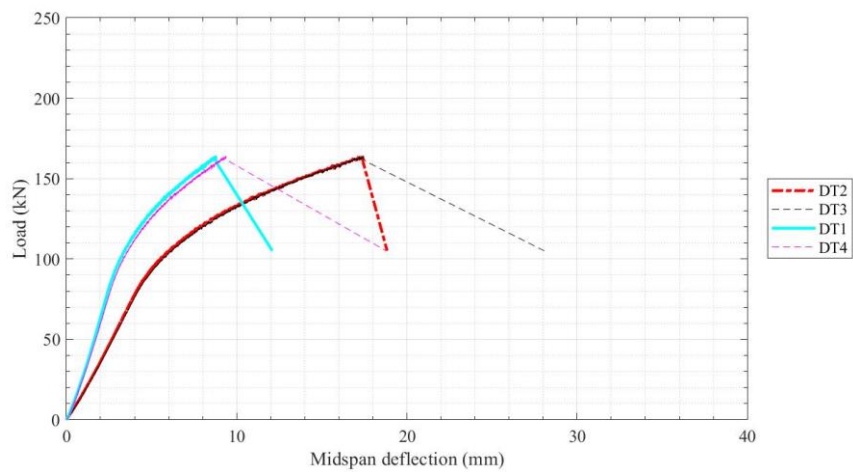


Figure A.6 Load-deflection curve of beam BMM120-100.

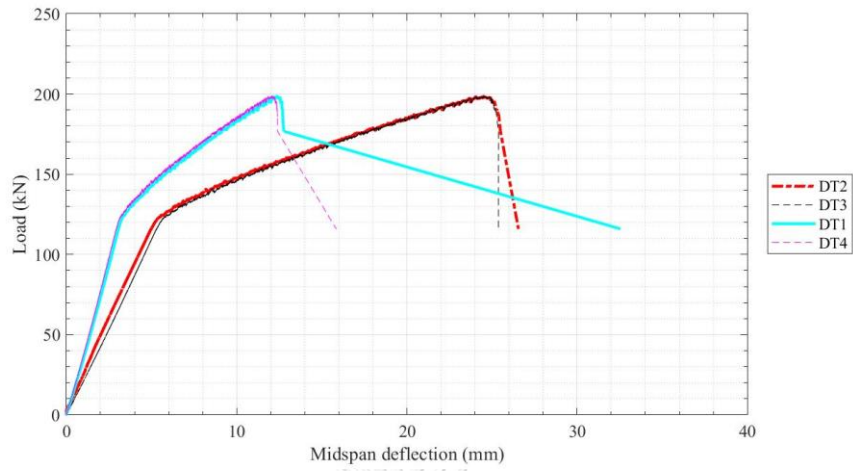


Figure A.7 Load-deflection curve of beam BMM120Y-100.

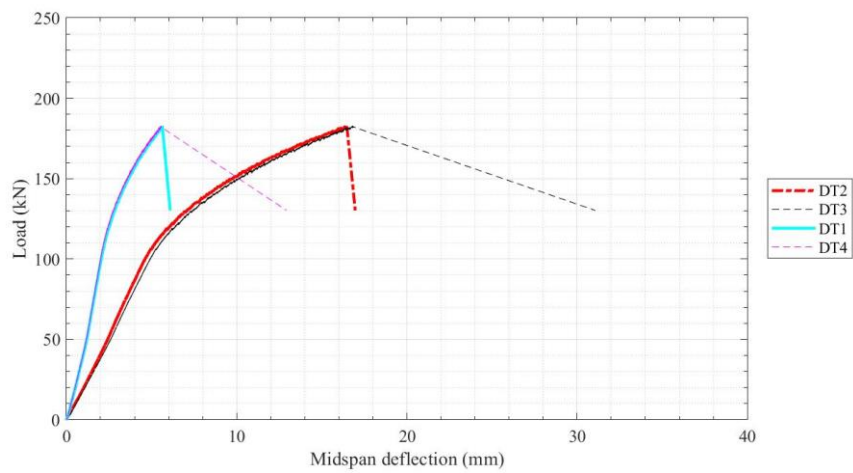


Figure A.8 Load-deflection curve of beam BMM150-100.

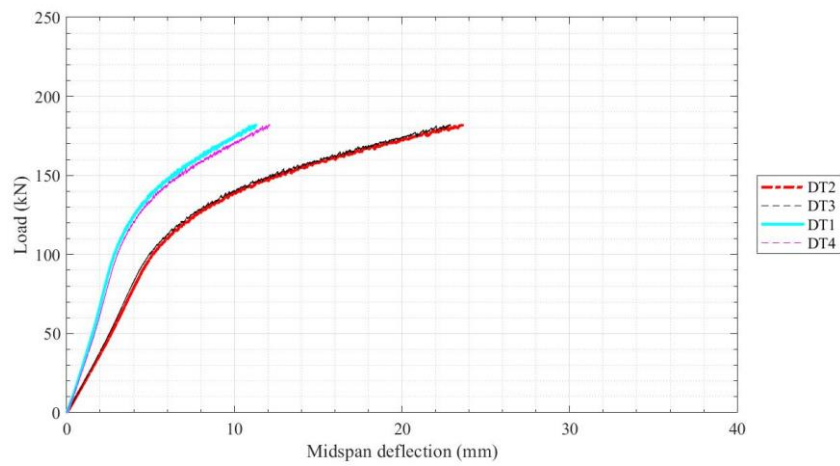


Figure A.9 Load-deflection curve of beam BSM120-0.

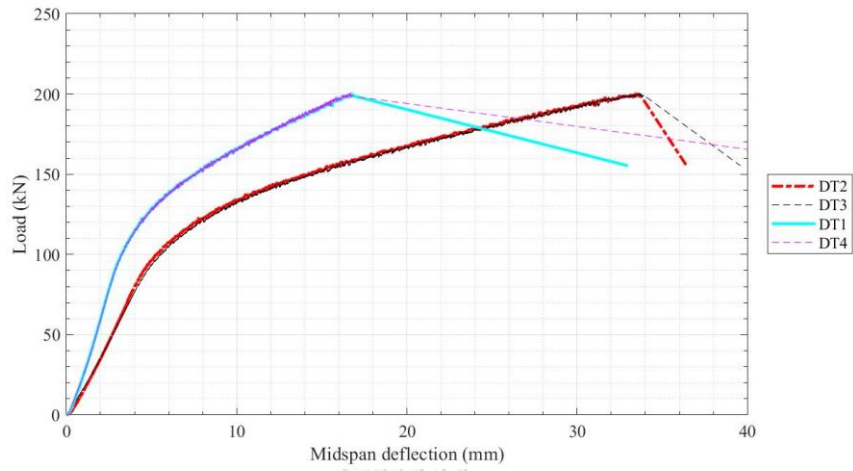


Figure A.10 Load-deflection curve of beam BSM120-100.

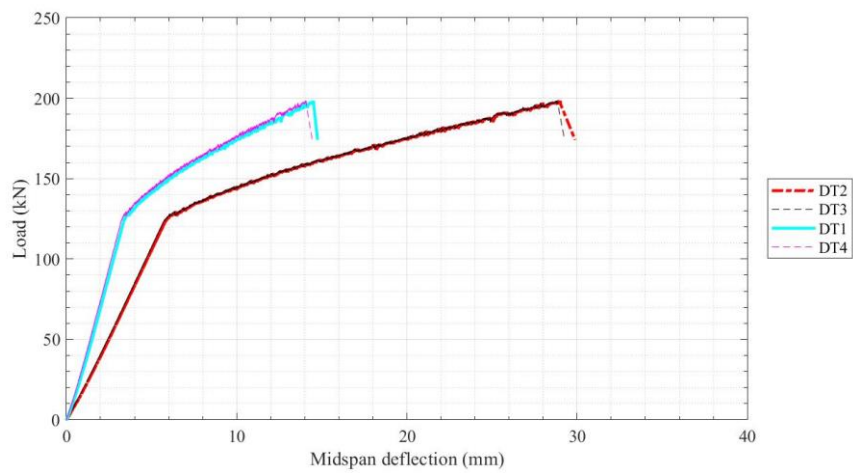


Figure A.11 Load-deflection curve of beam BSM120Y-100.

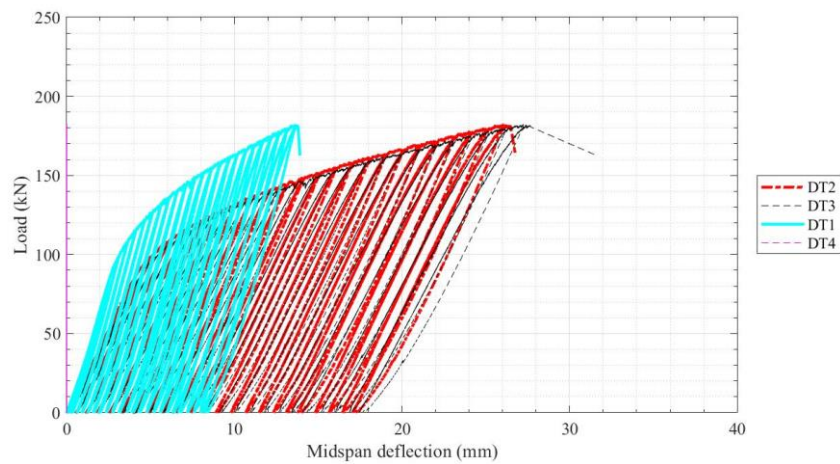


Figure A.12 Load-deflection curve of beam BSP120-100.

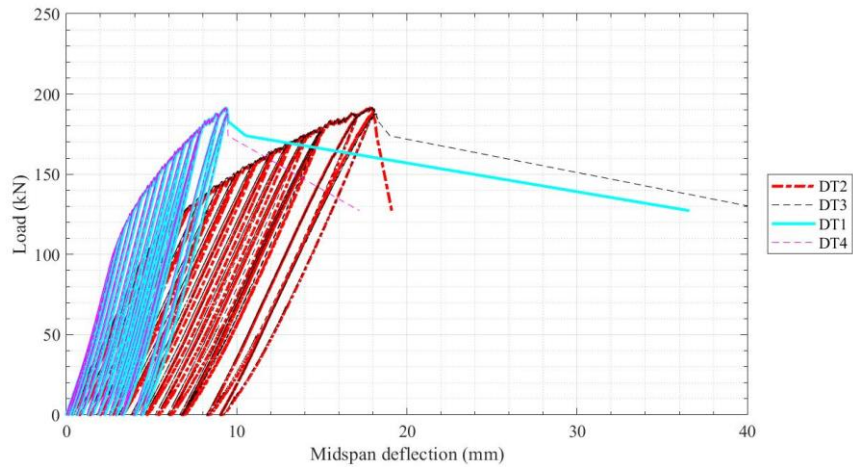


Figure A.13 Load-deflection curve of beam BMP120-100.

A.2 Loading Rate

Expected rate of midspan deflection rate is 1mm/min for all monotonic tested beams. Displacement rate is examined by plotting between midspan deflection measured by DT2 versus time. Figure A.14 to Figure A.23 present the actual midspan deflection rate obtained from datalogger with respected to the expected rate of monotonic tested beams. The actual rate is found to be consistent with the expected rate. The last value of the measured midspan deflection is associated with a post-peak applied load.

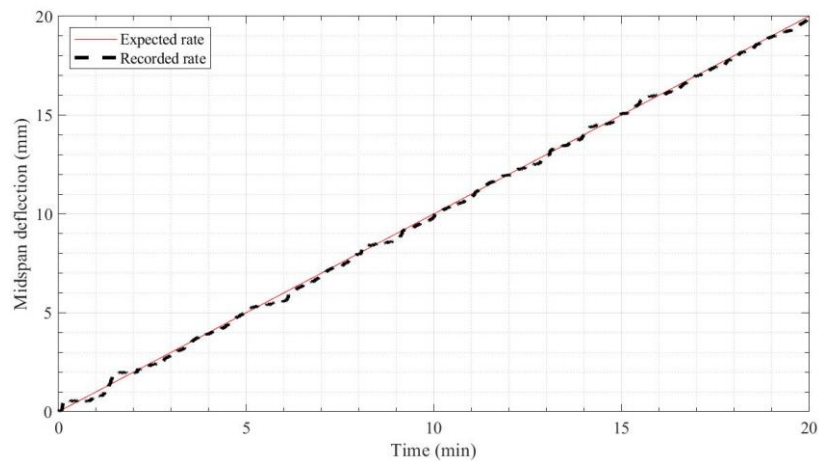


Figure A.14 Displacement rate of beam CBM.

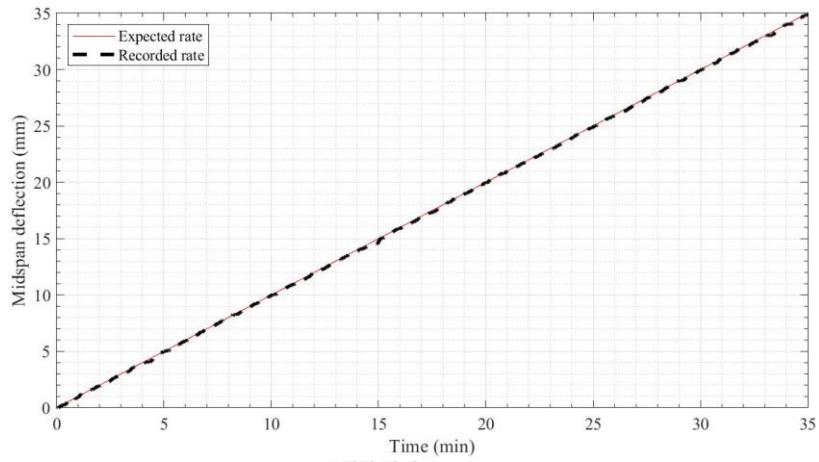


Figure A.15 Displacement rate of beam CBMY.

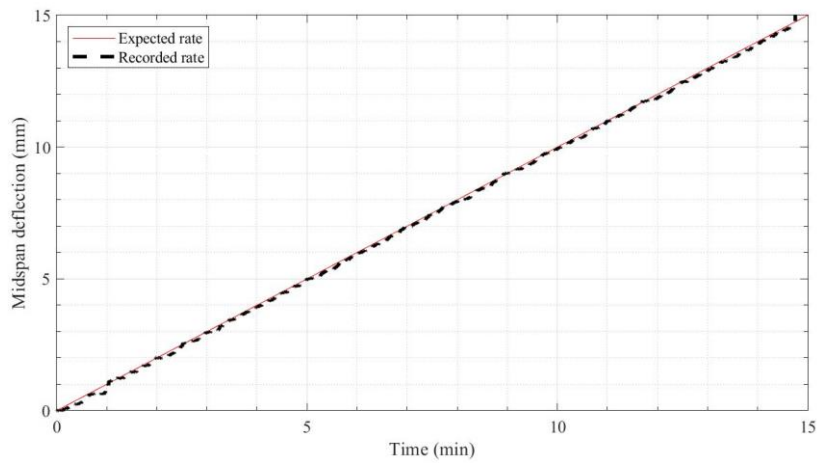


Figure A.16 Displacement rate of beam BMM120-0.

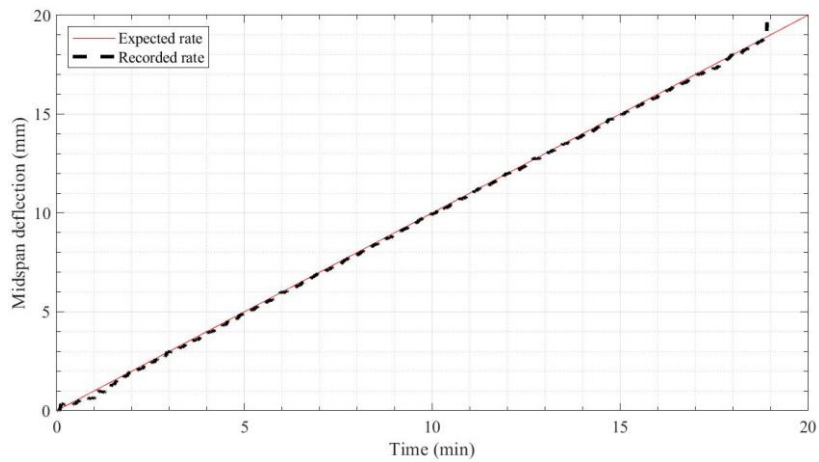


Figure A.17 Displacement rate of beam BMM120-50.

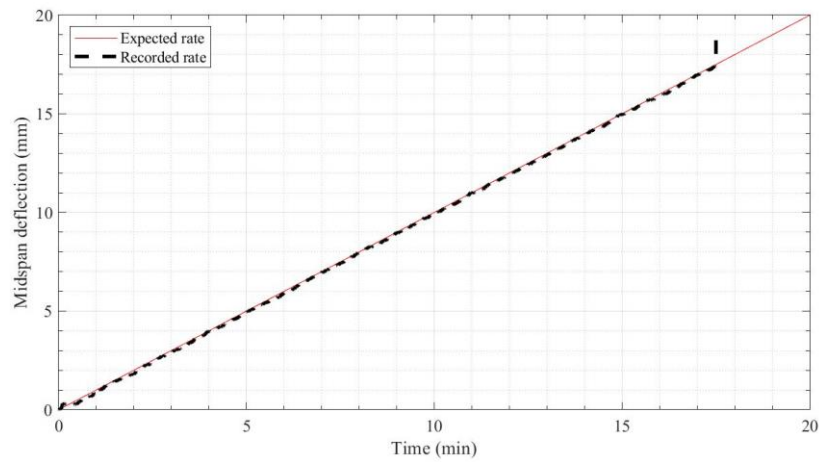


Figure A.18 Displacement rate of beam BMM120-100.

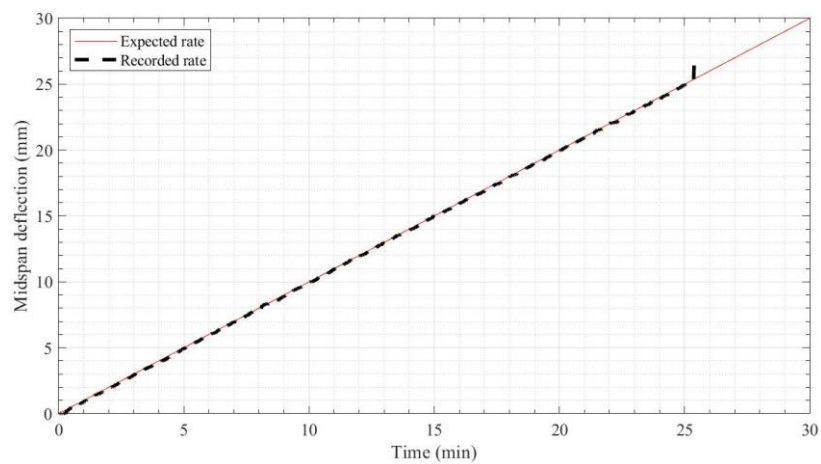


Figure A.19 Displacement rate of beam BMM120Y-100.

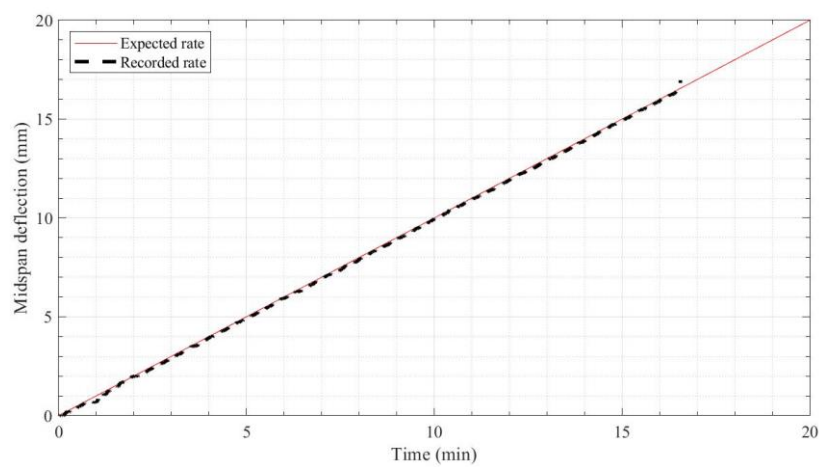


Figure A.20 Displacement rate of beam BMM150-100.

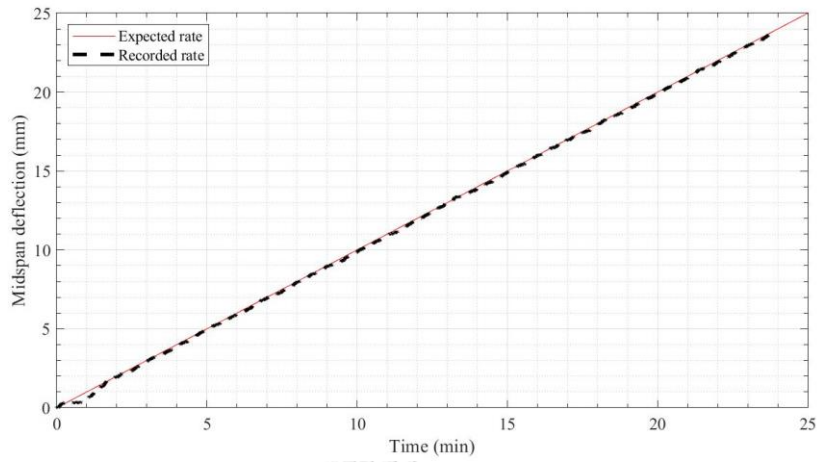


Figure A.21 Displacement rate of beam BSM120-0.

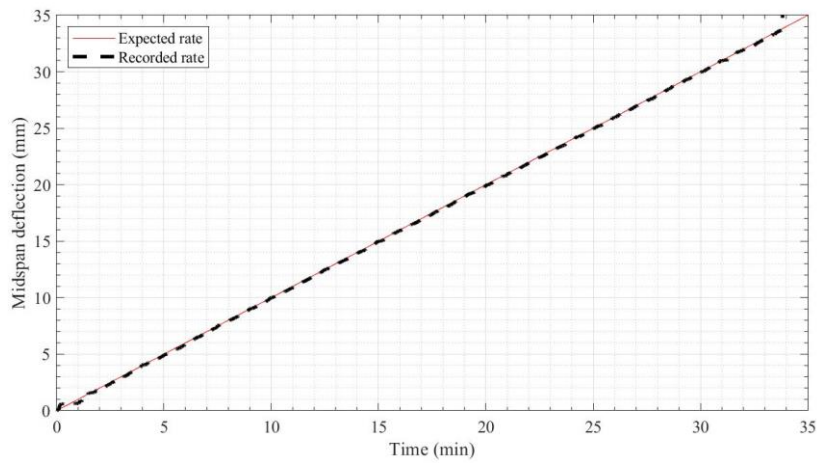


Figure A.22 Displacement rate of beam BSM120-100.

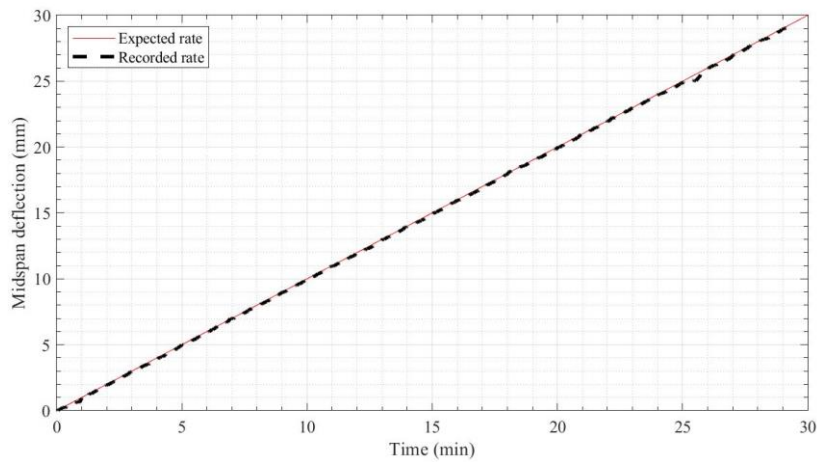


Figure A.23 Displacement rate of beam BSM120Y-100.

Midspan deflection rate of midspan deflection rate of all periodic unloading tested beam are plotted in Figure A.24 to Figure A.26. Permanent midspan deflection is observed after the midspan deflection of beams beyond the yielding point. Increasing of midspan deflection at 1mm/min is controllable. After the yielding point of beams, applied load could be unloaded to the zero-force value. Decreasing of midspan deflection about 1.67% of maximum deflection in each cycle per second is attempted to control. Increasing of midspan deflection in the next cycle was repeated as soon as the permanent midspan deflection is observed.

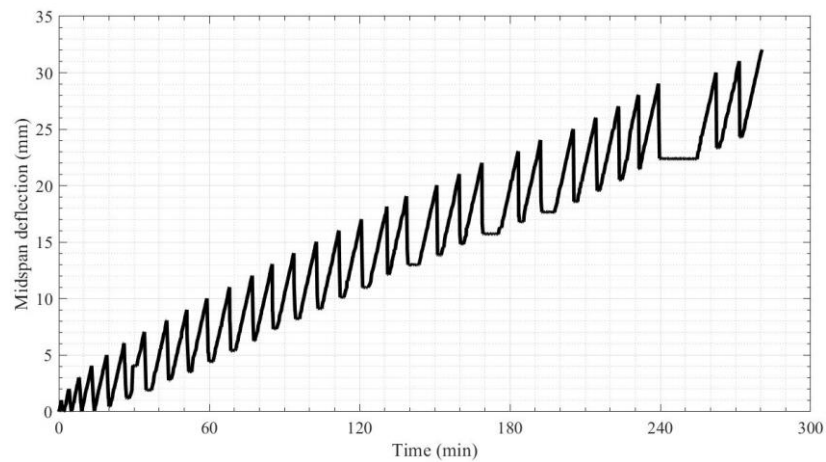


Figure A.24 Displacement rate of beam CBP.

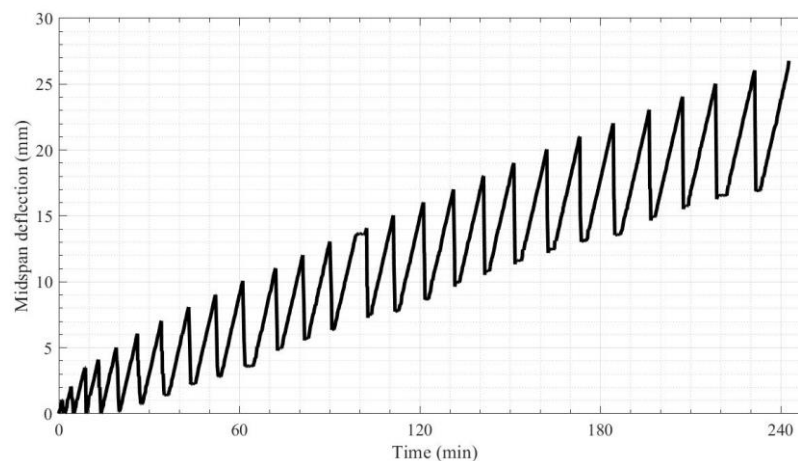


Figure A.25 Displacement rate of beam BSP120-100.

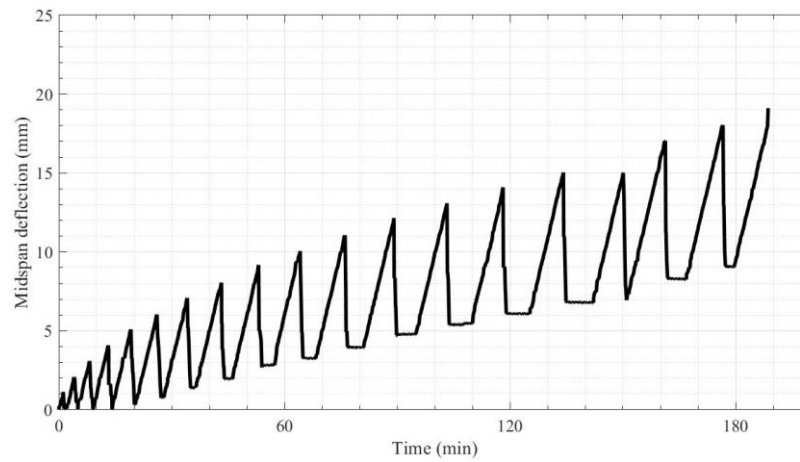


Figure A.26 Displacement rate of beam BMP120-100.



APPENDIX B

PRE-PEAK BEHAVIOR OF TESTED BEAMS

Strain gage signals before an applied load reaches the maximum value are presented in this appendix to examine the flexural behavior in detail. Section B.1 exhibits the definition of yielding point by investigating the relationship between load and strain affixed on the bottom surface of bottom flange. All strain gages installed at the midspan section are presented in section B.2 and B.3 to observe strain distribution across the cross section at midspan. Steel strain within the constant moment region is focused in section B.4 and B.5 by plotting all strains attached on the bottom surface of bottom flange. FRP strain distribution when an applied load increased is also investigated in section B.6 and B.7.

B.1 Definition of Yielding Point

Load-steel strain curves at midspan section of unstrengthened beams are plotted in Figure B.1 and Figure B.2. It is found that the steel strain of unstrengthened beams is proportioned to the applied load before the yielding load. When an applied load of the beam CBM is higher than the yielding load, applied load is not proportioned to the strains. This phenomenon did not occur in beam CBMY. This may be caused by multidirectional stress state due to flexure and material instability due to beyond yielding point. During the increasing of applied load, steel strain of bottom flange under flexure may not similarly developed as the steel strain of coupons under pure tension.

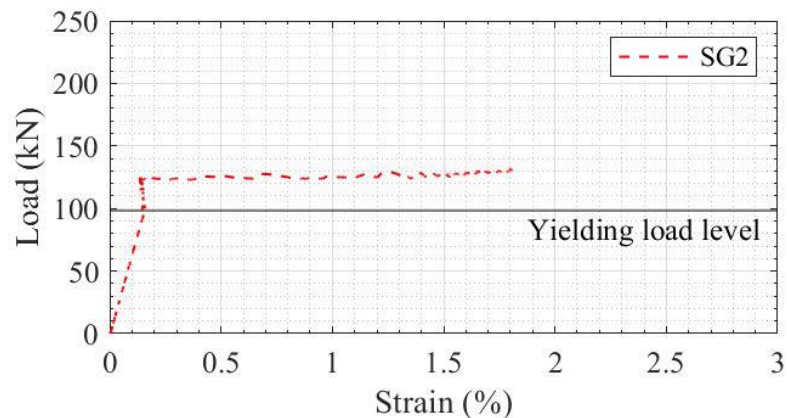


Figure B.1 Bottom flange strain of beam CBM.

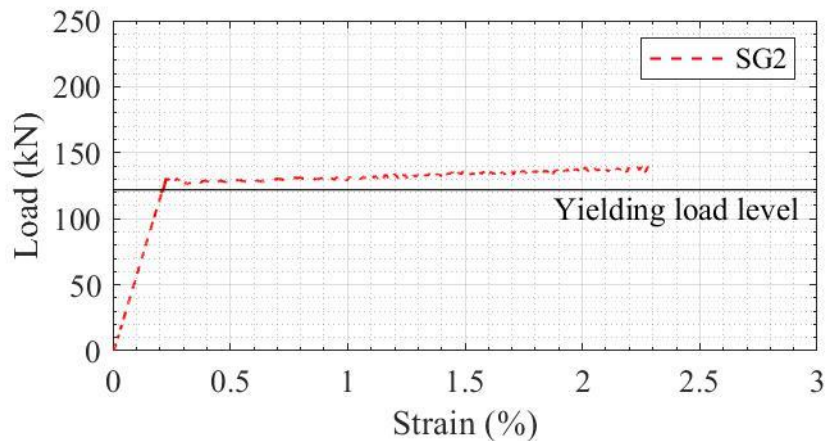


Figure B.2 Bottom flange strain of beam CBMY.

Load-steel strain curves at midspan section of FRP-strengthened beams are plotted in Figure B.3 to Figure B.10. The beams show a well-proportioned relationship between load and strain before the yielding load. Trends of steel strain after the applied load beyond the yielding value are unexplainable with the recent knowledge. The presence and absence of initial bond defect, the use of different FRP modulus, and predamage are not affected to the trend of strain development after the yielding point. Note that the steel strain at midspan (measured by SG9) always produced the maximum strain compared to the adjacent steel strain measured by SG7 and SG14.

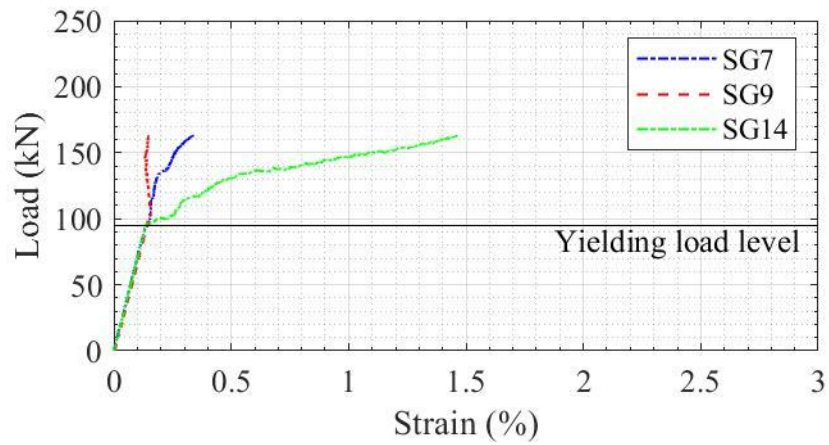


Figure B.3 Bottom flange strain of beam BMM120-0.

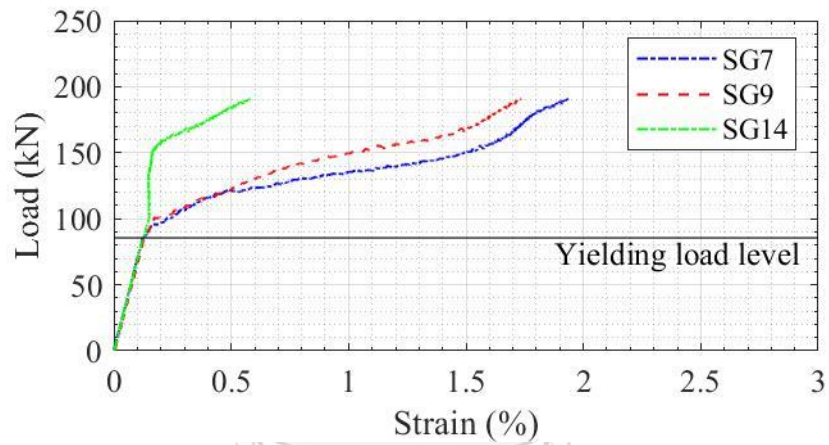


Figure B.4 Bottom flange strain of beam BMM120-50.

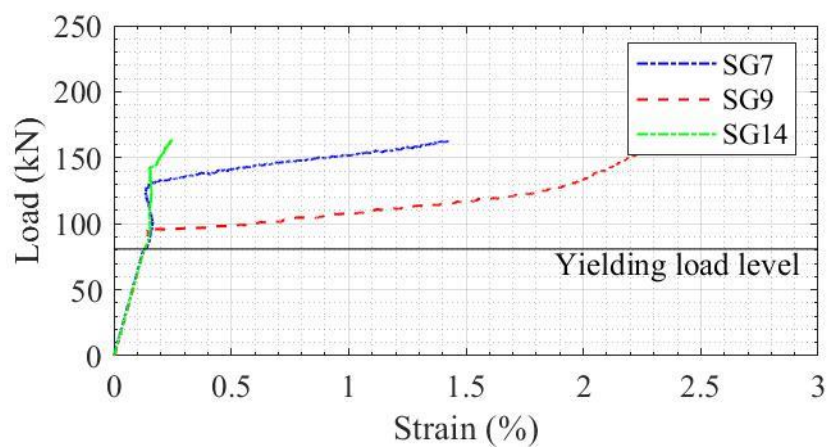


Figure B.5 Bottom flange strain of beam BMM120-100.

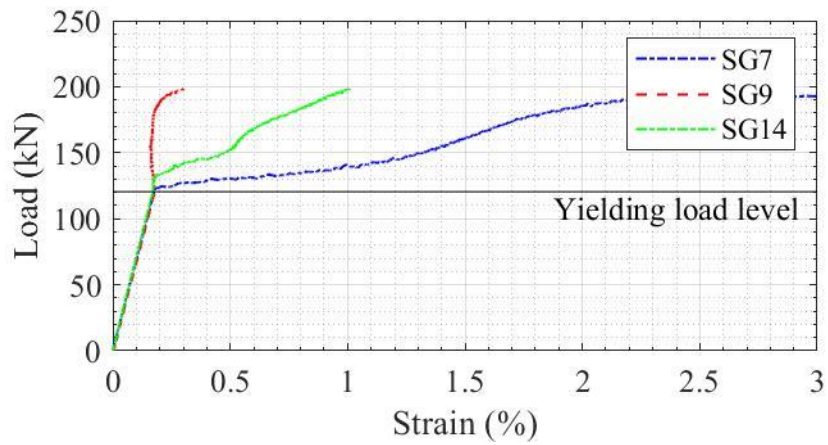


Figure B.6 Bottom flange strain of beam BMM120Y-100.

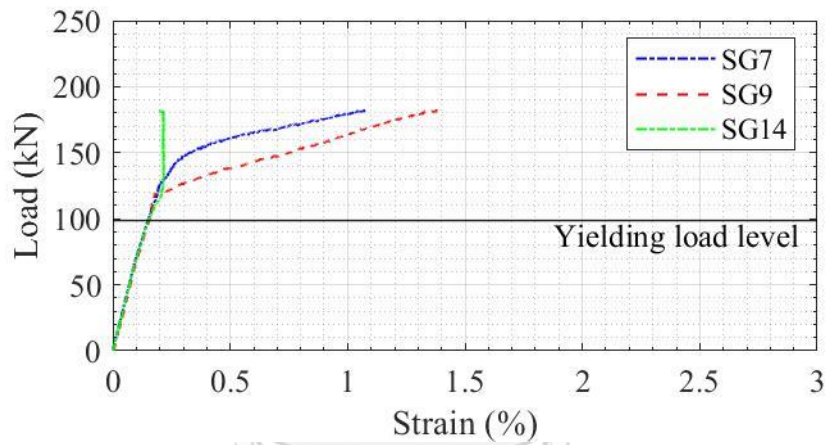


Figure B.7 Bottom flange strain of beam BMM150-100.

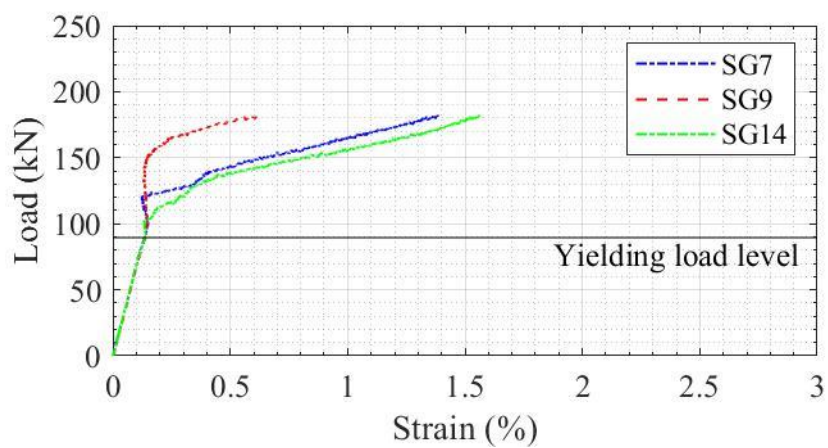


Figure B.8 Bottom flange strain of beam BSM120-0.

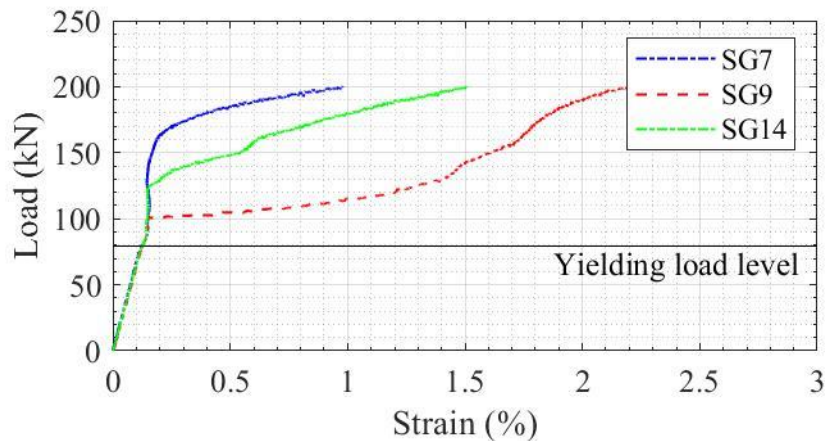


Figure B.9 Bottom flange strain of beam BSM120-100.

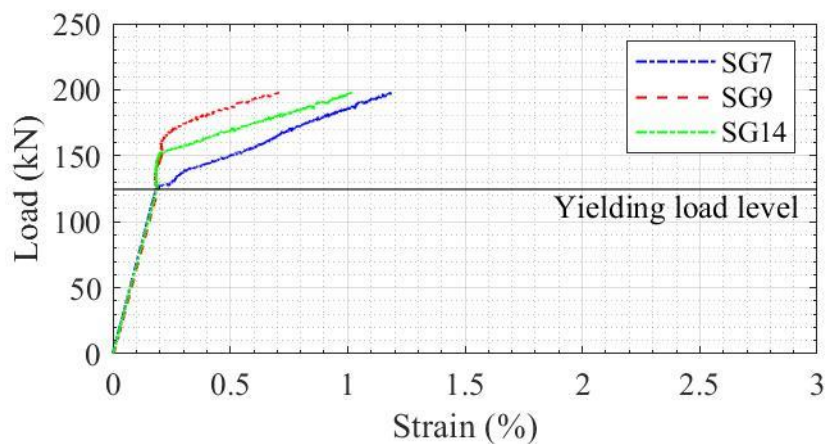


Figure B.10 Bottom flange strain of beam BSM120Y-100.

B.2 Strain Distribution at Midspan Section (Before Yielding)

Development of strain at midspan section before the yielding state is plotted in Figure B.11 to Figure B.22. Applied load is separated into five levels. Each increment of load level is equal to 20% of yielding load. The fifth load level is equal to the yielding load. It is found that strain at bottom surface of top flange was usually more than strain at top surface of the cover plate. Although the cover plate was precisely welded to the top flange, these results showed that the composite action was not fully activated before the yielding state. This issue should be one of further consideration since many steel structures used welding connection between beam and deck components.

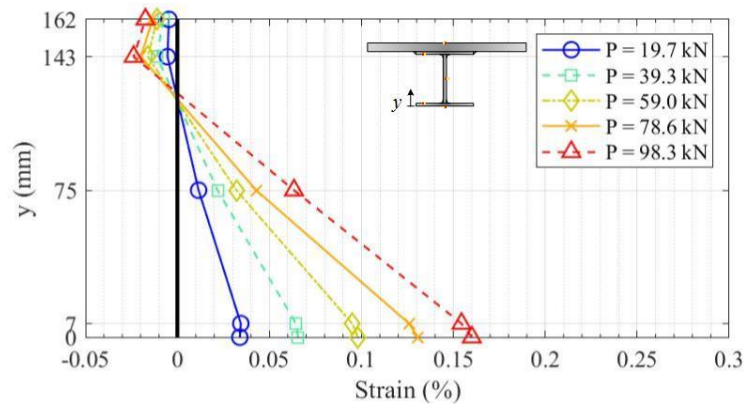


Figure B.11 Strain at midspan section of beam CBM (before yielding).

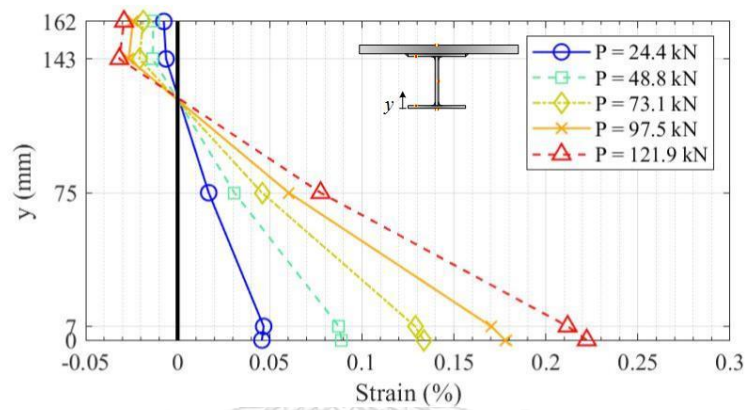


Figure B.12 Strain at midspan section of beam CBMY (before yielding).

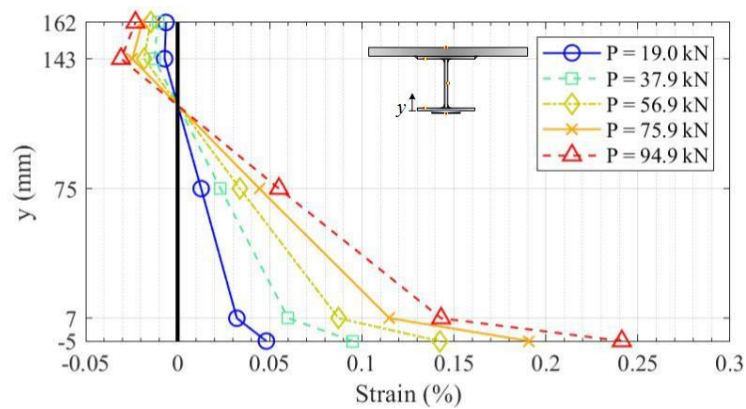


Figure B.13 Strain at midspan section of beam BMM120-0 (before yielding).

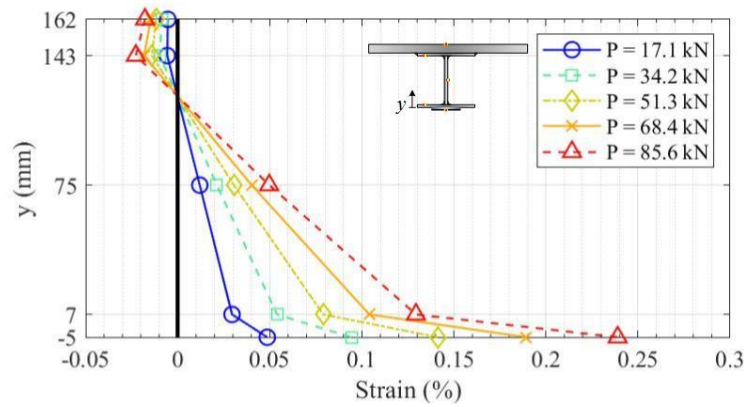


Figure B.14 Strain at midspan section of beam BMM120-50 (before yielding).

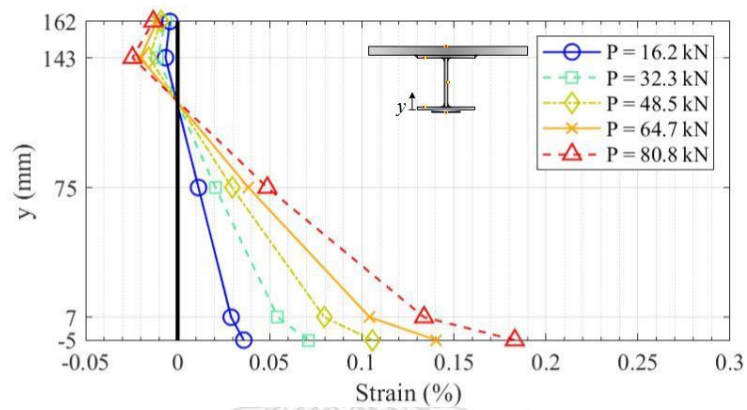


Figure B.15 Strain at midspan section of beam BMM120-100 (before yielding).

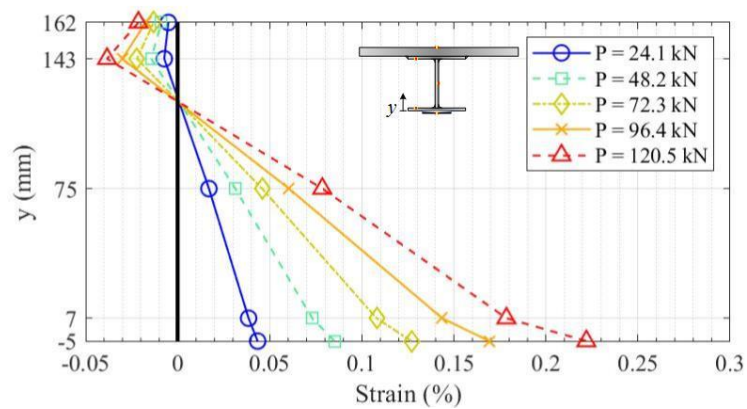


Figure B.16 Strain at midspan section of beam BMM120Y-100 (before yielding).

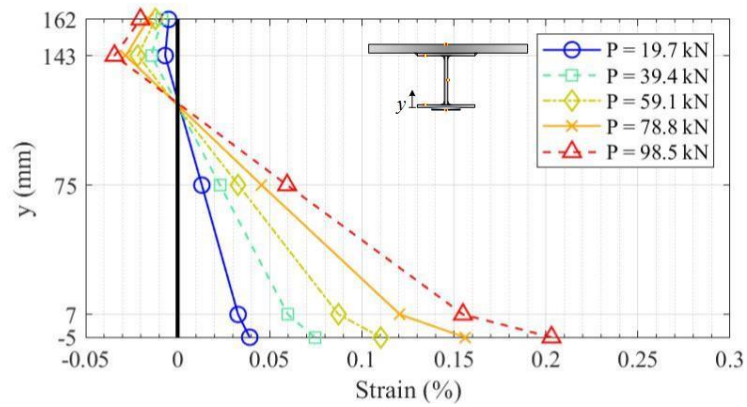


Figure B.17 Strain at midspan section of beam BMM150-100 (before yielding).

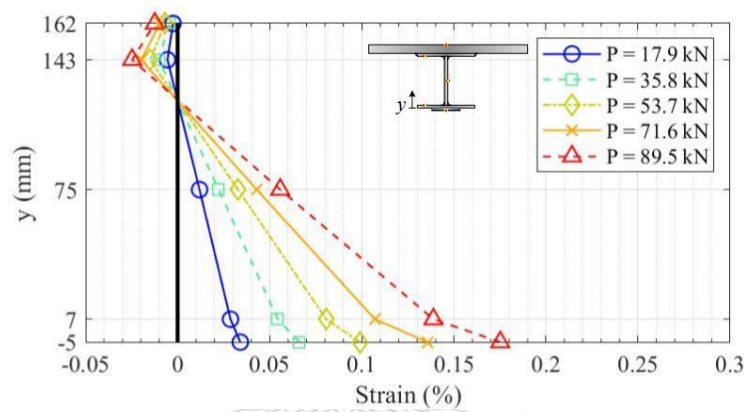


Figure B.18 Strain at midspan section of beam BSM120-0 (before yielding).

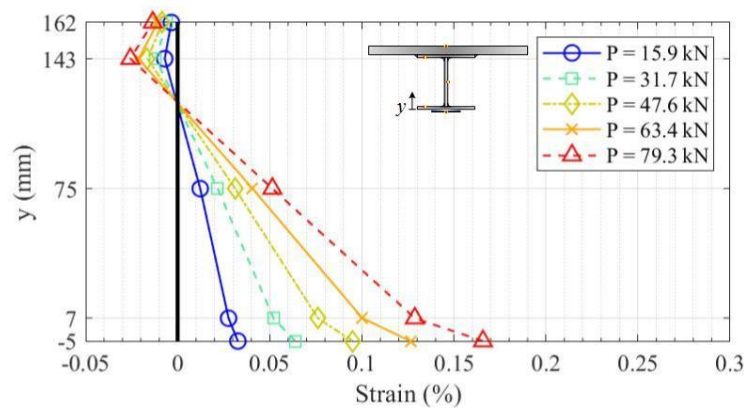


Figure B.19 Strain at midspan section of beam BSM120-100 (before yielding).

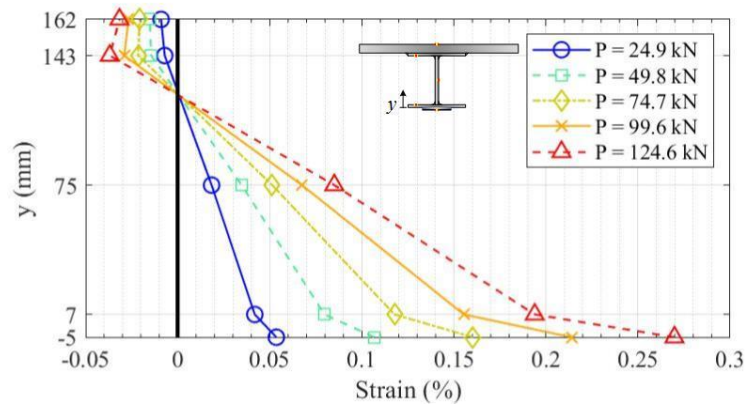


Figure B.20 Strain at midspan section of beam BSM120Y-100 (before yielding).

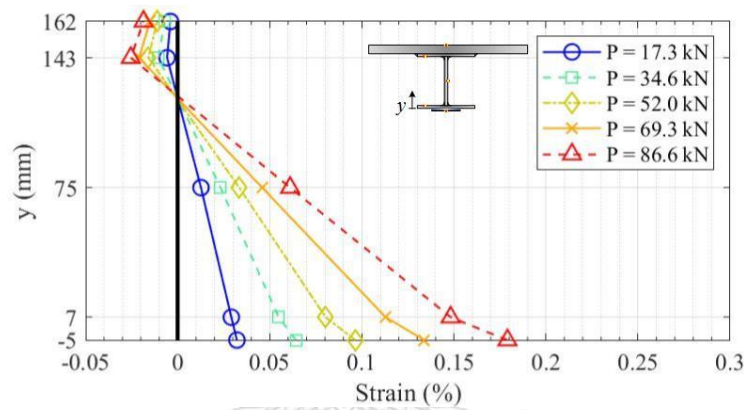


Figure B.21 Strain at midspan section of beam BSP120-100 (before yielding).

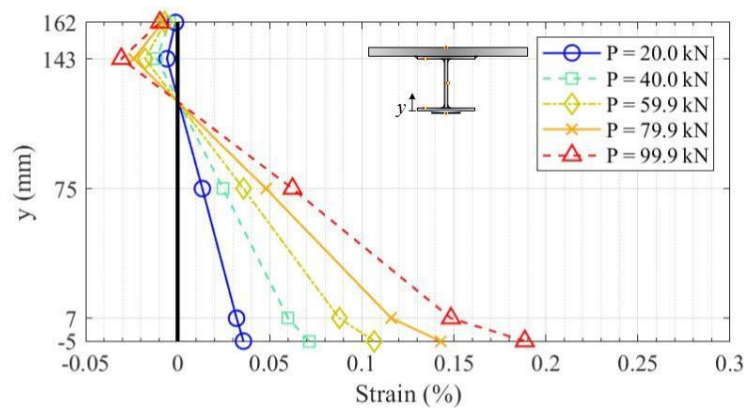


Figure B.22 Strain at midspan section of beam BMP120-100 (before yielding).

B.3 Strain Distributions at Midspan Section (Between Yield and Maximum Loads)

Development of strain at midspan section between the yielding state and the state that applied load reached the maximum value is plotted in Figure B.23 and Figure B.34. Applied load is separated into five levels. Each increment of load level is equal to 20% of the difference between yielding load and maximum load. The first load level is equal to the yielding load. The fifth load level is equal to the maximum load. It was found that strains of most beams were aggressively increased at the maximum load level. The phenomenon that indicates the higher top flange strain compared to the cover plate is disappeared after beams beyond the yielding state. At maximum load, beam CBMY is found that strain at top surface of bottom flange was slightly higher than the corresponding value at bottom surface of bottom flange. This may be a little variant strain due to large deformation of steel.

Strain at top surface of bottom flange of beam BSM120-0, BMM120-0, and BMM120Y-100 are found to be less than the corresponding strain at midweb. This may be caused by FRP restraint as discussed in section 5.4.

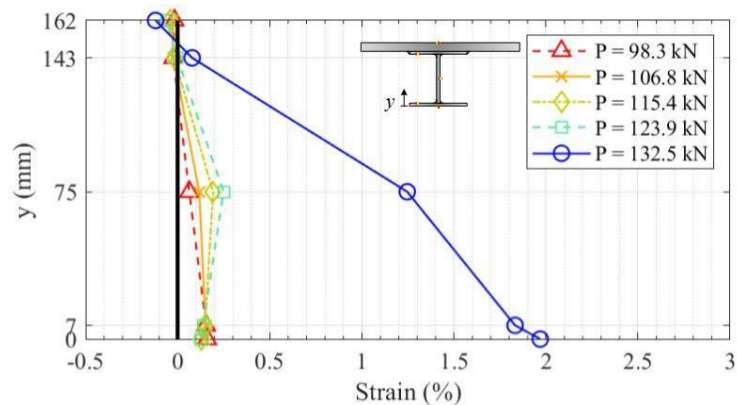


Figure B.23 Strain at midspan section of beam CBM (between yield and maximum load).

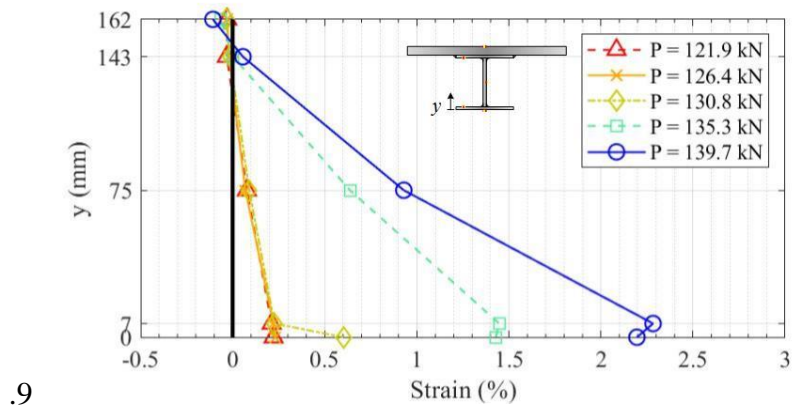


Figure B.24 Strain at midspan section of beam CBMY (between yield and maximum load).

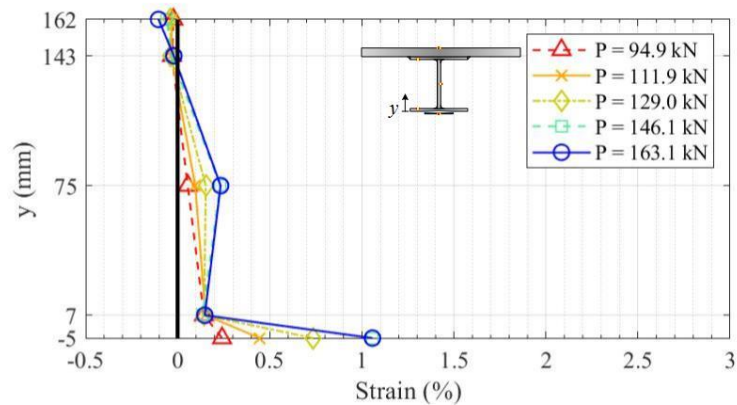


Figure B.25 Strain at midspan section of beam BMM120-0 (between yield and maximum load).

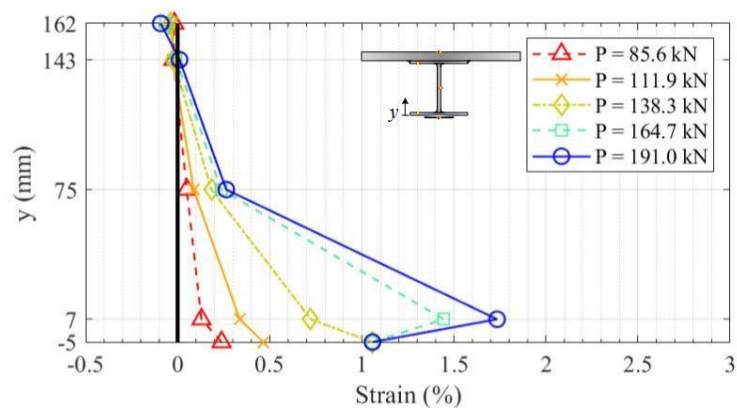


Figure B.26 Strain at midspan section of beam BMM120-50 (between yield and maximum load).

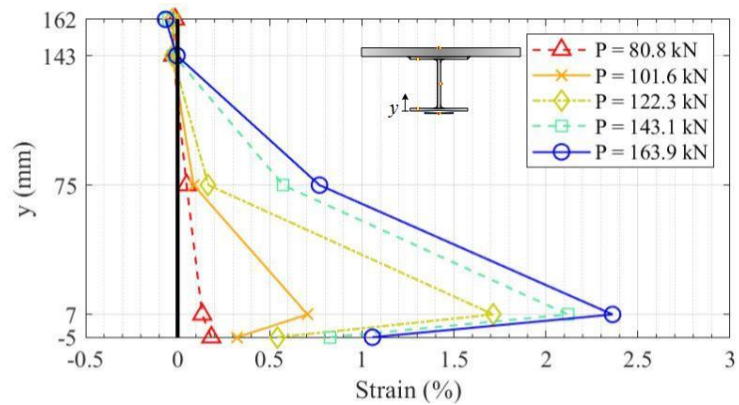


Figure B.27 Strain at midspan section of beam BMM120-100 (between yield and maximum load).

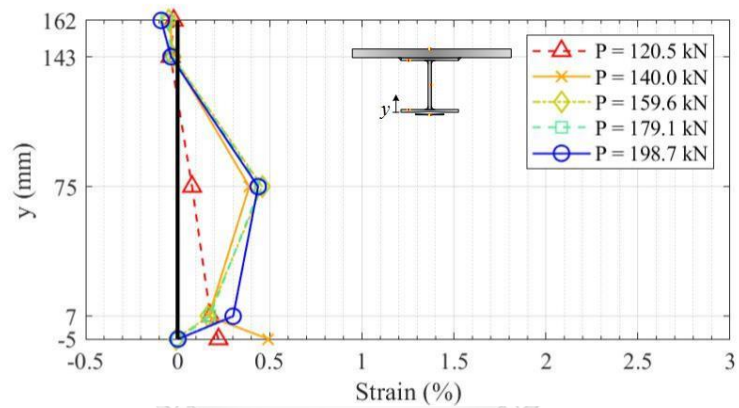


Figure B.28 Strain at midspan section of beam BMM120Y-100 (between yield and maximum load).

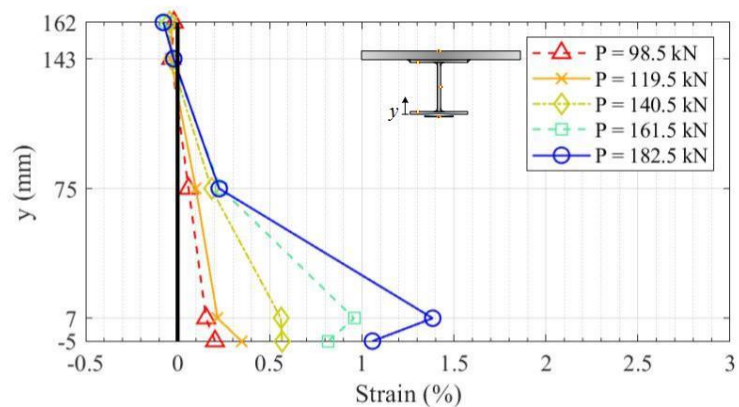


Figure B.29 Strain at midspan section of beam BMM150-100 (between yield and maximum load).

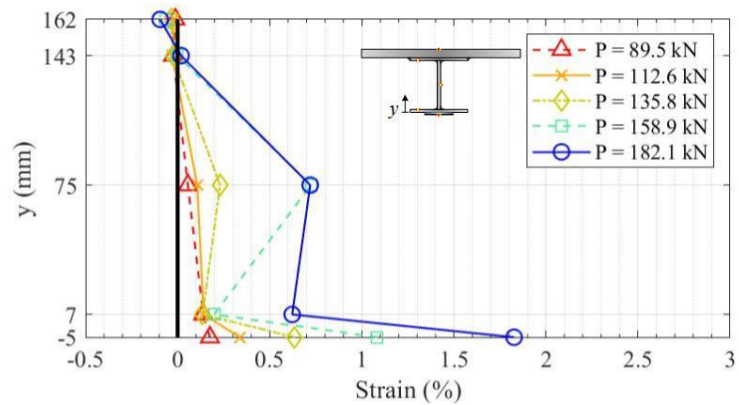


Figure B.30 Strain at midspan section of beam BSM120-0 (between yield and maximum load).

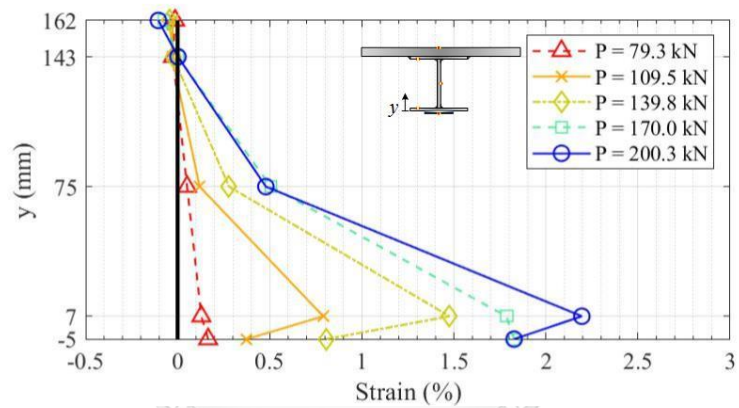


Figure B.31 Strain at midspan section of beam BSM120-100 (between yield and maximum load).

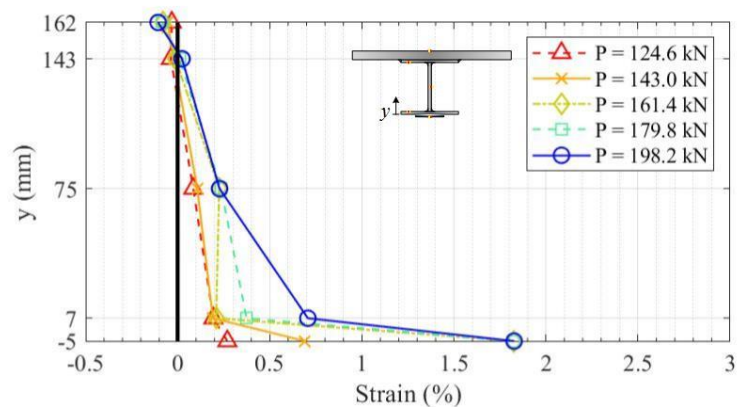


Figure B.32 Strain at midspan section of beam BSM120Y-100 (between yield and maximum load).

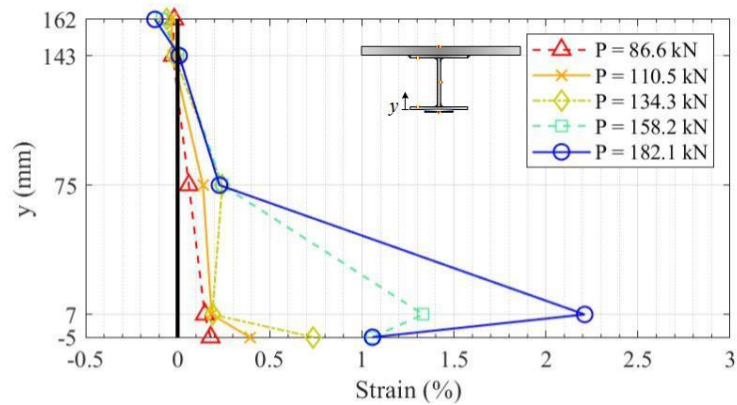


Figure B.33 Strain at midspan section of beam BSP120-100 (between yield and maximum load).

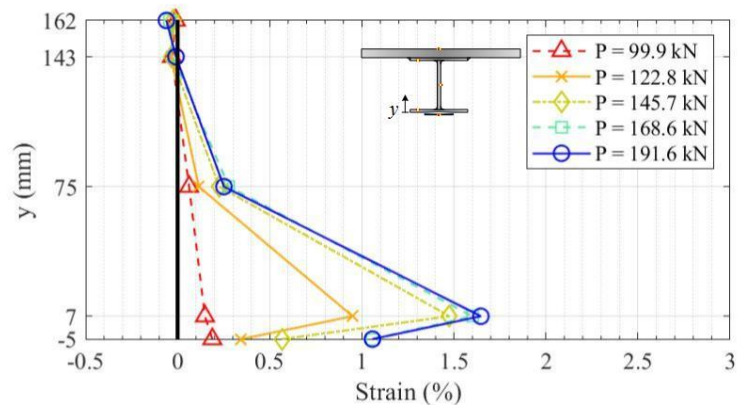


Figure B.34 Strain at midspan section of beam BMP120-100 (between yield and maximum load).

B.4 Strain Distributions of Steel in Vicinity of Midspan Section (Before Yielding)

Development of strain in vicinity of midspan section in constant moment region before the yielding state is plotted in Figure B.35 to Figure B.44. Applied load is separated into five levels. Each increment of load level is equal to 20% of yielding load. The fifth load level is equal to the yielding load.

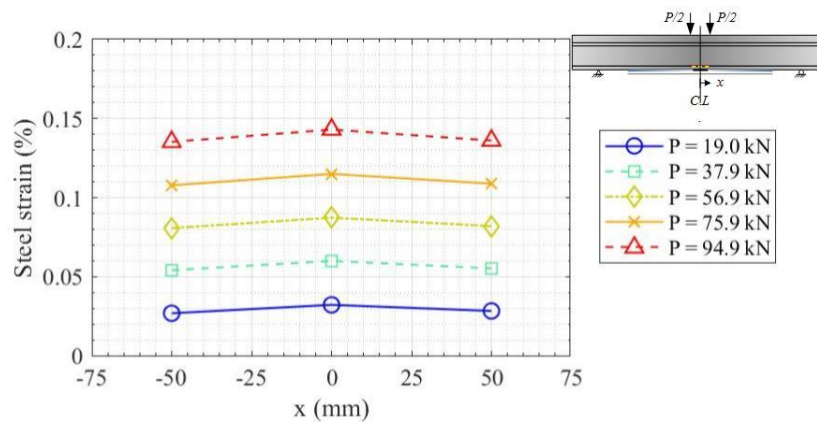


Figure B.35 Steel strain near midspan section of beam BMM120-0 (before yielding).

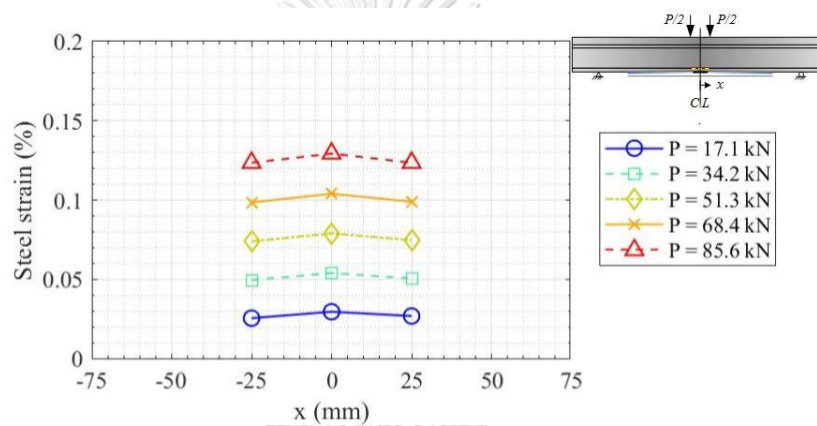


Figure B.36 Steel strain near midspan section of beam BMM120-50 (before yielding).

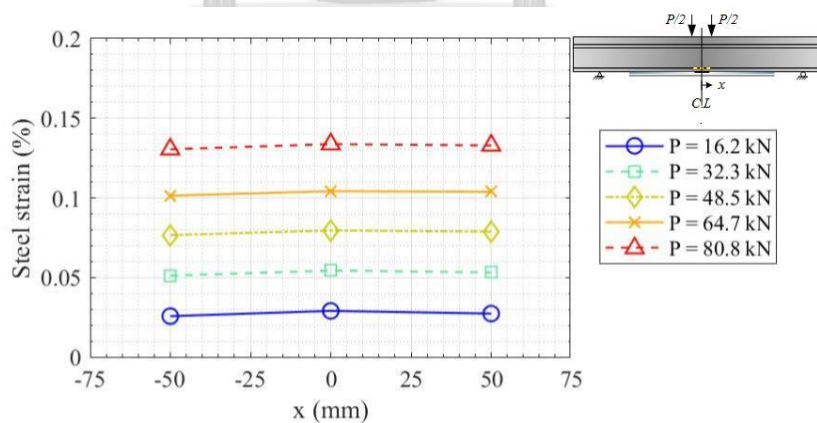


Figure B.37 Steel strain near midspan section of beam BMM120-100 (before yielding).

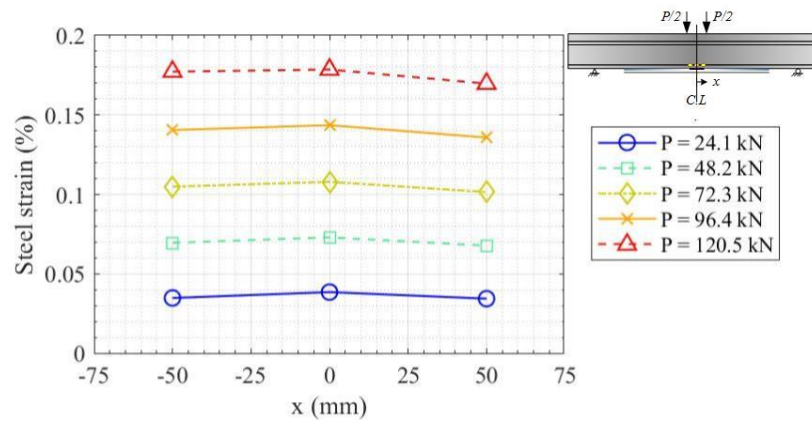


Figure B.38 Steel strain near midspan section of beam BMM120Y-100 (before yielding).

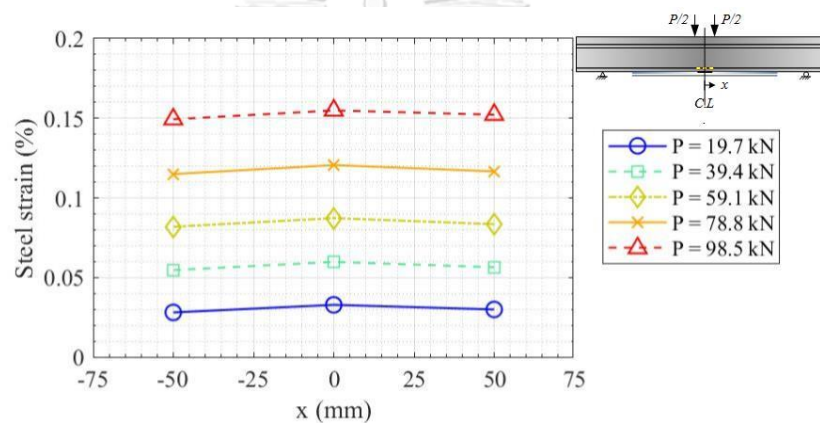


Figure B.39 Steel strain near midspan section of beam BMM150-100 (before yielding).

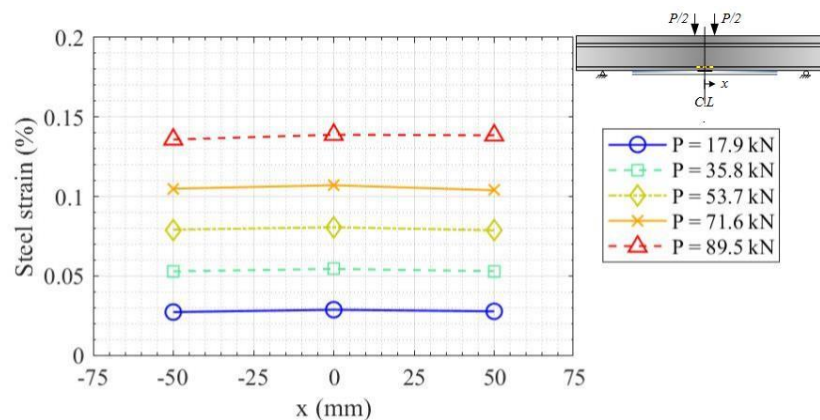


Figure B.40 Steel strain near midspan section of beam BSM120-0 (before yielding).

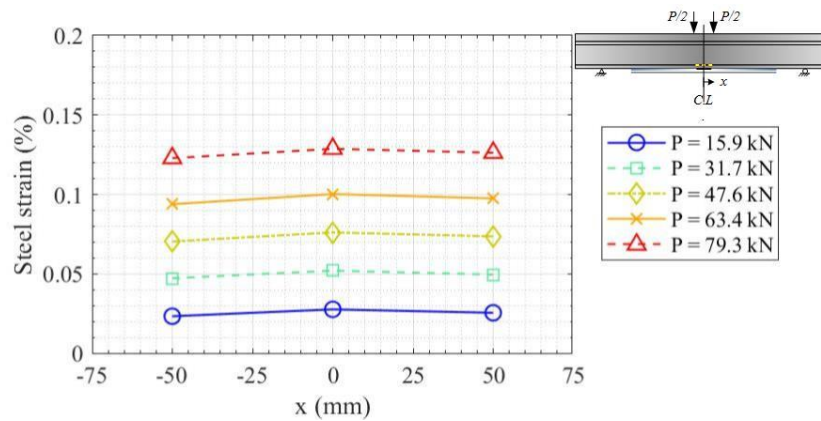


Figure B.41 Steel strain near midspan section of beam BSM120-100 (before yielding).

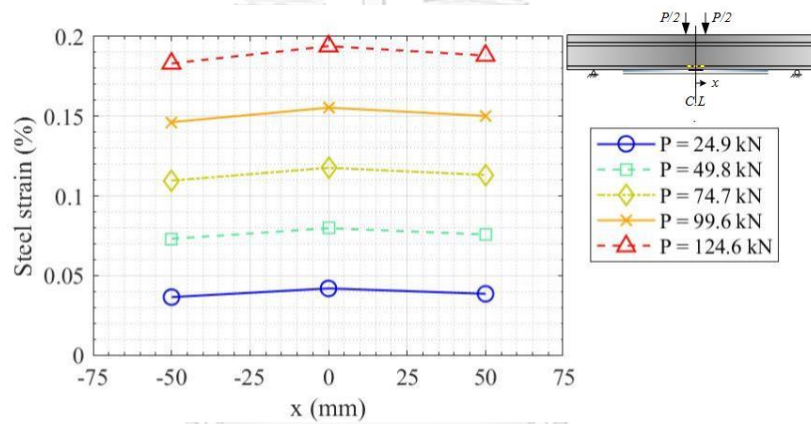


Figure B.42 Steel strain near midspan section of beam BSM120Y-100 (before yielding).

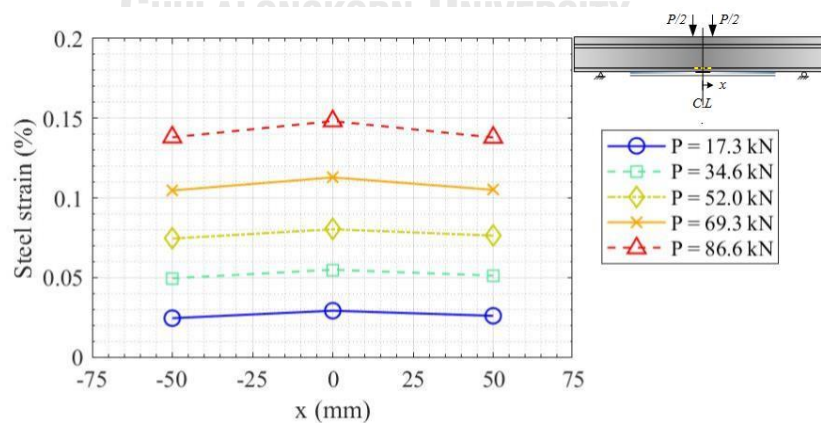


Figure B.43 Steel strain near midspan section of beam BSP120-100 (before yielding).

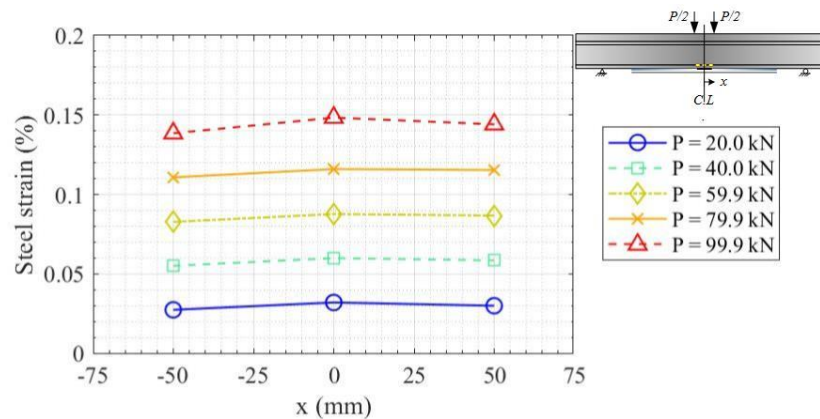


Figure B.44 Steel strain near midspan section of beam BMP120-100 (before yielding).

B.5 Strain Distributions at Steel Beams in Vicinity of Midspan Section (Between Yield and Maximum Loads)

Development of steel strains in vicinity of midspan section between the yielding state and the state that applied load reached the maximum value is plotted in Figure B.23 and Figure B.34. Applied load is separated into five levels. Each increment of load level is equal to 20% of the difference between yielding load and maximum load. The first load level is equal to the yielding load. The fifth load level is equal to the maximum load. It was found that strains of most beams were also aggressively increased at the maximum load level as observed in strain development over the midspan section.

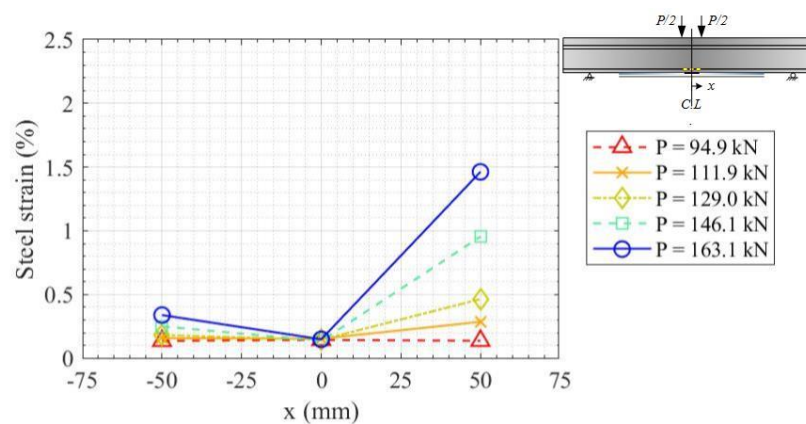


Figure B.45 Steel strain near midspan section of beam BMM120-0 (between yield and maximum load).

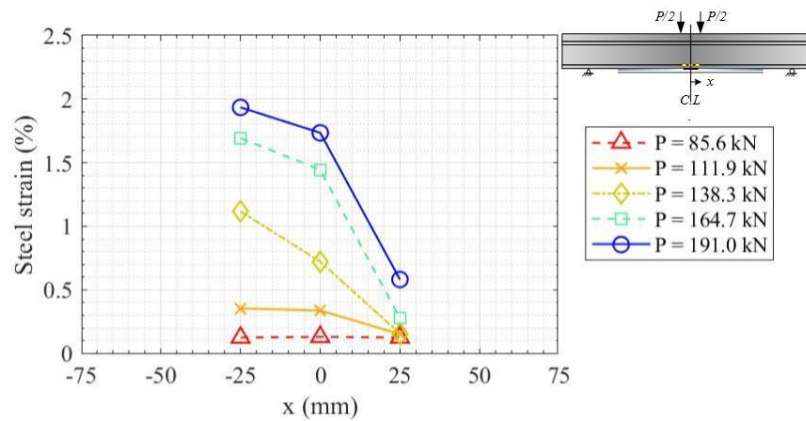


Figure B.46 Steel strain near midspan section of beam BMM120-50 (between yield and maximum load).

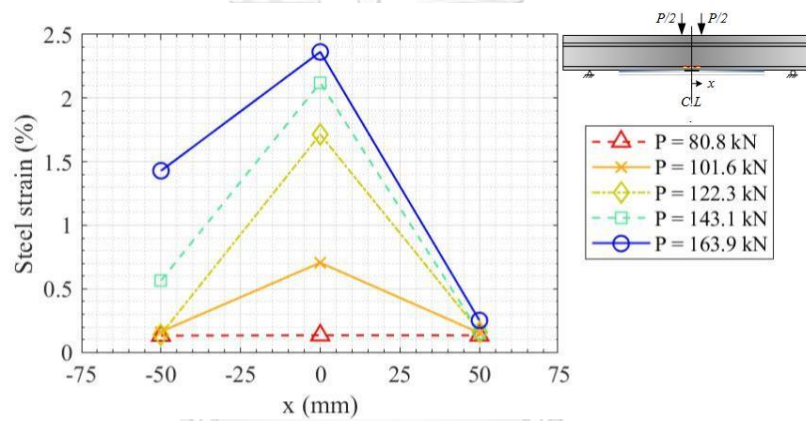


Figure B.47 Steel strain near midspan section of beam BMM120-100 (between yield and maximum load).

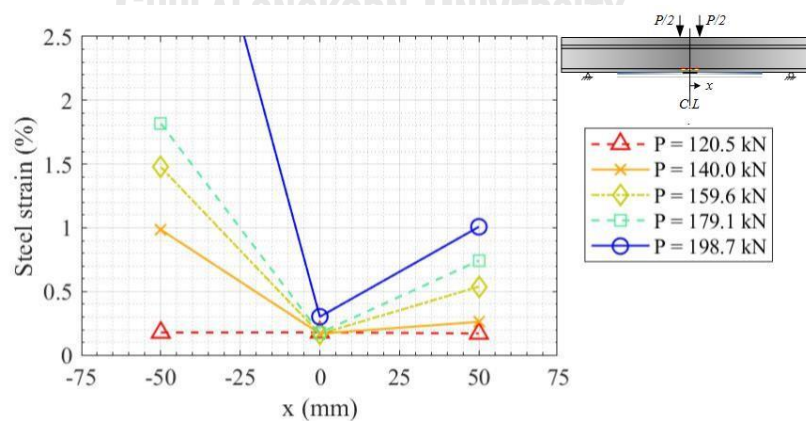


Figure B.48 Steel strain near midspan section of beam BMM120Y-100 (between yield and maximum load).

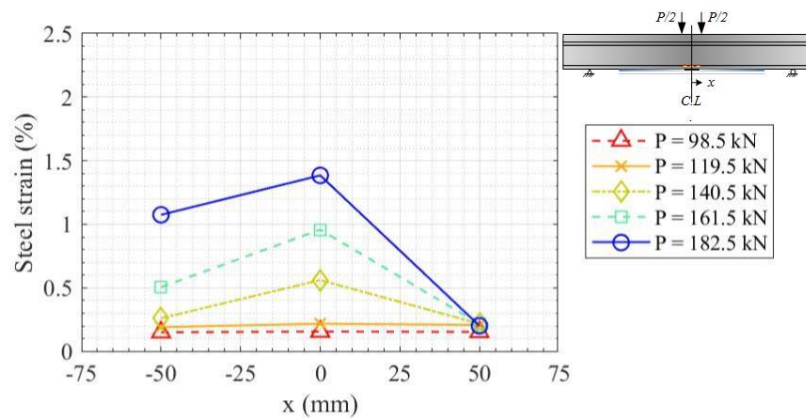


Figure B.49 Steel strain near midspan section of beam BMM150-100 (between yield and maximum load).

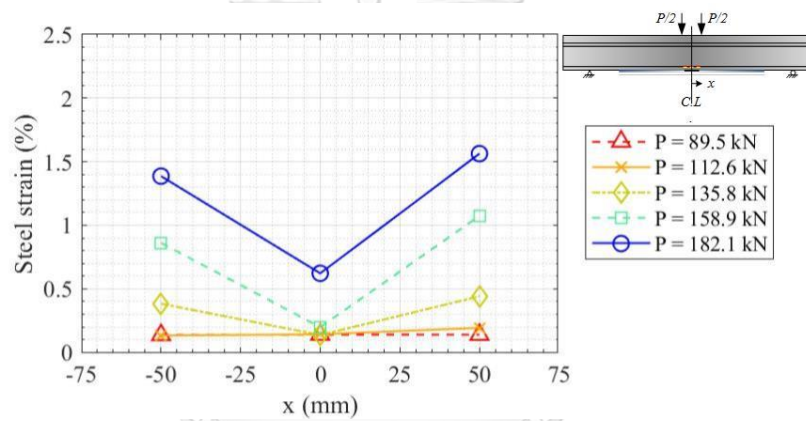


Figure B.50 Steel strain near midspan section of beam BSM120-0 (between yield and maximum load).

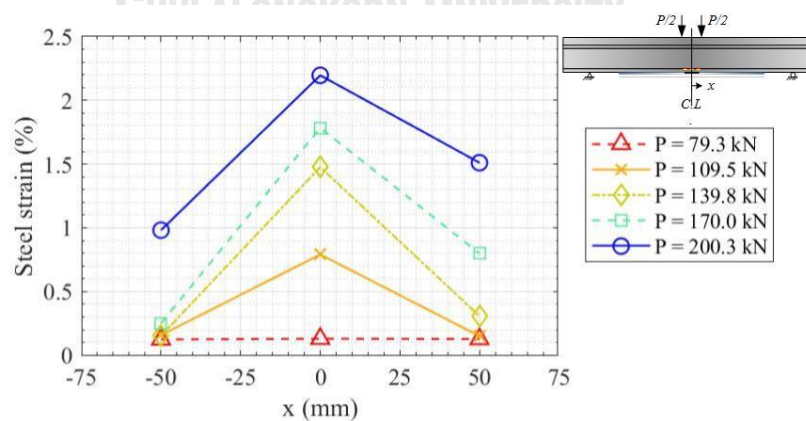


Figure B.51 Steel strain near midspan section of beam BSM120-100 (between yield and maximum load).

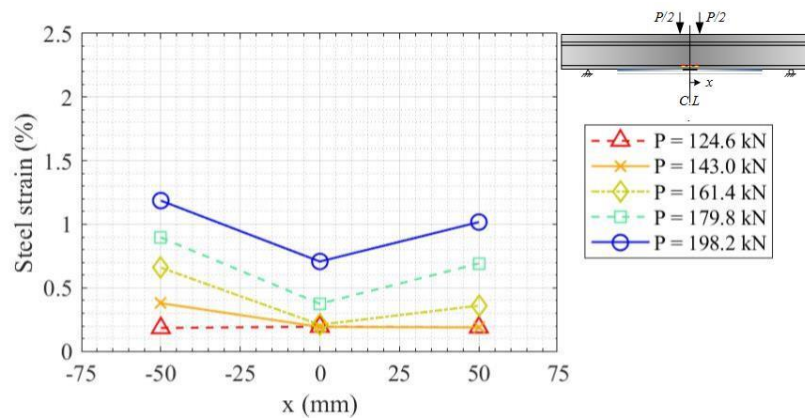


Figure B.52 Steel strain near midspan section of beam BSM120Y-100 (between yield and maximum load).

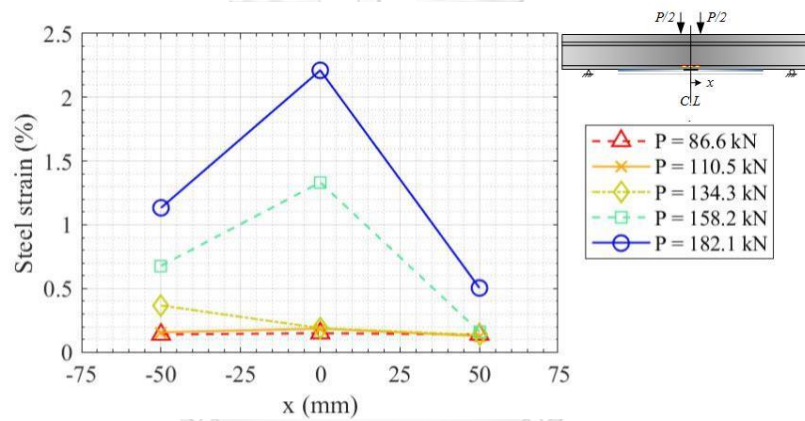


Figure B.53 Steel strain near midspan section of beam BSP120-100 (between yield and maximum load).

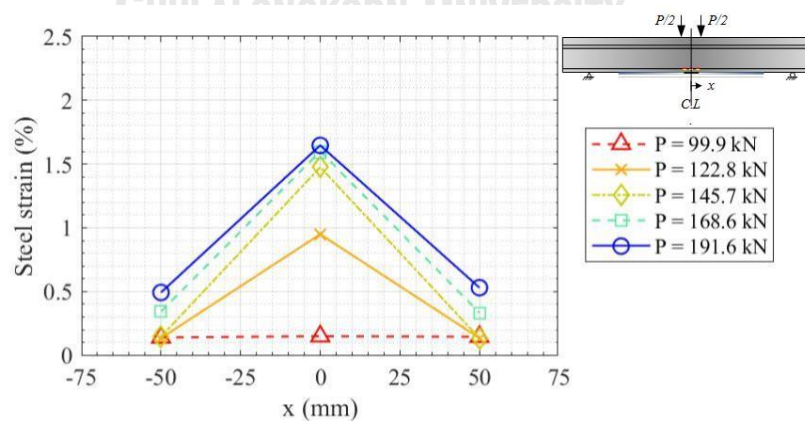


Figure B.54 Steel strain near midspan section of beam BMP120-100 (between yield and maximum load).

B.6 Strain Distributions Along FRP Plates (Before Yielding)

Development of strain along the FRP plates before the yielding state is plotted in Figure B.55 to Figure B.64. Applied load is separated into five levels. Each increment of load level is equal to 20% of yielding load. The fifth load level is equal to the yielding load. It was found that strain at bottom surface of top flange is usually more than strain at top surface of the cover plate. The light gray-shaded area indicates the constant moment region. It is found that strain level in constant moment zone cannot produce an exactly identical strain level as discussed in section 5.5. Unusual strain signal at -200 mm from midspan section is detected in beam BSM120Y-100. Strain at this point is aggressively increased and dropped to the usual value. This phenomenon cannot be implied and needs to be examined such strange situation in future works.

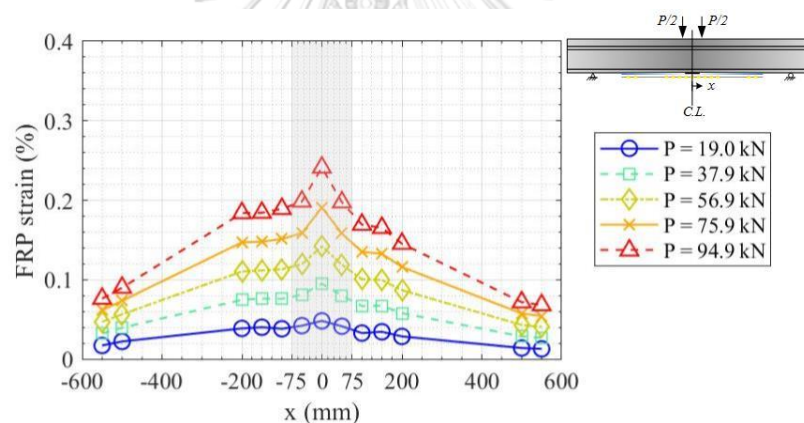


Figure B.55 FRP strain of beam BMM120-0 (before yielding).

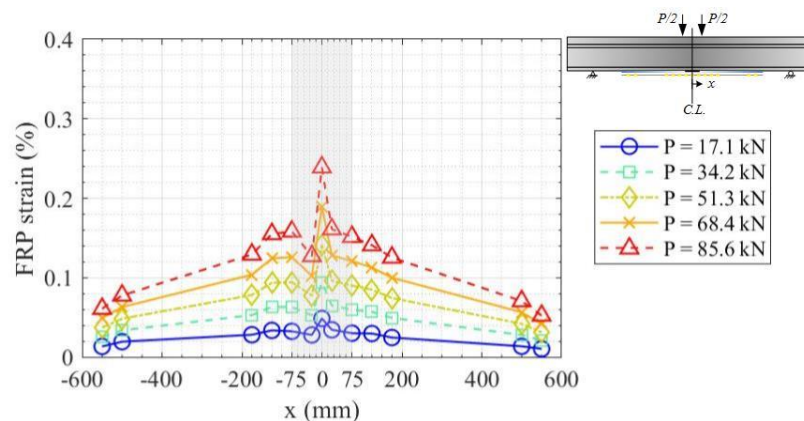


Figure B.56 FRP strain of beam BMM120-50 (before yielding).

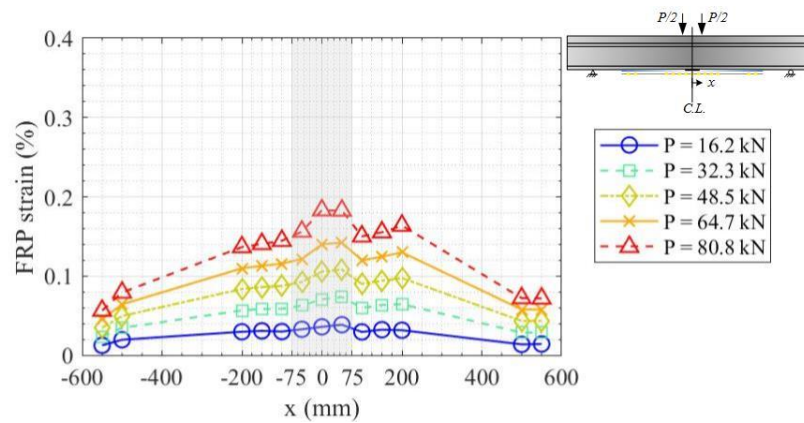


Figure B.57 FRP strain of beam BMM120-100 (before yielding).

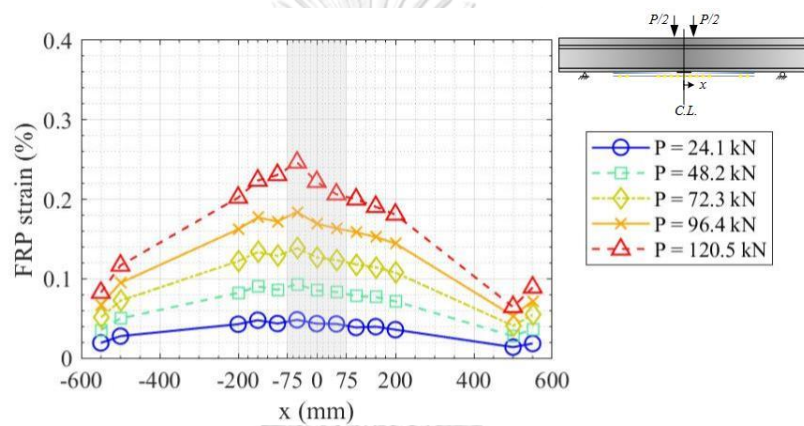


Figure B.58 FRP strain of beam BMM120Y-100 (before yielding).

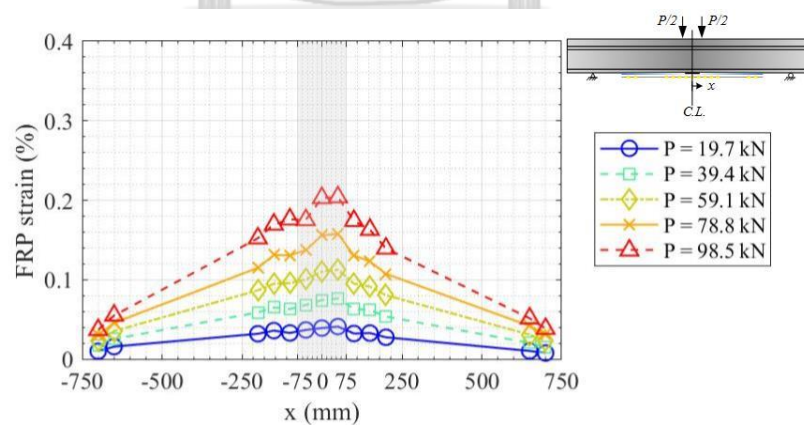


Figure B.59 FRP strain of beam BMM150-100 (before yielding).

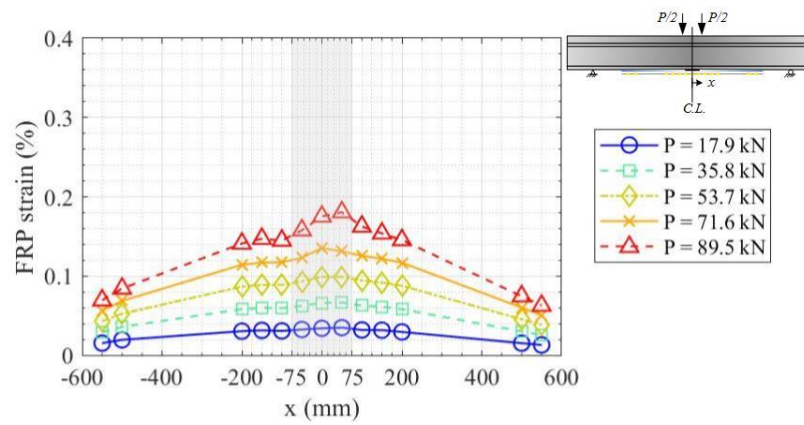


Figure B.60 FRP strain of beam BSM120-0 (before yielding).

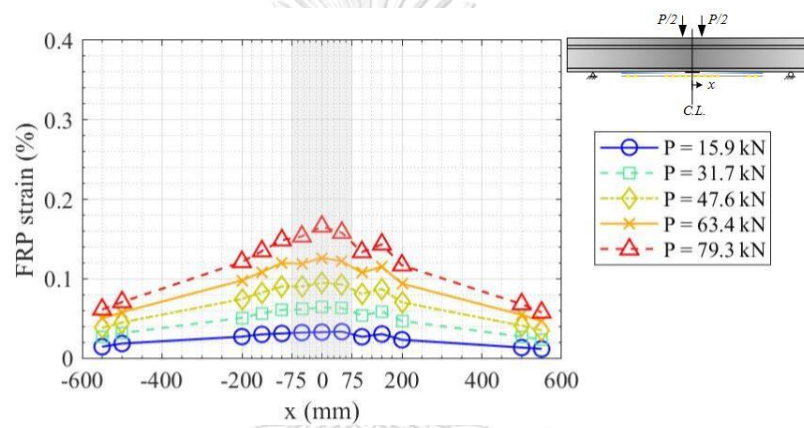


Figure B.61 FRP strain of beam BSM120-100 (before yielding).

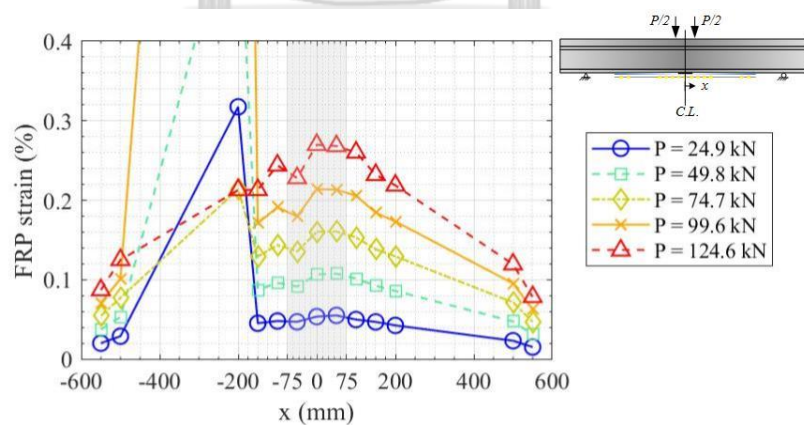


Figure B.62 FRP strain of beam BSM120Y-100 (before yielding).

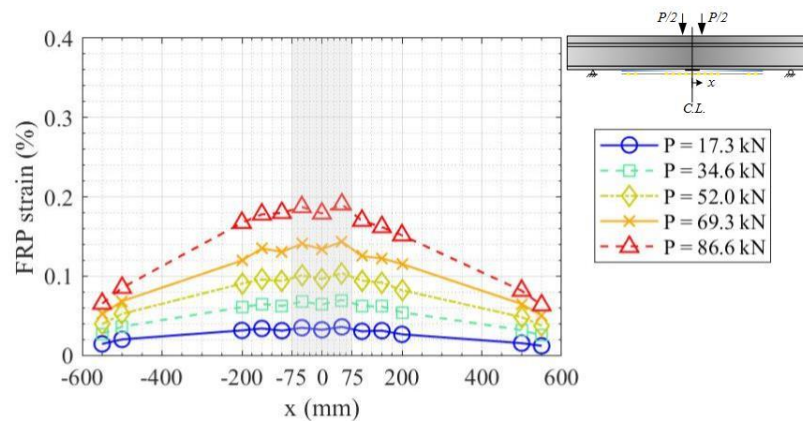


Figure B.63 FRP strain of beam BSP120-100 (before yielding).

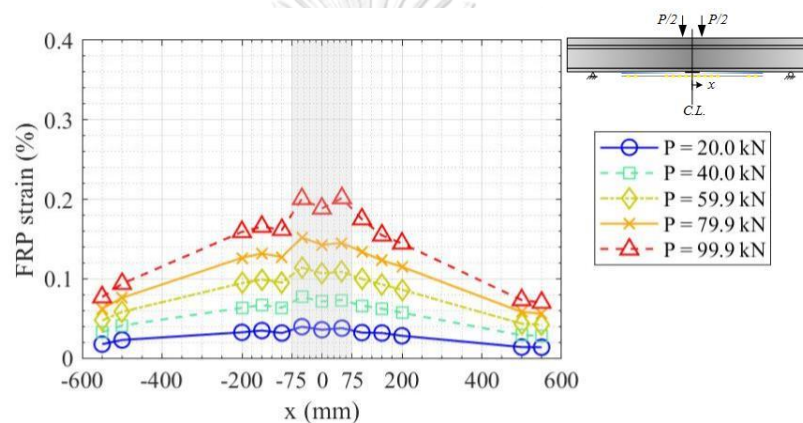


Figure B.64 FRP strain of beam BMP120-100 (before yielding).

B.7 Strain Distributions Along FRP Plates (Between Yield and Maximum Loads)

Development of strain along the FRP plates between the yielding state and the state that applied load reached the maximum value is plotted in Figure B.65 and Figure B.74. Applied load is separated into five levels. Each increment of load level is equal to 20% of the difference between yielding load and maximum load. The first load level is equal to the yielding load. The fifth load level is equal to the maximum load. It was found that FRP strains of all beams were significantly increased at the maximum load level. The limited value of 1% and 1.8% is the tensile strain obtained from FRP plate coupons. This limited value is used to cut off the excessive strain value due to strain gage failure for the appropriated graph plotting. The signal at limited value is supposed to be local fiber situation. The significantly decreasing of

strain signal is assumed that FRP at that point may debond from steel beam. It is worth noting that local fiber rupture is occurred in all beams at maximum applied load. Local intermediate debonding is also occurred in most beams except for beam BMM150-100 and BSP120-100. This is one of an advantage of strain gage installation over digital image correlation. Local fiber rupture and microscopic intermediate debonding of FRP plates may not easily detected by using image analysis.

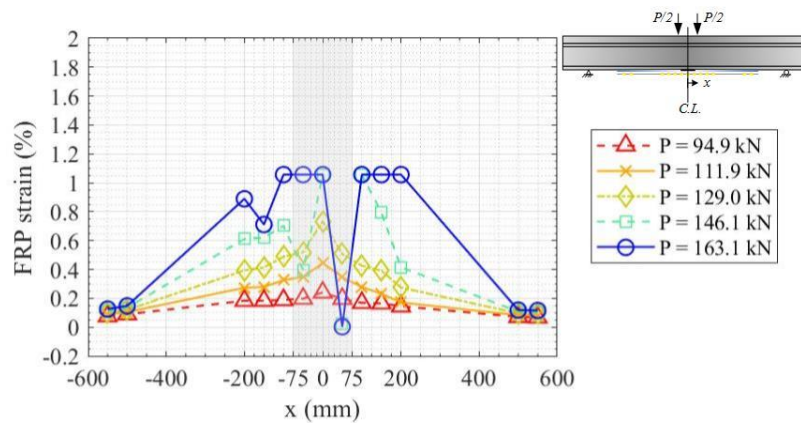


Figure B.65 FRP strain of beam BMM120-0 (between yield and maximum load).

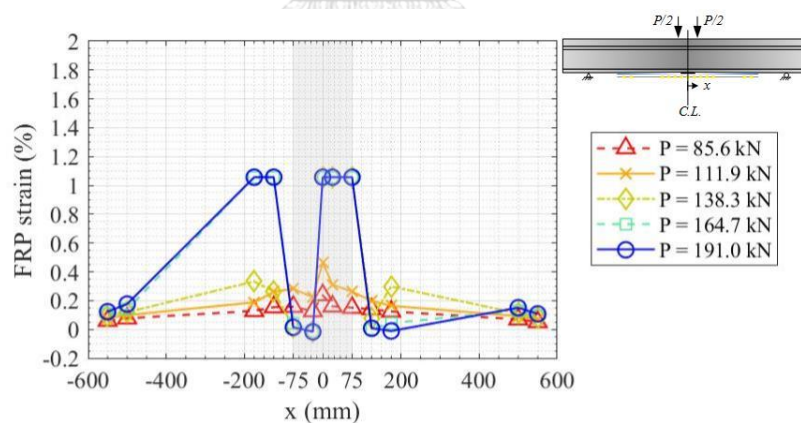


Figure B.66 FRP strain of beam BMM120-50 (between yield and maximum load).

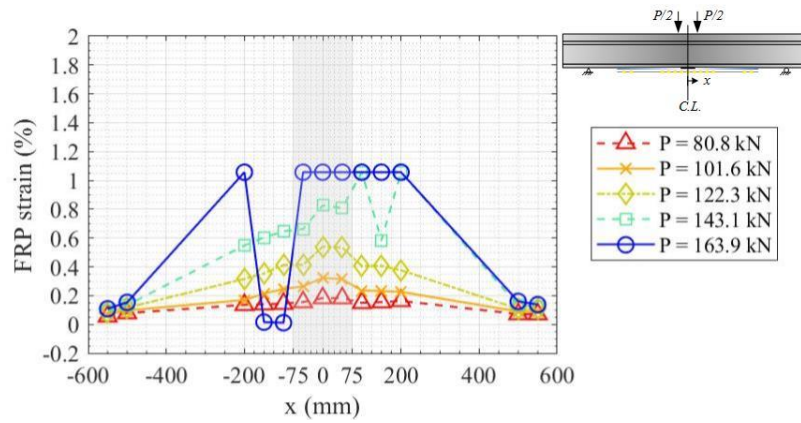


Figure B.67 FRP strain of beam BMM120-100 (between yield and maximum load).

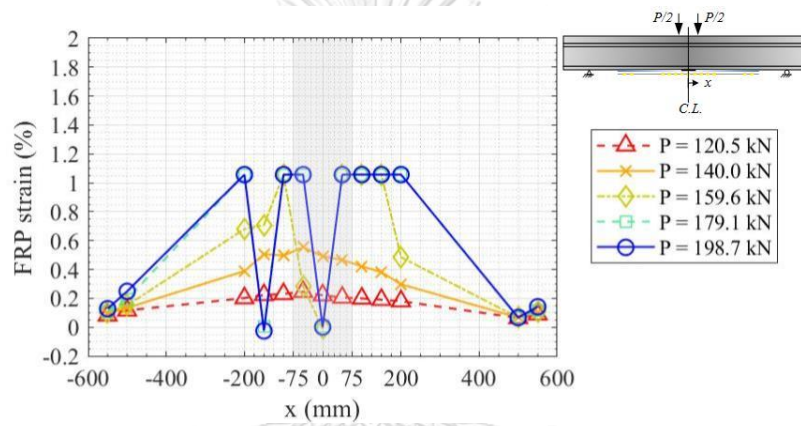


Figure B.68 FRP strain of beam BMM120Y-100 (between yield and maximum load).

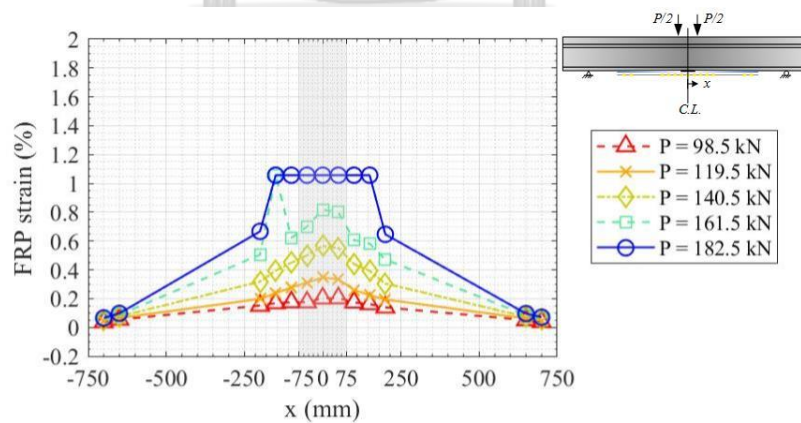


Figure B.69 FRP strain of beam BMM150-100 (between yield and maximum load).

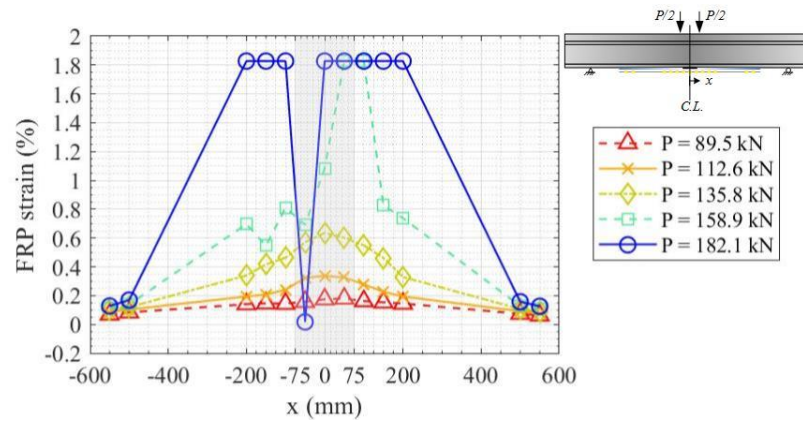


Figure B.70 FRP strain of beam BSM120-0 (between yield and maximum load).

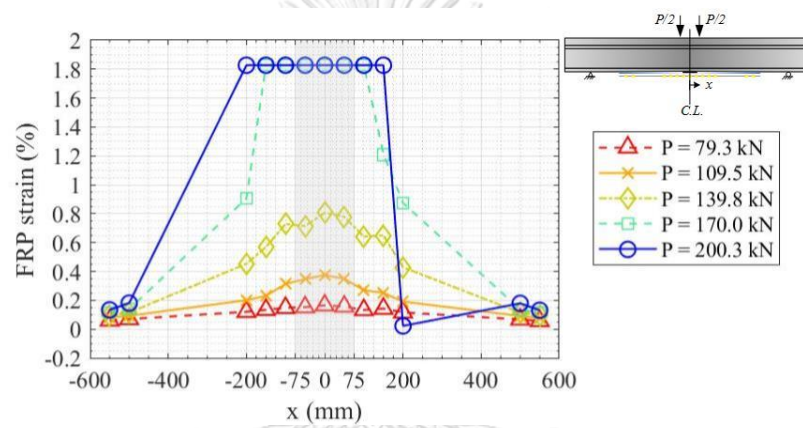


Figure B.71 FRP strain of beam BSM120-100 (between yield and maximum load).

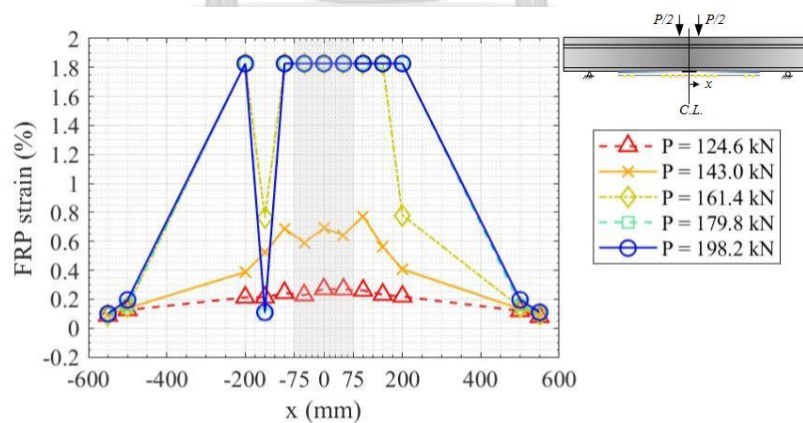


Figure B.72 FRP strain of beam BSM120Y-100 (between yield and maximum load).

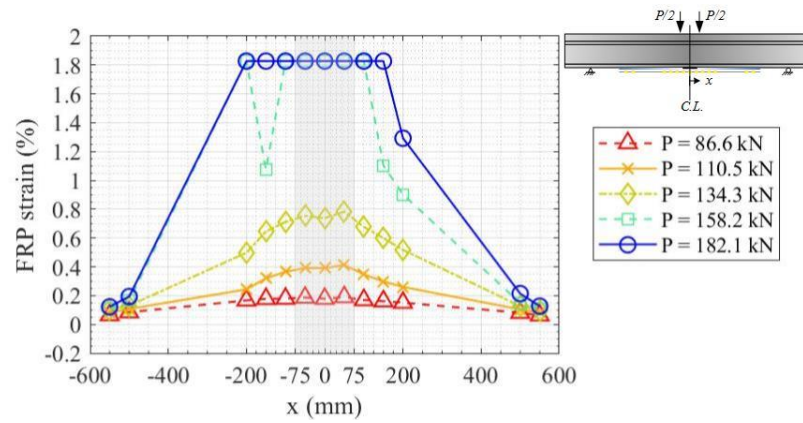


Figure B.73 FRP strain of beam BSP120-100 (between yield and maximum load).

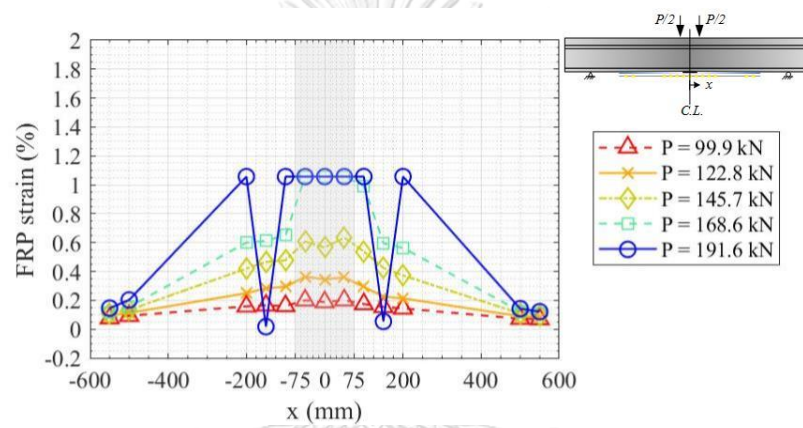


Figure B.74 FRP strain of beam BMP120-100 (between yield and maximum load).

APPENDIX C

POST-PEAK BEHAVIOR OF MONOTONIC TESTED BEAMS

Strain gage signals after an applied load reaches the maximum value are presented in this appendix to examine the flexural behavior in detail. Section C.1 discusses the flexural properties of beams at post-peak of applied load. Load-deflection curves of beams are also presented. All strain gages installed at the midspan section are presented in section C.2 to observe strain distribution across midspan section. The integrity of the yielding zone within the constant moment region is focused in section C.3 by plotting all strains attached on the bottom surface of bottom flange. FRP strain distribution when an applied load increased is also investigated through section C.4.

C.1 Load-Deflection Curves

Flexural properties of FRP-strengthened beams are tabulated in Table C.1. t_{post} denotes the time that beam can resist the applied load before the global failure due to FRP rupture or debonding occurred. It is worth noting that beam without initial bond defect has not much time before the global failure is existed. The presence of initial bond defect may reduce the brittle behavior of FRP-strengthened beams as much as it could be. For the beam with predamage application, the time before global failure is significantly increased, especially beam BMM120Y-100. Unlike beam BSM120Y-100, the time before global failure is less compared to beam BSM120-100. This may cause by the less difference of elastic modulus between steel and FRP plate. Level of predamage may affect this issue as well. Future research should examine the effects of FRP modulus and predamage level on post-peak behavior of FRP-strengthened steel beams.

Load-deflection curves of monotonic tested beams with softening branch are plotted as shown in Figure C.1 to Figure C.4. Beam without initial bond defect shows that the use of higher FRP modulus cannot observe the softening branch. In case of the presence of initial bond defect, the softening branch is easily observed. For the

beam using Sika® CarboDur® S512, the presence of initial bond defect shows the softening branch more clearly than beam BSM120-0.

Table C.1 Post-peak properties of strengthened beams.

Beam	Δ_{max} (mm)	P_{max} (kN)	Δ_{post} (mm)	P_{post} (kN)	Post-peak stiffness deterioration (kN/m)	t_{post} (sec)
BMM120-0	14.64	163.5	16.70	120.6	20,757	1.22
BMM120-50	18.76	191.4	19.95	122.1	58,527	7.69
BMM120-100	17.39	164.1	18.84	105.1	40,931	3.33
BMM120Y-100	24.51	199.0	26.55	115.9	40,791	46.85
BMM150-100	16.41	182.9	16.96	130.2	95,149	6.4
BSM120-0	23.59	182.4	23.63	181.3	24,865	1.99
BSM120-100	33.53	200.7	36.43	155.3	15,664	15.77
BSM120Y-100	28.92	198.5	29.88	174.1	25,429	11.15

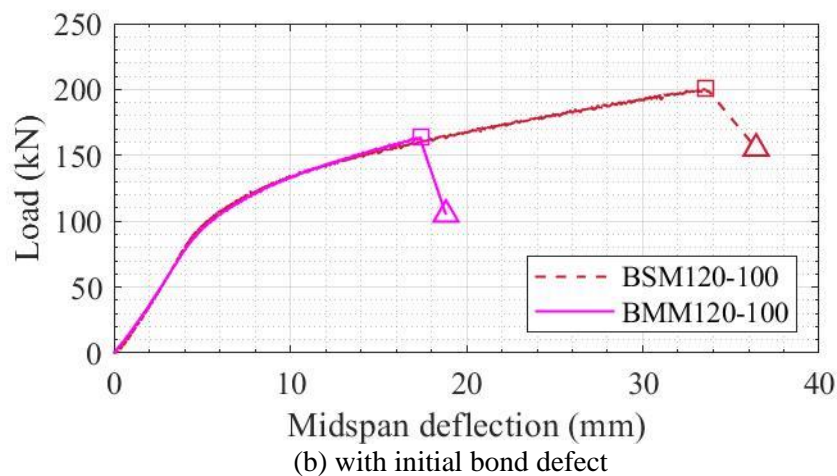
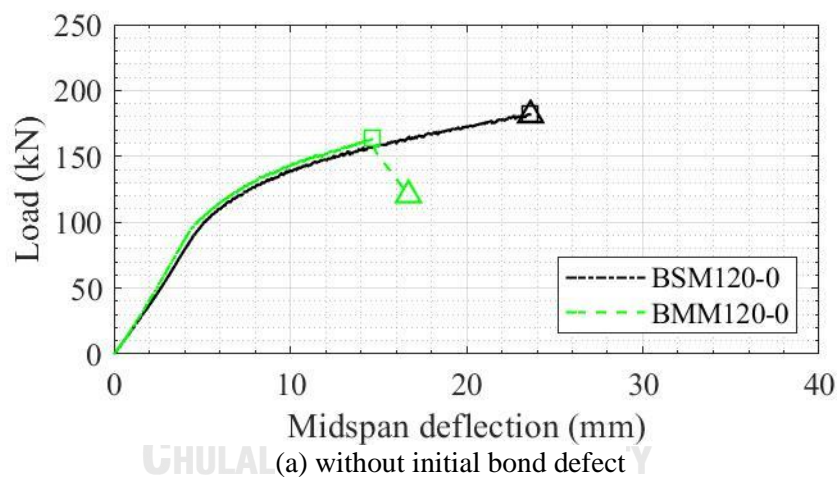


Figure C.1 Effect of FRP modulus on post-peak load-deflection curve.

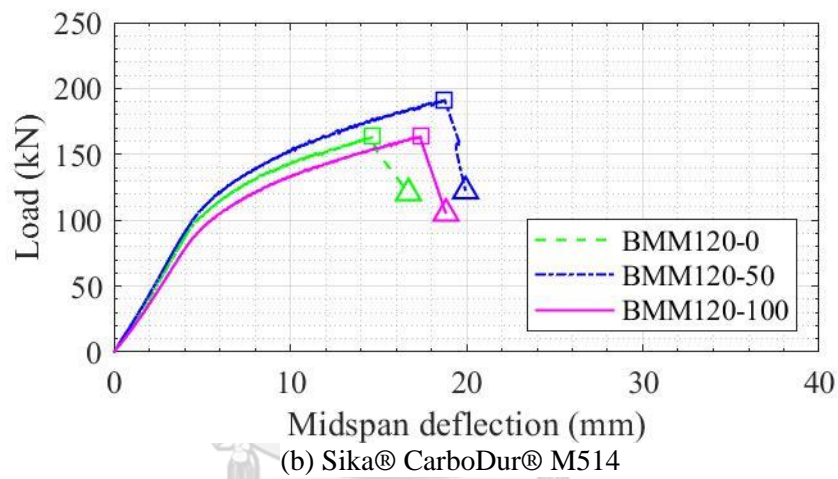
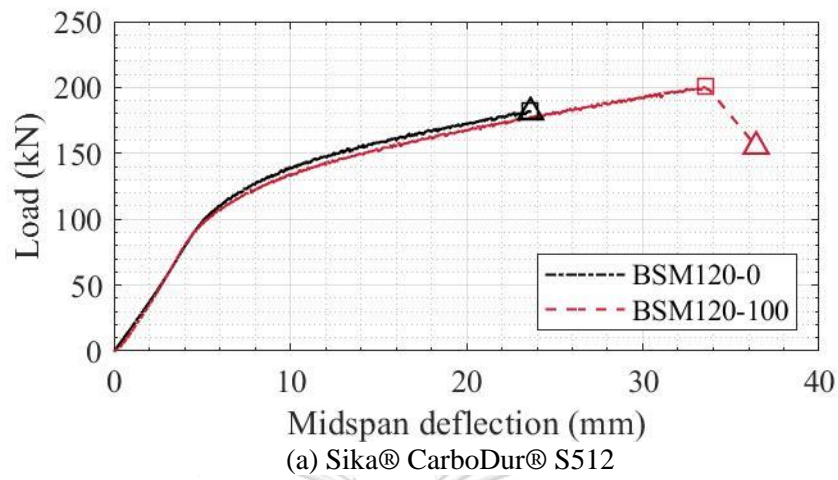


Figure C.2 Effect of initial bond defect on post-peak load-deflection curve.

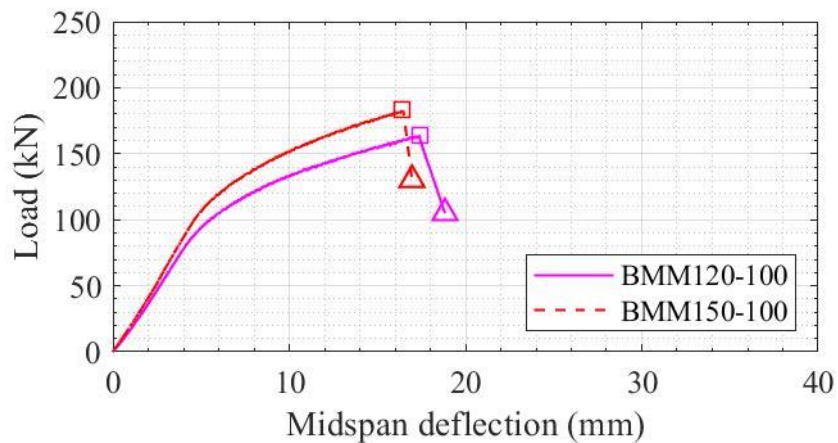


Figure C.3 Effect of FRP bond length on post-peak load-deflection curve.

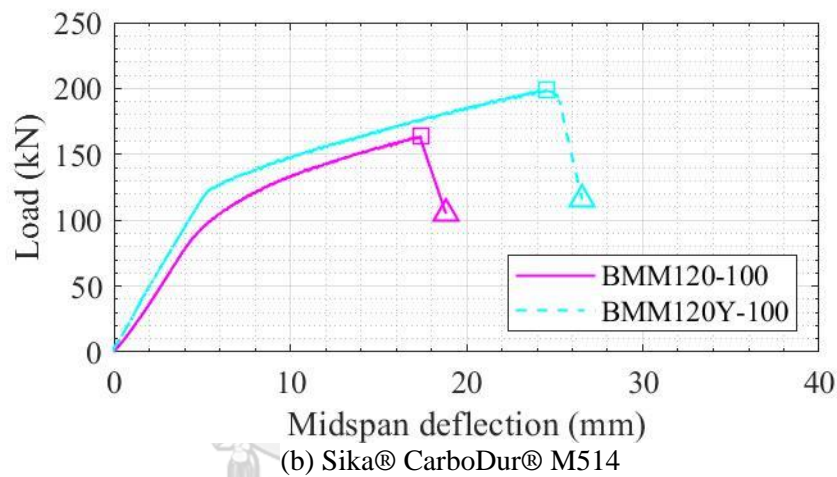
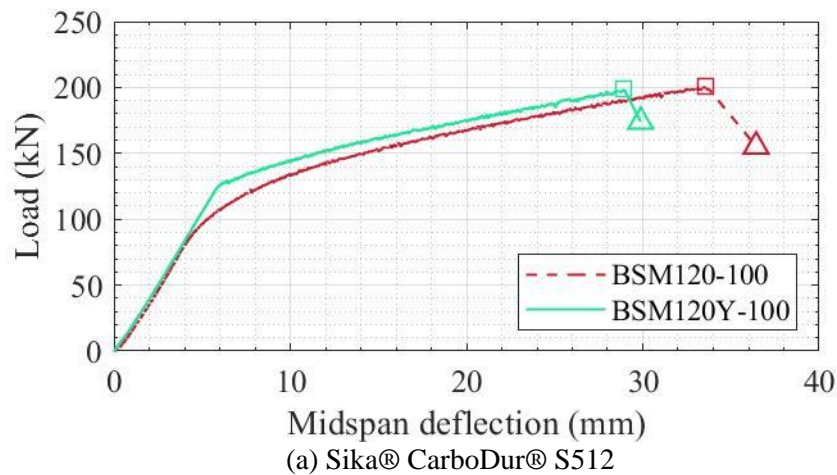


Figure C.4 Effect of predamage on post-peak load-deflection curve.

C.2 Strain Distribution at Midspan Section

Before sudden failure of FRP plate has occurred, all steel strains were recorded and can be tabulated in Table C.2. Steel strains in beam BMM120-0 and BSM120-0 were not changed compared to the state that applied load reached the maximum value. Beam without initial bond defect shows the brittle behavior, which is strain in steel are not allowed to increase before failure. At maximum recordable midspan deflection, beam BMM120Y-100 is the most increase in value of strain at top surface of bottom flange compared to the corresponding strain at maximum load. This use of FRP modulus and predamage level may be suitable for allowing the large increasing of strain after applied load beyond the maximum value.

Table C.2 Steel strains of FRP-strengthened beams at maximum recordable midspan deflection.

Beam	Steel strain normalized by coupon yield strain			
	Top surface of the bottom flange	Midweb	Bottom surface of the top flange	Top surface of the cover plate
BMM120-0	0.73	1.15	-0.10	-0.53
BMM120-50	8.72	1.66	0.15	-0.50
BMM120-100	11.65	3.79	-0.02	-0.33
BMM120Y-100	3.10	3.22	0.05	-0.53
BMM150-100	7.68	1.17	-0.04	-0.41
BMP120-100	8.23	1.27	0.02	-0.31
BSM120-0	3.07	3.55	0.09	-0.49
BSM120-100	12.69	3.44	0.20	-0.63
BSM120Y-100	3.52	1.12	0.12	-0.54
BSP120-100	10.99	1.10	0.04	-0.63

Strain distributions over the midspan section at the maximum recordable value of midspan deflection are plotted in Figure C.5 to Figure C.12. Most beams with an initial bond defect show the significantly increased in steel strains before catastrophic failure of FRP plate take places. Strains in beam BSM120Y-100 is not quite changed before failure. This research believes that the use of FRP modulus, predamage level, and initial bond defect length affect strain distribution before failure.

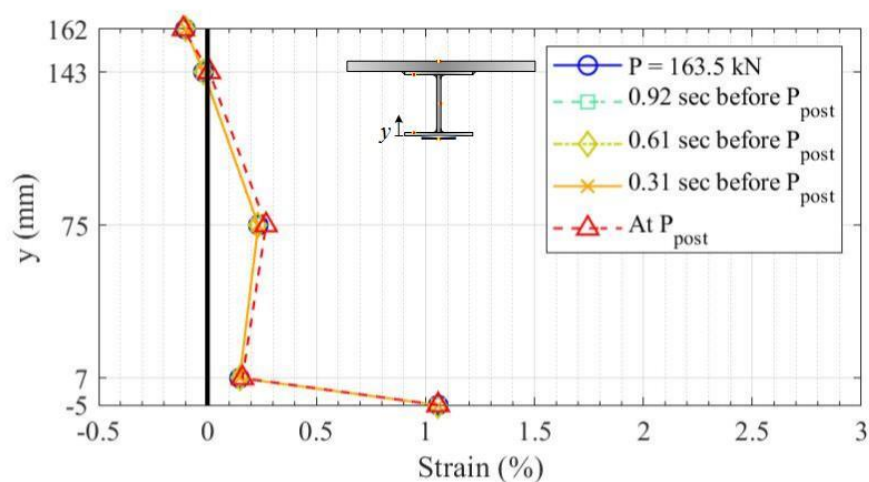


Figure C.5 Post-peak strain at midspan section of beam BMM120-0.

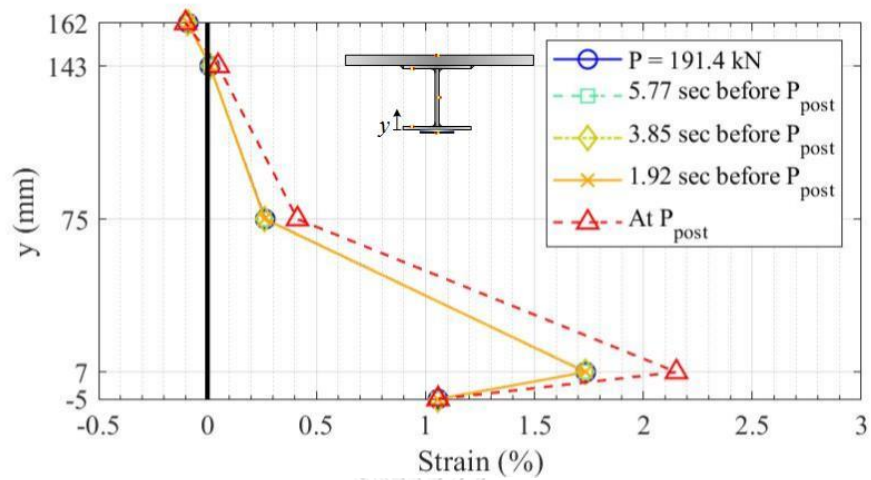


Figure C.6 Post-peak strain at midspan section of beam BMM120-50.

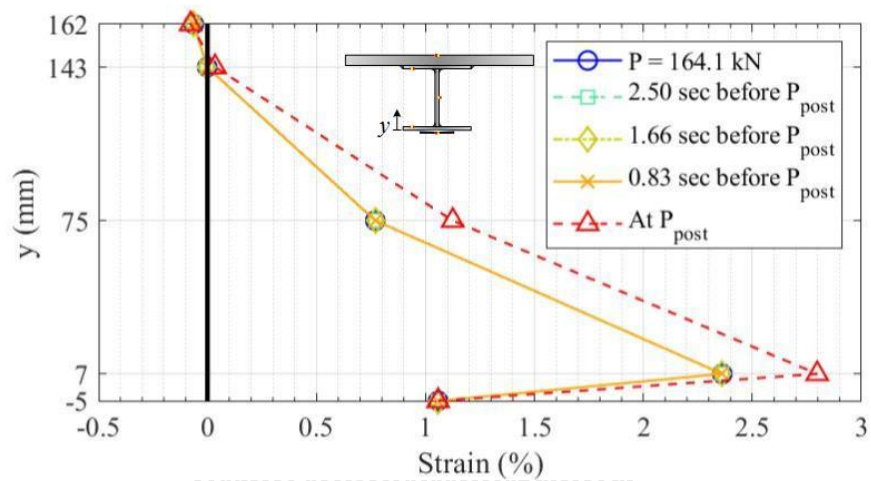


Figure C.7 Post-peak strain at midspan section of beam BMM120-100.

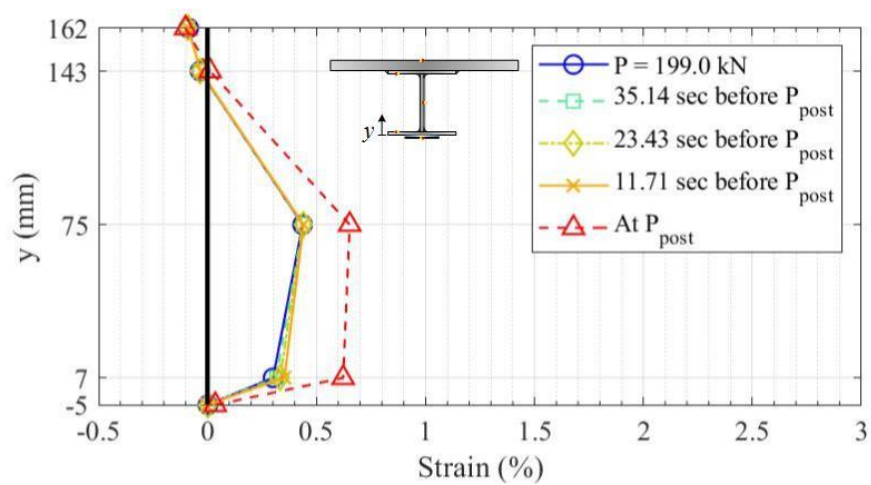


Figure C.8 Post-peak strain at midspan section of beam BMM120Y-100.

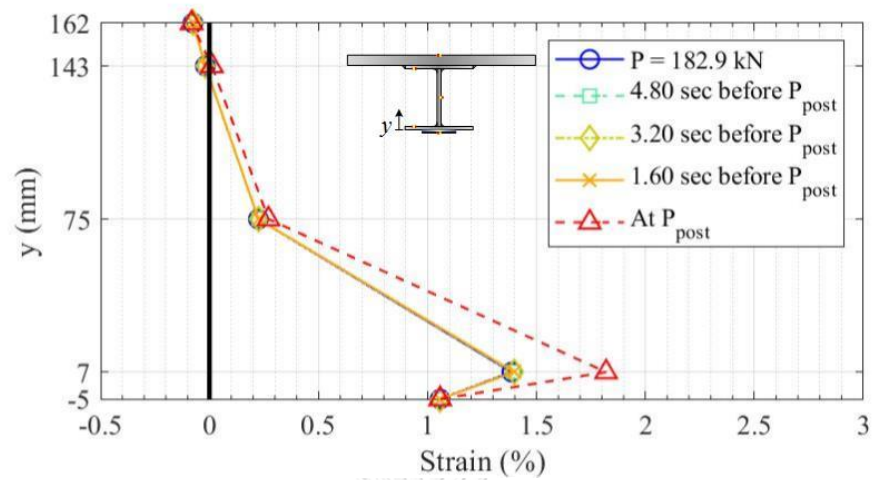


Figure C.9 Post-peak strain at midspan section of beam BMM150-100.

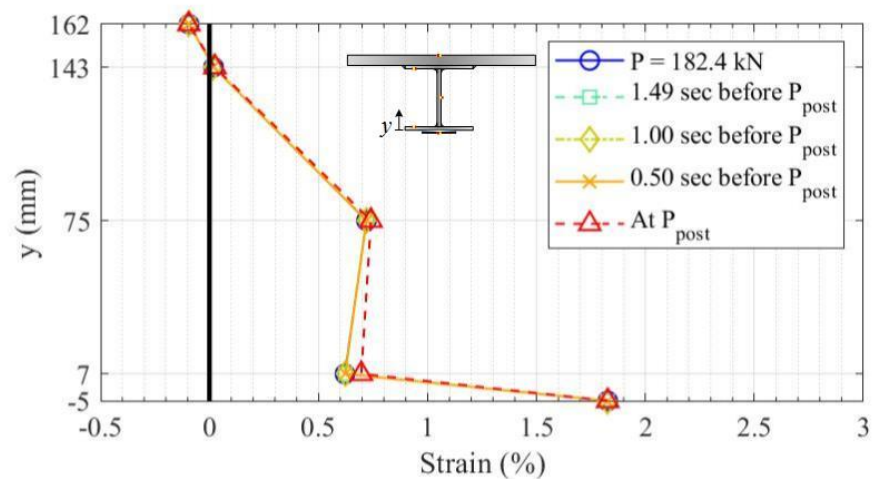


Figure C.10 Post-peak strain at midspan section of beam BSM120-0.

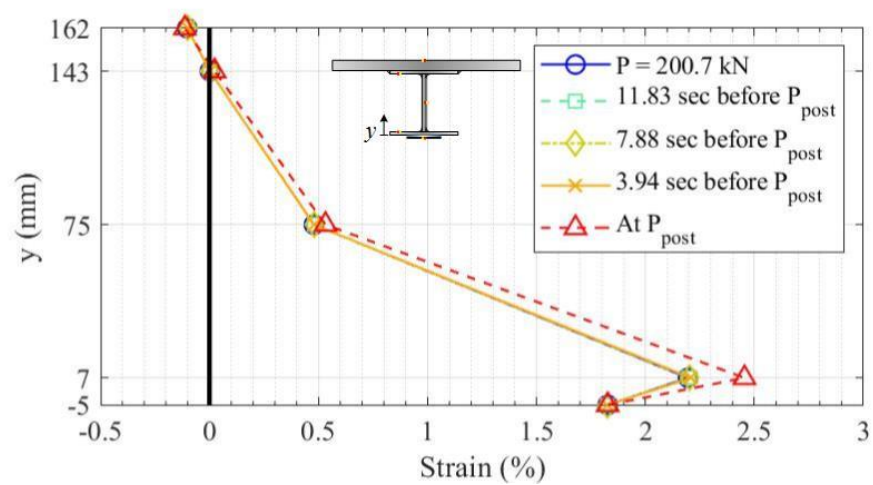


Figure C.11 Post-peak strain at midspan section of beam BSM120-100.

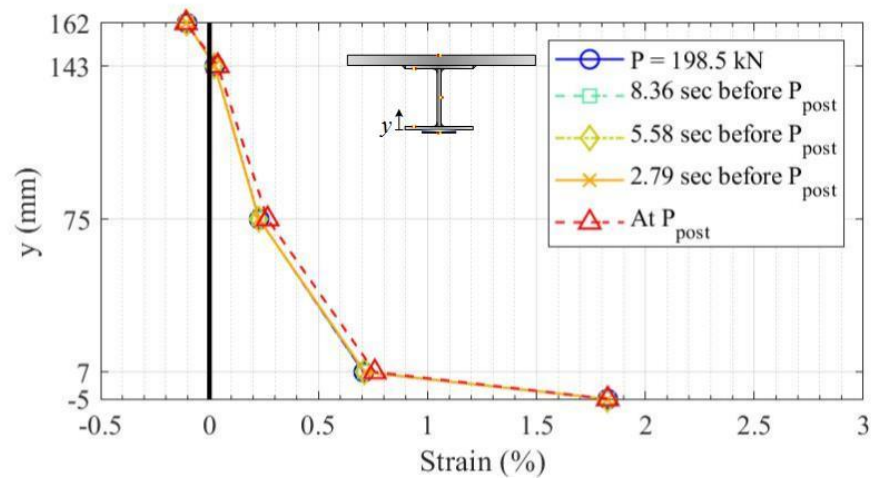


Figure C.12 Post-peak strain at midspan section of beam BSM120Y-100.

C.3 Strain Distributions of Steel in Vicinity of Midspan Section

In the post-peak region of the load-deflection curve, the development of strain in vicinity of midspan section in constant moment region is plotted in Figure C.13 to Figure C.20. It is found that all beams show non-uniform yielding even though the measured points are lie in the constant moment zone. There is the failure of strain gage affixed in beam BMM120Y-100 and BSM120-100. The strain gage in BMM120Y-100 started to fail at maximum load. The strain gage in BSM120-100 started to fail before catastrophic failure of FRP plate took places. This research anticipates that the occurrence of local intermediate debonding of FRP plate for these two beams may induce some vibration or shocking. This vibration or shocking may break the strain gage wire.

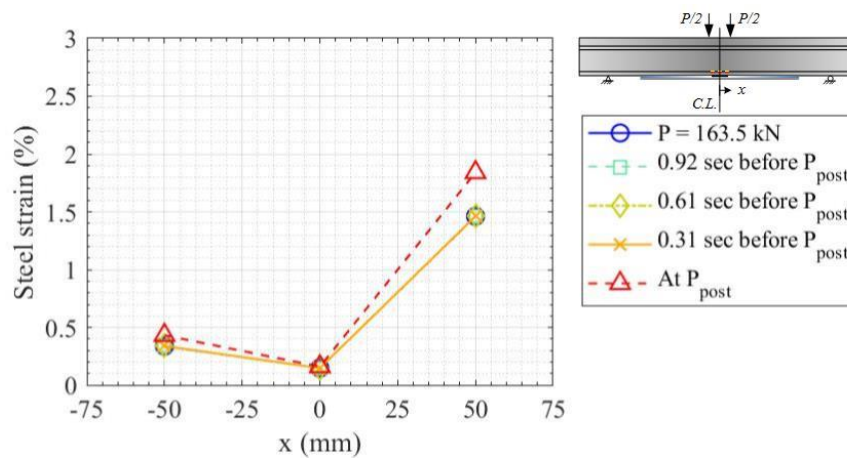


Figure C.13 Post-peak steel strain near the midspan section of beam BMM120-0.

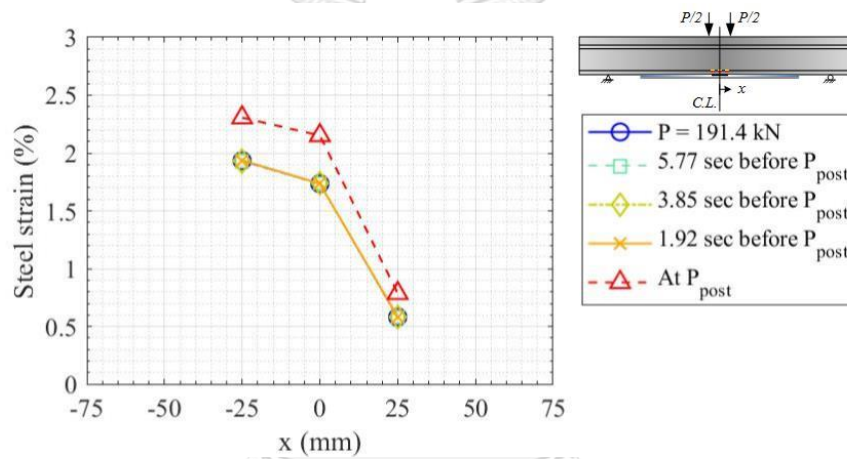


Figure C.14 Post-peak steel strain near the midspan section of beam BMM120-50.

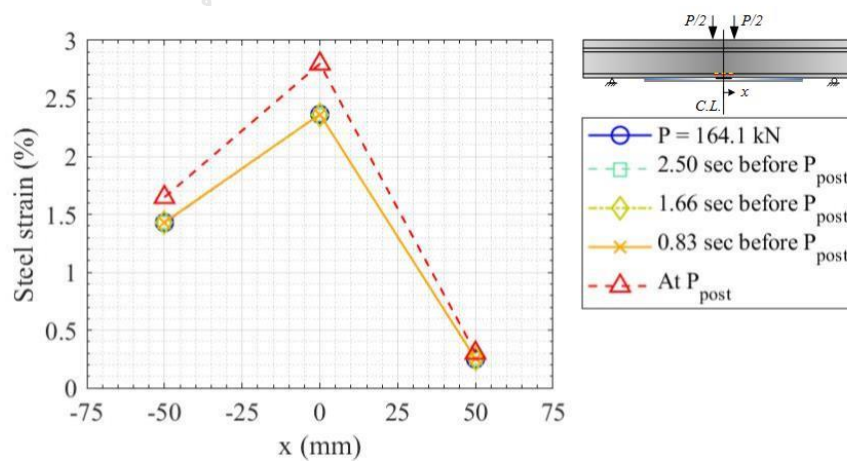


Figure C.15 Post-peak steel strain near the midspan section of beam BMM120-100.

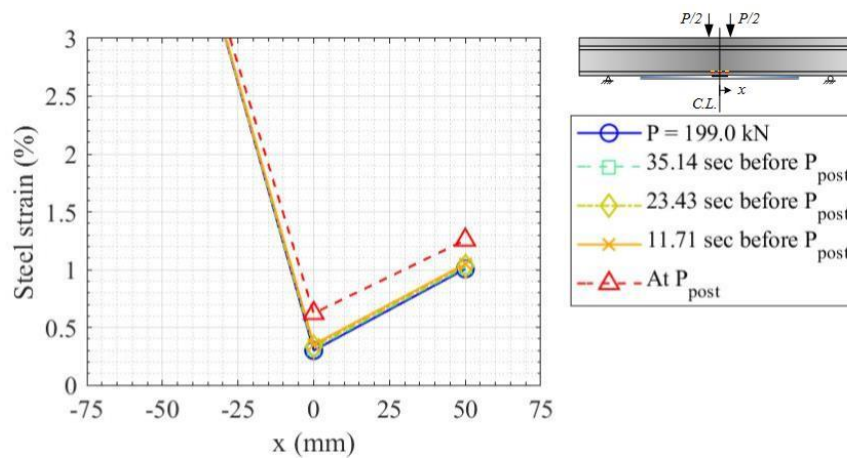


Figure C.16 Post-peak steel strain near the midspan section of beam BMM120Y-100.

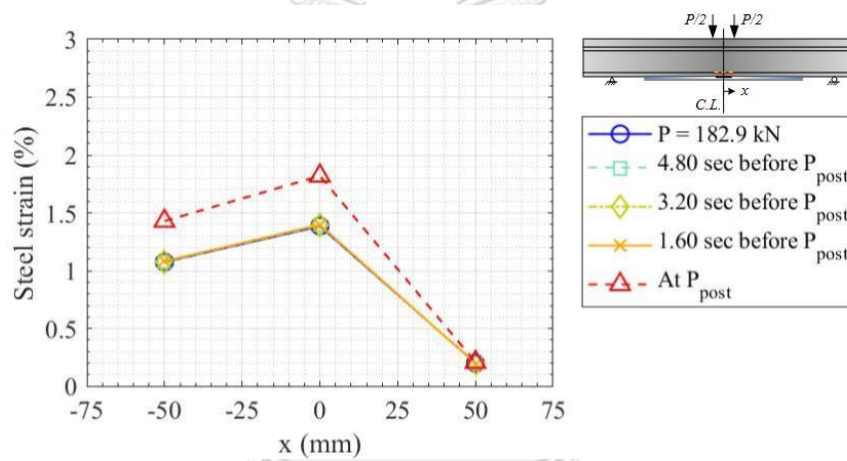


Figure C.17 Post-peak steel strain near the midspan section of beam BMM150-100.

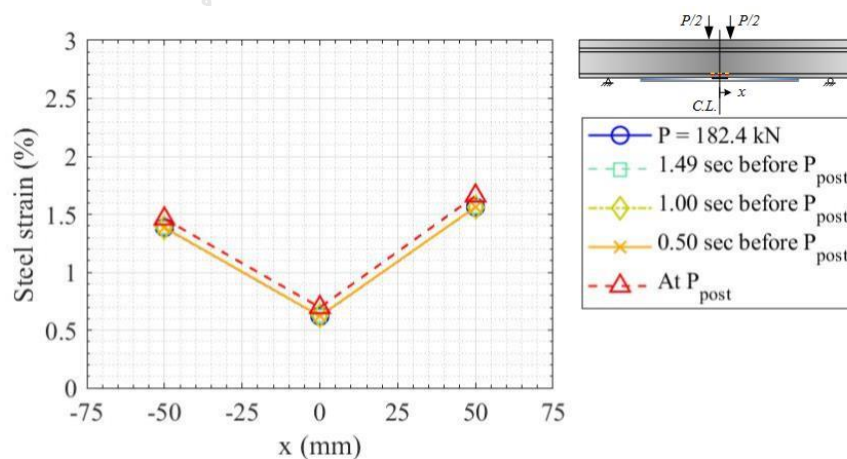


Figure C.18 Post-peak steel strain near the midspan section of beam BSM120-0.

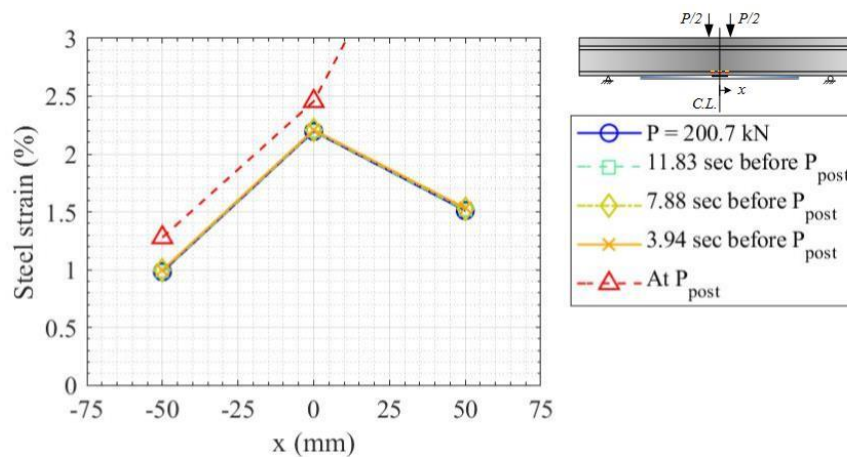


Figure C.19 Post-peak steel strain near the midspan section of beam BSM120-100.

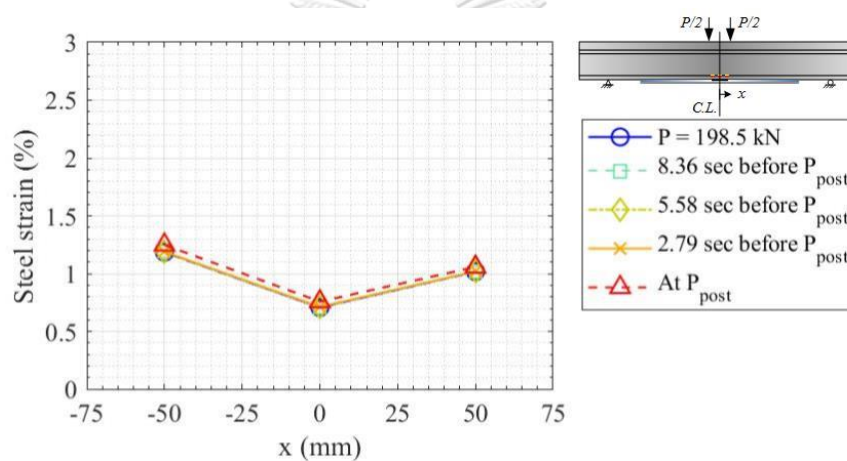


Figure C.20 Post-peak steel strain near the midspan section of beam BSM120Y-100.

C.4 Strain Distribution Along FRP Plates

Development of FRP strain before beam failure are plotted in Figure C.21 to Figure C.28. The light gray-shaded area indicates the constant moment region. This research assumes that the significantly increased of strain may cause from local fiber rupture. This phenomenon can be observed in FRP plate coupons testing under tensile load. Some part of FRP plate was found to be break before the maximum load reached. Moreover, the obviously decreased of strain is supposed to be local intermediate debonding of FRP plate. This is possible when the bonding system between FRP plate and steel beam is failed. Increasing of strain may not be continued during the increase of applied load. Constant moment zone only allows for local fiber rupture as seen in beam BMM120-0. Strain gage affixed at the distance equal to 50

mm from midspan section is found to be the local fiber rupture before catastrophic failure of FRP plate take places. It is also found that moment gradient can induce both of local fiber rupture and local FRP intermediate debonding.

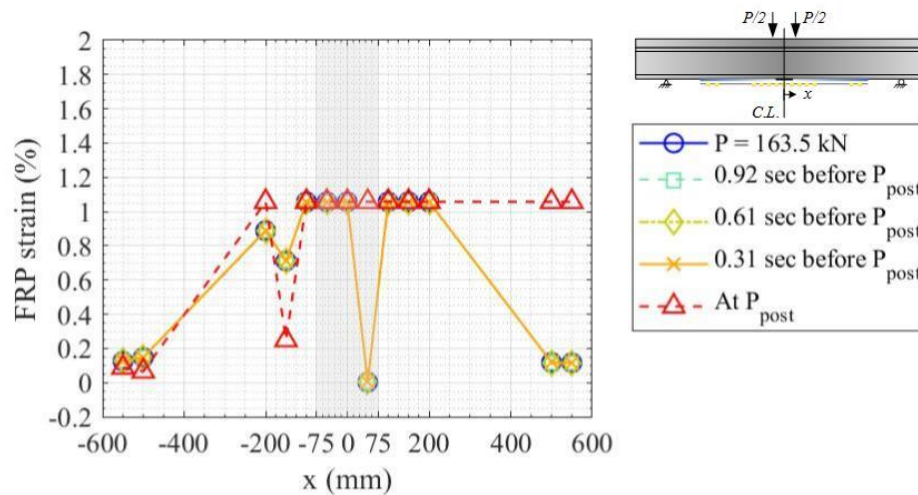


Figure C.21 Post-peak FRP strain of beam BMM120-0.

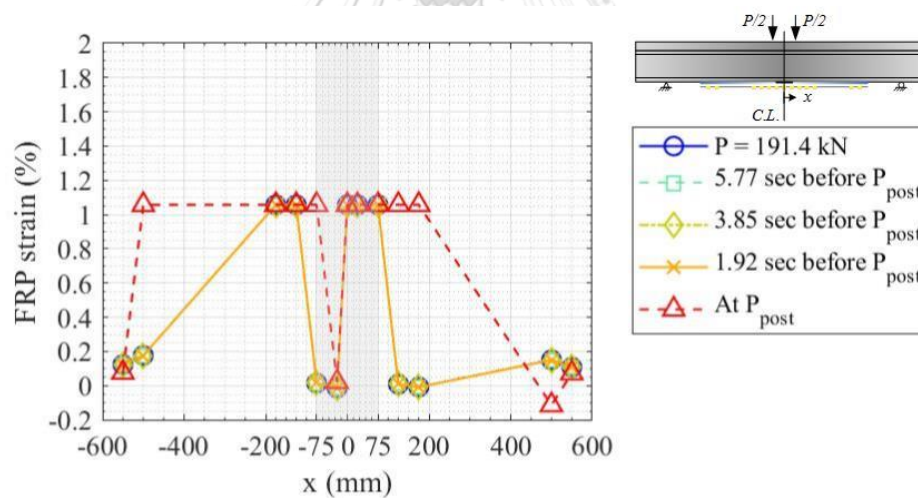


Figure C.22 Post-peak FRP strain of beam BMM120-50.

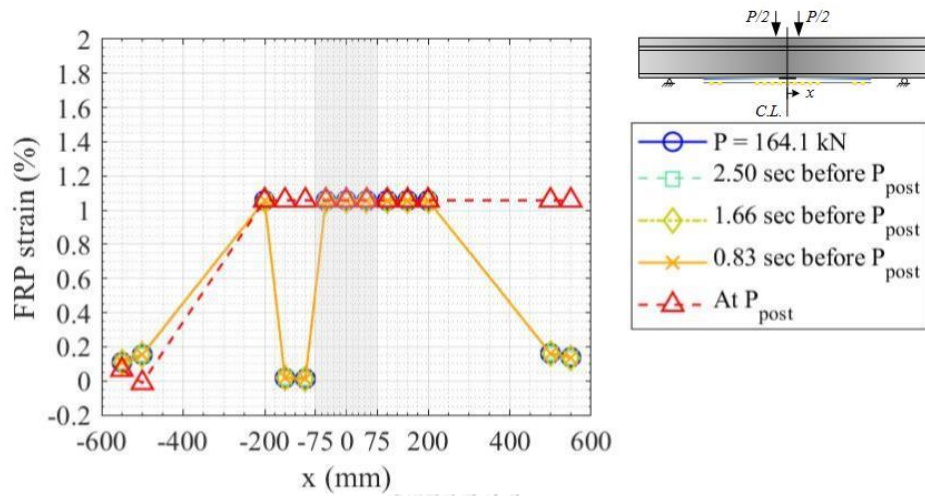


Figure C.23 Post-peak FRP strain of beam BMM120-100.

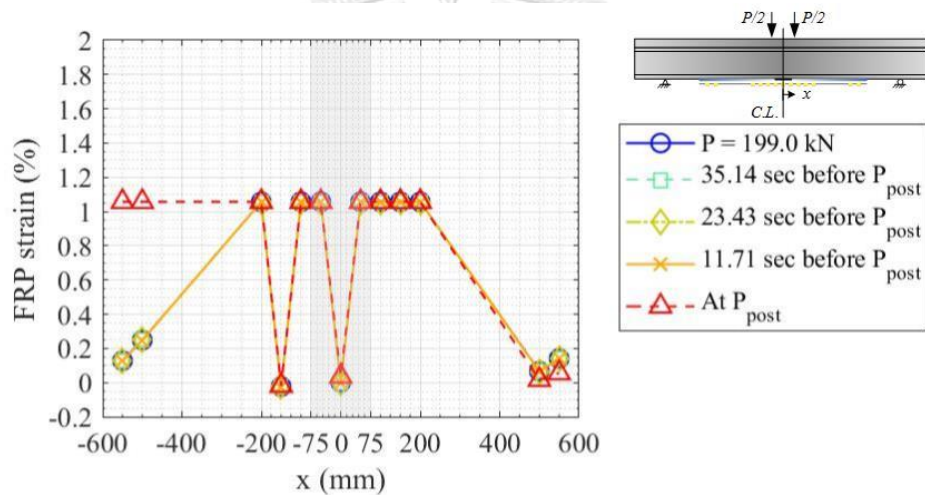


Figure C.24 Post-peak FRP strain of beam BMM120Y-100.

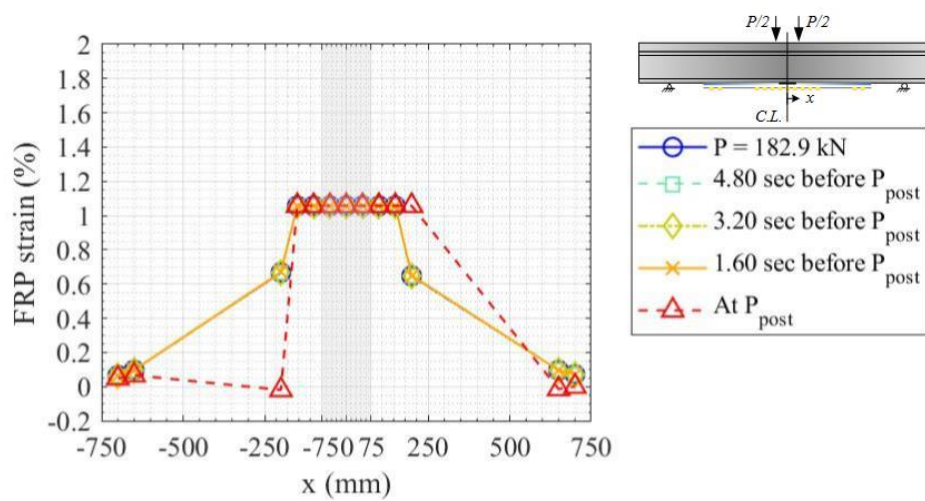


Figure C.25 Post-peak FRP strain of beam BMM150-100.

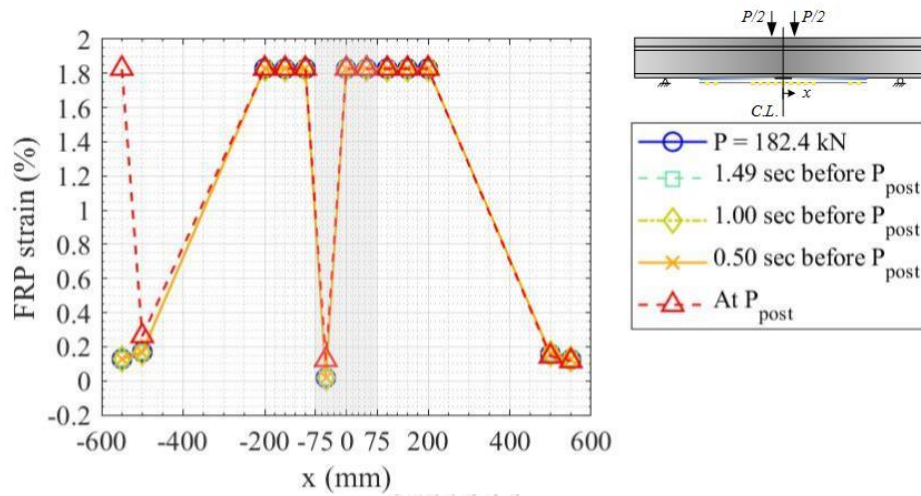


Figure C.26 Post-peak FRP strain of beam BSM120-0.

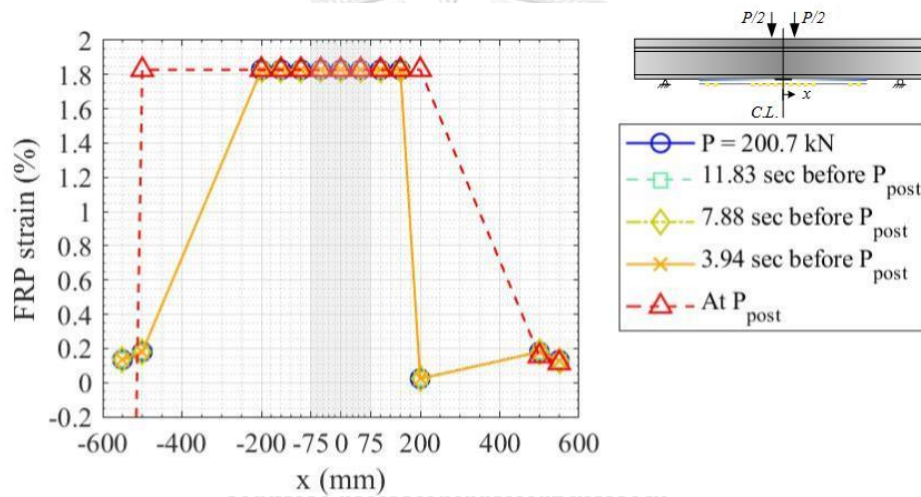


Figure C.27 Post-peak FRP strain of beam BSM120-100.

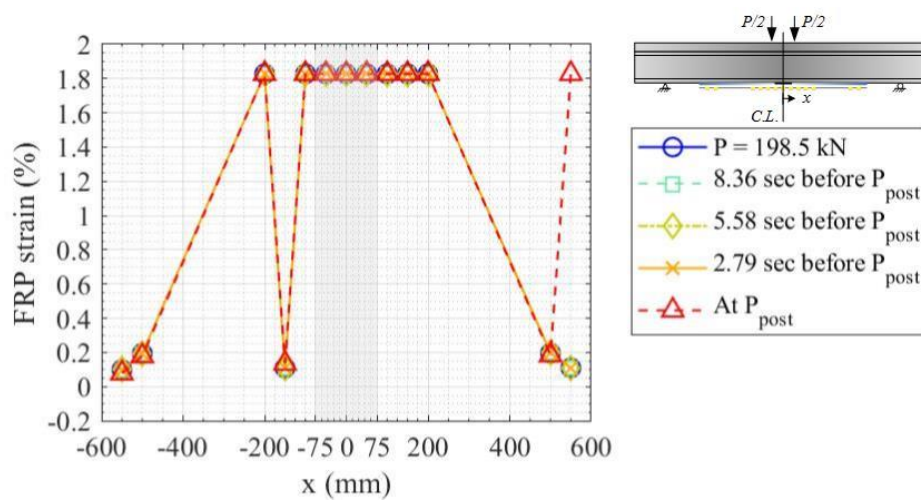


Figure C.28 Post-peak FRP strain of beam BSM120Y-100.

VITA

NAME Tosporn PRASERTSRI

DATE OF BIRTH 17 November 1986

PLACE OF BIRTH Bangkok, Thailand

INSTITUTIONS ATTENDED

- Master of Engineering in Civil Engineering, Chulalongkorn University, Bangkok, Thailand, 2012
- Bachelor of Engineering in Civil Engineering, King Mongkut's University of Technology North Bangkok, Bangkok, Thailand, 2010.

HOME ADDRESS

PUBLICATION

- Kulkiatanant, B., Prasertsri, T., Thongchom, C., and Lenwari, A. "Bond Behavior between Carbon Fiber Reinforced Polymer Plates and Steel." Proceedings of the 24th National Conference of Civil Engineering, Udonthani, 10-12 July 2019.
- Prasertsri, T., Lenwari, A., and Rungamornrat, J. "Finite Element Analysis of Strength and Ductility of Concrete Cylinders Partially Confined with FRP Sheets Using Drucker-Prager Yield Criterion." Proceedings of the 6th ASEAN Civil Engineering Conference, Bangkok, 21-22 November 2013, pp.CE28-1 to CE28-10.
- Prasertsri, T., Lenwari, A., and Rungamornrat, J. "Analysis of Compressive Stress-Strain Relationships of Concrete Cylinders Confined with Fiber- Reinforced Polymer Sheets." Proceedings of the 17th National Conference of Civil Engineering, Udonthani, 9-11 May 2012.

AWARD RECEIVED Winner award of academic steel truss contest, Sripatum University, Bangkok, Thailand, 2008.